Spectroscopy of excited states in ^{252}No

Thesis submitted in accordance with the requirements of the University of Liverpool for the degree of Doctor in Philosophy

by

Edward J. E. Parr

Oliver Lodge Laboratory

2011

Acknowledgements

For giving me the oppertunity to do my PhD, I would like to thank my supervisor Prof. Rodi Herzberg as well as Liverpool University and STFC for financial support. I am greatful to the people at the accelerator laboratory in Jyväskylä, Finland where the experiment was carried out and to Dr. Robert Page and Gail Axford who helped me with my Thesis.

Abstract

A spectroscopic study of excited states in ^{252}No was carried out to gain experimental evidence of the energies, orderings and assignments for the single particle levels in the region around the deformed shell gaps at N = 152 and Z = 100. Some of these energy levels are of particular interest as they lie close to the Fermi surface in the spherical region around the predicted next magic numbers.

The ^{252}No nuclei were produced at the accelerator laboratory in Jyväskylä, Finland, using the fusion evaporation reaction ^{206}Pb(^{48}Ca,2n)^{252}No and separated with the RITU gas filled separator. The JUROGAM and GREAT detector arrays were used for in-beam and focal plane spectroscopy respectively, allowing the recoils to be identified using recoil-decay tagging techniques. The previously identified $K^{\pi} = 8^{-}$ K isomer was investigated, with in-beam γ-ray spectra of rotational band transitions above this state being observed for the first time and the level scheme up to $I^{\pi} = 19^{-}$ (and up to 22^{-} tentatively) being found.

As the spectra produced were of low statistics, new approaches were required in their analysis to assign a single particle structural configuration to the excited state. Two methods are described which act to utilise the low statistics fully, the results of which provide strong indications that the $8^{-}\{\frac{7}{2}^{+}[624]_{\nu} \otimes \frac{9}{2}^{-}[734]_{\nu}\}$ configuration is responsible for the isomer. These results are also compared with other excited states in nuclei around the deformed shell gaps to build up a picture of regional systematics. Their bearing on the predictions for the next spherical shell closures is also discussed.

Contents

Chapter 1

Motivation in the study of super-heavy nuclei

When considering the bound nuclear system, a natural question to ask is that of the limit of its possible mass. Just as work takes place to find the maximum numbers of protons and neutrons in a given nucleus, defining the drip lines, the maximum constituent mass of a nucleus is being investigated through the study of the super-heavy nuclei.

1.1 Theoretical enhanced stability

It is seen that nuclei of increasing mass become susceptible to spontaneous fission due to coulomb repulsions. Figure 1.1 highlights the line in the nuclear chart above which nuclei in this particular super-heavy region would be expected to instantaneously fission when applying the simple liquid drop model, with those close to the line expected to fission with very short half-lives due to a low fission barrier. However, by considering the quantum shell structure of the constituent nucleons, regions of enhanced stability are predicted. An example of this stability is shown in the Figure where shell correction energy contours for ground state nuclei are given and all synthesised nuclei at the time of the publication are highlighted by the crosses and

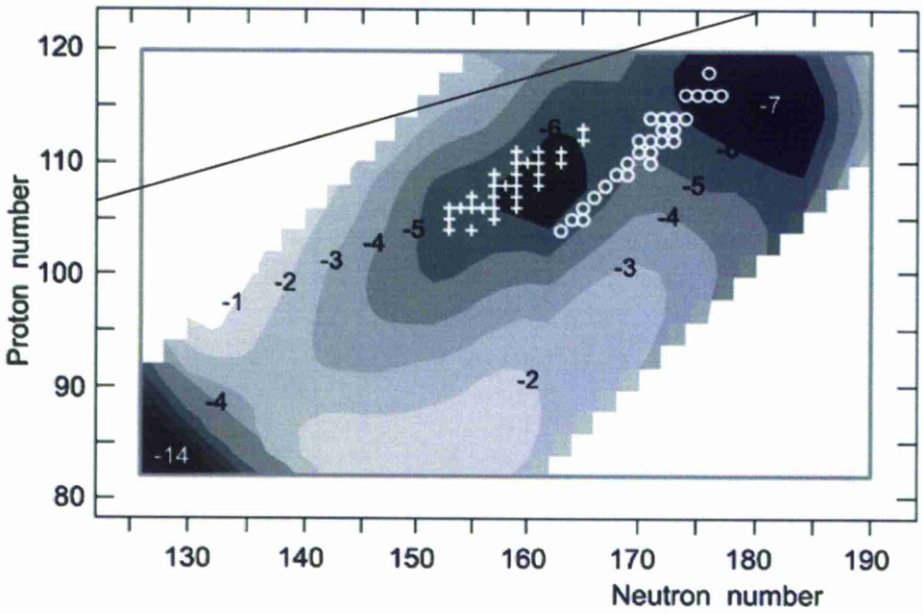

Figure 1.1: Shell correction energies δU_{SH} (MeV) calculated from the last known doubly magic ^{208}Pb up to the super-heavy nuclei region for ground state nuclei. Black line shows the liquid drop model limit for instantaneous fission and the crosses and circles give synthesised nuclei at the time of publication. Figure taken from [1].

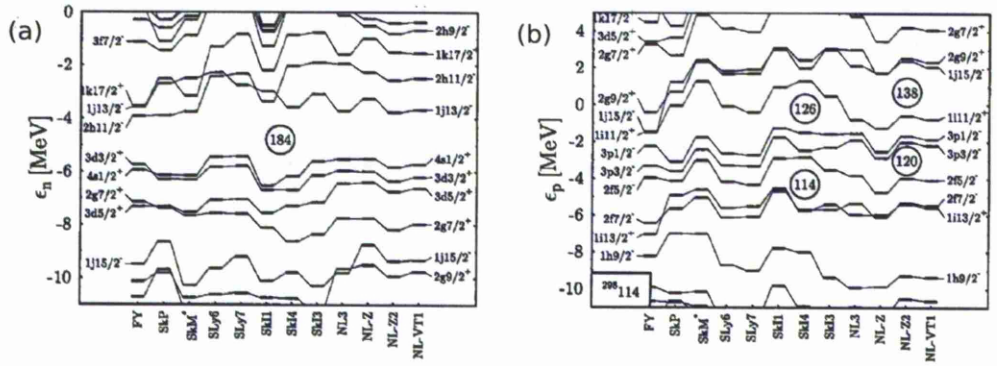

Figure 1.2: Spherical single particle energy levels calculated for $^{298}_{184}114$ using various self-consistent mean field methods. Predicted next spherical shell gaps are shown for neutrons (a) and protons (b) taken from [2].

circles [1]. This increased stability implies the question of if, and where in this region, possible spherical shell closures may lie. Above the experimentally and theoretically well understood values of 2, 8, 20, 28, 50, 82 and 126 (neutron only), much work has been done to theoretically predict the next possible values for protons and neutrons. The approaches used to make these predictions fall into two main categories; that of macroscopic-microscopic and self consistent mean field methods.

The macroscopic-microscopic methods have been well established, with initial predictions for the next spherical shell closures of Z = 114 and N = 184 being made in 1967 by Meldner [3]. Since then a range of similar calculations have yielded roughly the same values as those initially proposed [4, 5, 6, 7]. More recent calculations have employed a self consistent mean field method where the resulting picture is less clear. The neutron gap at N = 184 is consistently produced by most calculations. However, values of Z = 114, 120 and 126 may be seen, or even a diffuse shell closure spread over a plateau of values [8, 9, 2, 10]. The neutron and proton single particle spherical energy levels calculated for a $^{298}_{184}114$ nucleus are given in Figure 1.2 [2] and are found by using various different self consistent mean field methods which are consistent

in predicting the lower mass spherical shell gaps. The difference in level energies produced may be seen and the effect on changing the spherical shell closures, for the proton value particularly, is apparent. With theoretical approaches producing different shell closure values, it is vital to obtain experimental evidence in this region to compare with predictions and hence constrain the theoretical methods.

1.2 Experimental approaches

The synthesis of man-made unstable isotopes of ever increasing mass, has been steadily progressing over the last 80 years. The production of nuclei approaching the next predicted spherical shell closures, has been achieved in the past 30 years at the GSI laboratory in Darmstadt, Germany with isotopes of elements Z = 107 to 112 [11, 12] and in the past 10 years at the RIKEN Laboratory in Japan and the Flerov Laboratory in Dubna, Russia with isotopes of elements Z = 113 [13] and 114 to 118 [1, 14] respectively. Many of these have been subsequently reproduced at other laboratories, including those named above as well as LBNL in Berkeley, USA. The cross section of production for these nuclei approaching the highest masses, are seen to be in the order of picobarns. This puts them at the limit of feasibility for the present experimental setups, meaning only small numbers of each isotope have been observed. Information may then be extracted for properties such as half-lives, masses, alpha energies, cross sections of production and possible decay modes. The existence of an increased stability in the region is shown from this data, as the broad quantities concur with most predictions [1, 15]. However, the lack of statistics means that detailed experimental information relating to the single particle energy level structure within the region is not possible. This is required to rigorously test the various theoretical calculations which predict the location of the next spherical shell closures.

A different approach taken in the past few years, is to concentrate on the production of nuclei around the deformed shell gaps illustrated in Appendix A (Figures A.1 and A.2) [16] for prolate deformations at N = 152 and Z = 100. All theoretical

calculations predict these deformed shell closures, however, the positions vary as the energies and orderings of the single particle energy levels vary. Although this is far from the predicted next spherical shell closures, it is seen that some of the single particle energy levels from that region are moved down in energy with increased deformation and lie around the Fermi surface for these lighter mass nuclei. These nuclei inhabit the 'plateau of stability' shown in Figure 1.1 and the key advantage of studying these, is that their cross sections of production are seen to approach the order of microbarns. Producing greater numbers of nuclei by several orders of magnitude, allows for significantly populated γ-ray spectra from their de-excitations to be acquired illuminating the detailed structures within the nuclei. Experimental results of the assignment, ordering and energies of the single particle levels, may be acquired from the study of K-isomeric states, formed from single particle excitations predicted to be prevalent in the region [6]. This is done using a technique proposed by Jones [17], whereby the delayed decay of the isomer is indicated by a cascade of conversion electrons from converted lower energy transitions. This then offers detailed comparisons to the various theoretical models used for the region, where the energies of the single particle levels, and consequently the positions of the deformed and spherical shell closures, differ. This may then be used to compare with and constrain the theoretical approaches.

1.3 Present investigation

Deformed shell gaps at N = 152 and Z = 100 are consistently predicted by macroscopic-microscopic calculations [4, 16, 18] between the $\frac{9}{2}^-[734]_\nu$ and $\frac{1}{2}^+[620]_\nu$ and the $\frac{7}{2}^+[633]_\pi$ and $\frac{1}{2}^-[521]_\pi$ states respectively. However, self-consistent mean field calculations often predict different values, such as those by A. Chatillon [19]. Here the $\frac{9}{2}^-[734]_\nu$ and $\frac{7}{2}^+[633]_\pi$ states, originating from the $1j\frac{15}{2}^-$ neutron and $1i\frac{13}{2}^+$ proton orbitals respectively, are calculated at higher energies opening up N = 150 and Z = 98 and 104 deformed shell gaps. It is clearly important to gain detailed experimental information

about the single particle energy levels within this region.

A study of the excited states found in the even-even constituents of the N = 150 isotone chain [20] reveals an 8^- and 2^- state in all five nuclei with Z = 94 to 102. As the neutron number remains constant it would be reasonable to assume a neutron configuration is responsible for all of the observed states, this is also indicated by the energies of the 8^- states showing a variation of only ~80 keV. Macro-microscopic calculations using a Woods-Saxon potential [20] predicts the energies of $8^-\{\frac{7}{2}^+[624]_\nu \otimes \frac{9}{2}^-[734]_\nu\}$ states in all members of the isotone chain and are consistent with those observed. Direct experimental evidence has also been found for the $8^-\{\frac{7}{2}^+[624]_\nu \otimes \frac{9}{2}^-[734]_\nu\}$ configuration being responsible for the $K^\pi = 8^-$ state in ^{250}Fm [21]. This was provided by interband/intraband γ-ray intensity ratio measurements from transitions within rotational bands built on the state (see Section 4.1 for details of method). An indication of an N = 152 deformed shell gap may be shown by the study of the member of the N = 152 isotone chain ^{254}No. Two excited states have been observed with configurations $3^+\{\frac{1}{2}^-[521]_\pi \otimes \frac{7}{2}^-[514]_\pi\}$ and $8^-\{\frac{7}{2}^-[514]_\pi \otimes \frac{9}{2}^+[624]_\pi\}$. These were assigned from γ-ray intensity ratio measurements within rotational bands and are also predicted by macro-micro calculation using a Woods-Saxon potential [22, 23]. The observation of neutron excitations in the N = 150 isotones and proton excitations when the neutron number is raised to N = 152 is a good indication of the N = 152 deformed shell gap.

The present investigation aims to provide direct experimental evidence for the configuration of the recently discovered 8^- K-isomeric state in the N = 150 isotone chain member ^{252}No [24]. This will be done using in-beam γ-ray spectra to observe inter/intraband intensity ratios between transitions within rotational bands built upon the excited state. Proposed ramifications of experimental results in the region, including present work, on theoretical models will be discussed in Chapter 6.

Chapter 2

Theoretical Basis

2.1 Liquid Drop Model

The binding energy of a nuclear system ${}^{A}_{Z}X_{N}$ may be written as

$$B = \{Zm_p + Nm_n - m({}^{A}_{Z}X_{N})\}c^2 \tag{2.1}$$

where the masses of the proton, neutron and nucleus are given by m_p, m_n and m respectively. Experimentally obtained values of this binding energy per nucleon, show that it remains roughly constant at ~8 MeV for all but the lightest nuclei. The implication of this, is that the attractive nucleon-nucleon force which provides the potential in which the nuclear system exists, is short ranged and so is only experienced by closely neighbouring constituents. This provides us with the analogous system of a classical liquid drop, in which short ranged electromagnetic van der Waals interactions act to bind the droplet with an energy proportional to its volume. This binding is reduced by a factor proportional to the surface area (i.e. the surface tension), causing the droplet to assume a spherical shape. An additional term required to model the binding energy of nuclei, represents the Coulomb repulsion provided by its protons. The binding energy of a nucleus found as a direct analogy to that of a charged spherical liquid drop of incompressible fluid, using the viscosity η and surface tension σ, may then be written as

$$B = \frac{4\pi\eta R_0^3}{3}A - 4\pi\sigma R_0^2 A^{2/3} - \frac{3}{5}\frac{e^2}{4\pi\epsilon_0 R_0}\frac{Z(Z-1)}{A^{1/3}} \tag{2.2}$$

where $R = R_0 A^{1/3}$ gives the radius of the nucleus and $R_0 \simeq 1.2$ fm. However values for the viscosity and surface tension of a nuclear fluid are not known, therefore experimental values for the binding energies must be fitted to a function of this form. We may then rewrite Equation 2.2 using unknown energy parameters for each term and adding two simple quantum correction terms to give

$$B = a_v A - a_s A^{2/3} - a_c\frac{Z(Z-1)}{A^{1/3}} - a_i\frac{(N-Z)^2}{A} + a_\delta A^{-3/4}. \tag{2.3}$$

Here the broad quantum behaviour is represented by an isospin term, with constant a_i, which represents the stabilising effect on nuclei of having lower values for the difference between proton and neutron numbers. This is necessary to reproduce the observed inhibition of systems to increase their binding energy indefinitely by the addition of neutrons. Finally, a pairing term, with constant a_δ, is added to increase stability for nuclei with paired protons or neutrons. This will be discussed in more detail in section 2.3.1. The term takes a positive value for nuclei with even numbers of both protons and neutrons, a negative value if both are odd and zero if a combination of odd-even is present.

The liquid drop model may also be used to estimate whether or not a nucleus will instantly fission due to Coulomb repulsions. Here we consider a spherical nucleus of radius R and then the same nucleus with a prolate deformation, so that its major axis is given by $a = R(1+\epsilon)$ and its two minor axis by $b = R(1+\epsilon)^{-1/2}$ (volume is conserved as $R^3 = ab^2$). With the additional deformation, the only terms in Equation 2.3 to change, will be the surface and Coulomb terms, which will change by factors of $(1+\frac{2}{5}\epsilon^2...)$ and $(1-\frac{1}{5}\epsilon^2...)$ respectively. This relates to a decrease in binding energy with deformation for the surface term as the surface area increases and an increase from the Coulomb term as repulsive charge is moved apart. The change in binding energy may then be given as

$$\Delta B(\epsilon) = B(\epsilon) - B(\epsilon = 0) \simeq \left(\frac{1}{5} a_c \frac{Z(Z-1)}{A^{1/3}} - \frac{2}{5} a_s A^{2/3} \right) \epsilon^2, \tag{2.4}$$

so that the condition for increased binding energy with prolate deformation and, hence for a nucleus to instantaneously fission, is given as

$$\frac{1}{5} a_c \frac{Z(Z-1)}{A^{1/3}} > \frac{2}{5} a_s A^{2/3}. \tag{2.5}$$

By fitting observed binding energies to Equation 2.3, the classical liquid drop model, with some quantum corrections, appears to explain the broad behaviour of the nuclear binding energy. It also predicts well the existence of a limit for mass of nuclei above which coulomb repulsions begin to induce fission. It is, however, limited as a model which may be taken further in predicting the more detailed nuclear effects observed. For this the constituent nucleons must be considered as occupying individual fermionic states within the nuclear potential.

2.2 Deformed Potential Shell Model

A successful approach when looking to describe enhanced stability at the 'magic numbers' of protons and neutrons, along with other observed nuclear behaviour dictated by the constituent nucleons quantum nature, has been the application of the spherical shell model. Here, the single particle states of all the constituent fermionic nucleons are found as interacting only with a mean field potential, chosen to mimic a smooth distribution of nuclear matter in a spherical nucleus. This model is present in many publications [25] and will not be discussed in further detail here. However, ground state nuclei away from shell closures, can be found to display large quadrupole moments, indicating a non-spherical deformed shape. Clearly, this is energetically favourable and the spherical shell model must be modified in order to accommodate and try to explain this phenomenon.

A deformed potential shell model contains single particle nucleon orbitals found within an axially deformed mean field potential. The effect on the energies of the

single particle states due to the application of this deformation to the potential, is shown in Appendix A (Figures A.1 and A.2) [16] using a Woods-Saxon form of the potential for neutrons and protons respectively. Various effects on the energy levels are apparent as the deformation parameter is increased. Firstly, the degeneracy of orbitals present in the spherical shell model (deformation parameter = 0) are lost as the energies split. To explain this, we can consider the $g_{9/2}$ orbital which displays a degeneracy of 10 protons. This is determined by the possible projection of its total angular momentum j (= 9/2) upon an axis to give the quantum number m_j, which may take values -j, -j + 1, ... j. In a spherical potential, all of these states would be degenerate in energy, but as we introduce a prolate deformation to the potential, as shown in Figure 2.1, the energy of the state is now dependent on the magnitude of the total angular momentum projection onto the the symmetry axis, which is given the value Ω. This degeneracy split may be understood in terms of the orbitals overlap, and hence interaction, with the nuclear potential. For our prolate deformation, the larger $\Omega = 7/2$ will give an orbital less overlapping, leading to a higher energy less bound state, due to the attraction of the nucleon-nucleon force. The converse is then true for the $\Omega = 5/2$ state, where a greater overlap with the nuclear potential is seen, giving a more bound state. This effect is reversed when introducing an oblate deformation to the potential. Each Ω state has a two fold degeneracy of $\pm\Omega$ giving the same projection of j onto the symmetry axis.

Another effect observed, is that the higher the shell, the greater rate of change in energy seen for increasing deformation. This is due to higher orbitals being at greater radii and therefore, a greater change in their overlap with the potential is seen with deformation. This last effect leads to another important phenomenon crucial in tying together deformed potential models with experimental results, which is that of deformed shell closures. In Appendix A (Figures A.1 and A.2) we see gaps opening in the energy levels which correspond to deformed shapes of the nucleus. As with spherical nuclei, enhanced stability of a system is seen at these large energy level gaps and a deformed shape may become energetically favourable for a nuclear system.

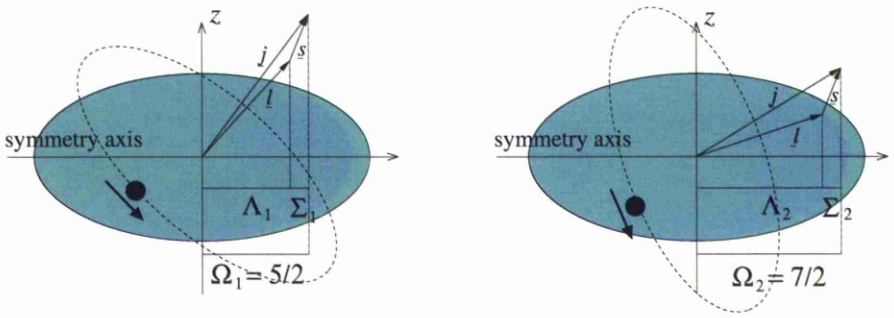

Figure 2.1: Two j states from the same orbital with different Ω values in a prolate deformed nucleus.

The increased shift in energy levels for higher orbitals explains the tendency for deformation in higher mass nuclei away from spherical shell closures and the existence of super-deformed states.

The energy level eigenstates found using the deformed potential shell model, may be labelled using their asymptotic quantum numbers:

$$\Omega^{\pi}[Nn_z\Lambda] \tag{2.6}$$

where the principle quantum number N represents the number of oscillation quanta and of those n_z gives the number along the symmetry axis. The projection of the orbital angular momentum along the symmetry axis is given by Λ which combines with that of the spin projection Σ $(= \pm 1/2)$ to give the total angular momentum's projection as

$$\Omega = \Lambda + \Sigma. \tag{2.7}$$

2.3 Realistic Modelling

The models we have looked at up to now, work well at predicting certain trends and observations for nuclei. However, the complexity of the nuclear system and the

assumptions made in all models, mean that additional refinements and considerations must be applied to explain specific phenomena and reproduce experimental values.

2.3.1 Pairing and Quasi-particle States

The single particle model predicts nucleons to fill levels of increasing energy up to the Fermi level, λ, and that non-collective excitations are created by promoting a nucleon into a higher orbital, creating a particle-hole pair. For the first excited state at ϵ_i this would require an energy of (ϵ_i-λ). However, experimental evidence consistently shows first non-collective excitation energies $\sim$ 1.5 MeV higher than those predicted by this for even-even and around half this value higher for odd-even nuclei. This is due to a stabilising effect that causes the total binding energies of even-even nuclei to be higher than neighbouring odd-even nuclei, whose values are higher again than those of odd-odd. These effects are explained by an inclination for nucleons to pair in the nucleus. This is an amendment to a core assumption of the shell model, namely that the nucleons are non-interacting within a uniform potential. This pairing can be thought of as two like nucleons in the same degenerate orbital, occupying time reversed paths. This gives the greatest possible overlap between the orbitals and due to the attractive nature of the nucleon-nucleon force, gives a uniquely bound state for two nucleons. Pairing helps to explain other observed phenomena, such as all ground state even-even nuclei having total combined angular momentum and parity $J^\pi = 0^+$ as the lowest energy state. This is because it invariably consists of fully paired and time reversed degenerate nucleons.

This maximum overlap between the wave functions of paired nucleons, leads to a 'scattering' into higher energy orbitals, which pairs occupy together as, J^π must remain constant. The system may now be viewed, not as orbitals occupied or unoccupied, but as having a finite probability of occupation (realistically only states close to the Fermi energy have a probability that deviates significantly from 1 or 0). This distribution is shown in Figure 2.2 where the probability of occupation ${V_i}^2$ is given as

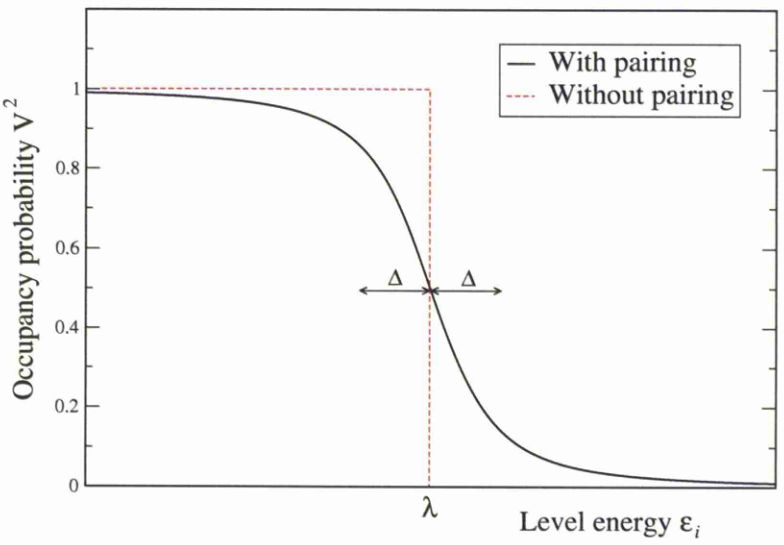

Figure 2.2: Probability of single particle nucleon states at energies ϵ_i being occupied, with and without pairing.

$$V_i^2 = \frac{1}{2}\left[1 - \frac{(\epsilon_i - \lambda)}{\sqrt{(\epsilon_i - \lambda)^2 + \Delta^2}}\right] \tag{2.8}$$

with ϵ_i being the energy of a given single particle level and λ the Fermi energy. Δ gives the gap parameter and is a measure of the strength of the pairing interaction.

In the presence of pairing, it is now not possible to define an excitation from a level at the Fermi surface to an excited level ϵ_i by its excitation energy (ϵ_i-λ), but instead by its quasi-particle energy

$$E_i = \sqrt{(\epsilon_i - \lambda)^2 + \Delta^2}. \tag{2.9}$$

This quasi-particle is a probabilistic distribution of particle and hole states where the probability of the presence of a hole is $U_i{}^2$ = 1-$V_i{}^2$ (i.e. the level must be occupied or not). Excitations are now thought of with regards to the creation of quasi-particle states. Considering a single particle excitation for an even-even nucleus, this will create two quasi-particle states, one being the excited particle in a higher orbit, the

other that of the hole state left behind. The energy for such an excitation will be the sum of these two states energies giving

$$E_{x_{ij}} = \sqrt{(\epsilon_i - \lambda)^2 + \Delta^2} + \sqrt{(\epsilon_j - \lambda)^2 + \Delta^2} \geq 2\Delta \tag{2.10}$$

with the energy of the levels for the particle and hole being ϵ_i and ϵ_j respectively. It is shown that the 2 quasi-particle excitation energy for an even-even nucleus must be greater than 2Δ giving the observed 'energy gap' for their first single particle excitations. Values of Δ are typically found to be $\sim$ 700 keV $\rightarrow$ 1 MeV [25].

2.3.2 Macroscopic-Microscopic Models

In the previous sections we have considered nuclear models which take a classical macroscopic approach in the LDM and also treated the nucleons individually as non-interacting particles in a deformed potential; both of which reproduce certain aspects of nuclear properties well. The LDM can predict broad trends as a function of mass number, but is unable to predict finer detail observed in the properties due to the quantum nature of the constituent nucleons not being taken into account. Likewise, single particle models may work well in finding level orderings to represent fluctuations in nuclear properties, but values for absolute quantities such as nuclear binding energy, do not concur with evidence. The Strutinsky model essentially takes the successful aspects of both models to determine certain nuclear properties. The method may be most simply represented as

$$U = U_{smooth} + \delta U_{SH} \tag{2.11}$$

where a value of the property U, such as binding energy, consists of a base line term U_{smooth} obtained from a macroscopic model. This is deviated from by an oscillatory term δU_{SH} which may be found at the Fermi surface using single particle microscopic models to give the specific oscillation as a function of A (Z and N) from smooth behaviour; a schematic illustration of which is shown in Figure 2.3.

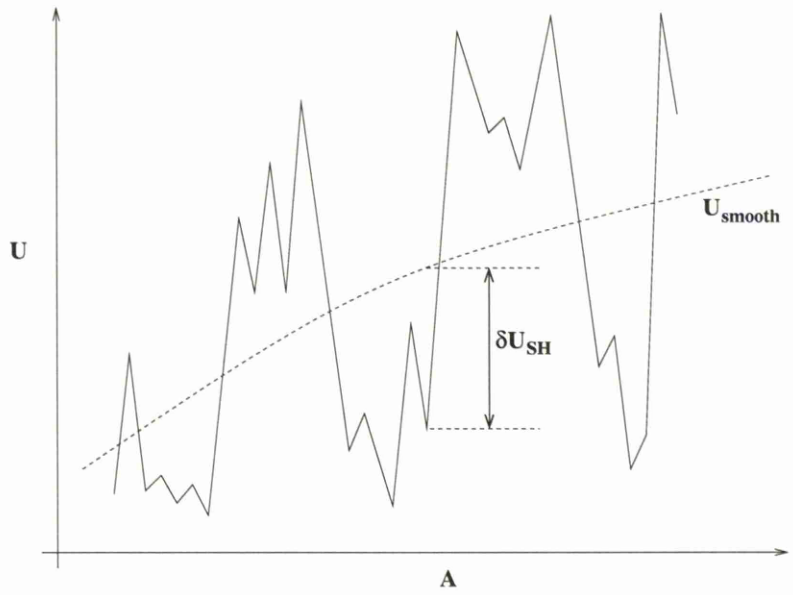

Figure 2.3: Representation of macroscopic-microscopic model using macroscopic U_{smooth} with single particle model δU_{SH} oscillations.

To obtain the δU_{SH} term we may consider the total single particle binding energy, obtained by summing the single particle energies calculated for all the occupied states. This containing the desired regionally varying oscillatory term and a smoothed component $\tilde{U}_{SH}$:

$$U_{SH} = \sum_{i=1}^{A} \varepsilon_i n_i = \tilde{U}_{SH} + \delta U_{SH} \tag{2.12}$$

where ε_i and n_i are the energies and degeneracies of all occupied energy levels A. This smoothed component may be found by using a smoothed level density $\tilde{g}(\varepsilon)$ and integrating up to the Fermi level $\tilde{\lambda}$ so that

$$\tilde{U}_{SH} = \int_{-\infty}^{\tilde{\lambda}} \varepsilon \tilde{g}(\varepsilon) d\varepsilon. \tag{2.13}$$

where $\tilde{\lambda}$ is found for the smoothed level density $\tilde{g}(\varepsilon)$. The oscillatory term may now be found as

$$\delta U_{SH} = \sum_{i=1}^{A} \varepsilon_i n_i - \int_{-\infty}^{\tilde{\lambda}} \varepsilon \tilde{g}(\varepsilon) d\varepsilon \tag{2.14}$$

and Equation 2.11 may be written as

$$U = U_{smooth} + [U_{SH} - \tilde{U}_{SH}]. \tag{2.15}$$

The importance of regional level densities on the stability of nuclei, may be appreciated by the oscillating term in Equation 2.14. A region of low level density (i.e. spherical shell gaps) would mean nucleons close to the Fermi surface would occupy lower and therefore more bound states than assumed by a smoothed level density. This would lead to an oscillation of higher binding energy for that region. Conversely, in a region densely populated by levels, we see a de-stabilising oscillating term. This effect of increased stability in terms of lower energy density also helps to explain observed deformation in nuclei. Graphs labelled A in Figure 2.4 [26] show shell corrections as a function of deformation parameter β for different neutron numbers. We can see that the neutron numbers relating to spherical shell closures (50, 82, 126) have minima at

$\beta = 0$, where those far from shell closures for heavier nuclei such as $N = 100$, may see energy minima for a prolate deformed shape. This is driven by level densities for single particle states found using deformed potential shell models where deformations between shell closures can lead to regions of low level density or what are known as deformed shell gaps. This is illustrated too, in the Figure with the graphs labelled B, giving the ratio of the deformed shell model level density to that of the smoothed form at different N. A high ratio relates to a less bound system and it can be seen how this is reduced for $N = 100$ nuclei by acquiring a prolate deformation.

2.3.3 Self-Consistent Mean Field Models

Another theoretical approach employed to describe the nuclear properties, is the use of a self-consistent mean field potential in the calculations. This is obtained through an iterative process, whereby an initial potential which mimics the nuclear distribution is used to calculate the single particle wave functions of the constituent nucleons. These are then used to give a nuclear potential and the process continues to give the self-consistent mean field potential. This method essentially uses just the microscopic part of the macro-micro model.

2.4 Nuclear rotations

A rotation about any axis of a spherical nucleus leaves the nuclear wavefunction indistinguishable and is therefore quantum mechanically forbidden. However, deformations in nuclei allow for their orientation to be defined, which leads to the possibility of rotations. The angular momentum associated with this rotation $\underline{R}$, couples with that from any single particle contributions $\underline{J}$, to give the total angular momentum

$$\underline{I} = \underline{J} + \underline{R} \tag{2.16}$$

where the total projection of $\underline{I}$ onto the symmetry axis gives the quantum number K, as shown in Figure 2.5. Increasing rotational angular momentum does not change

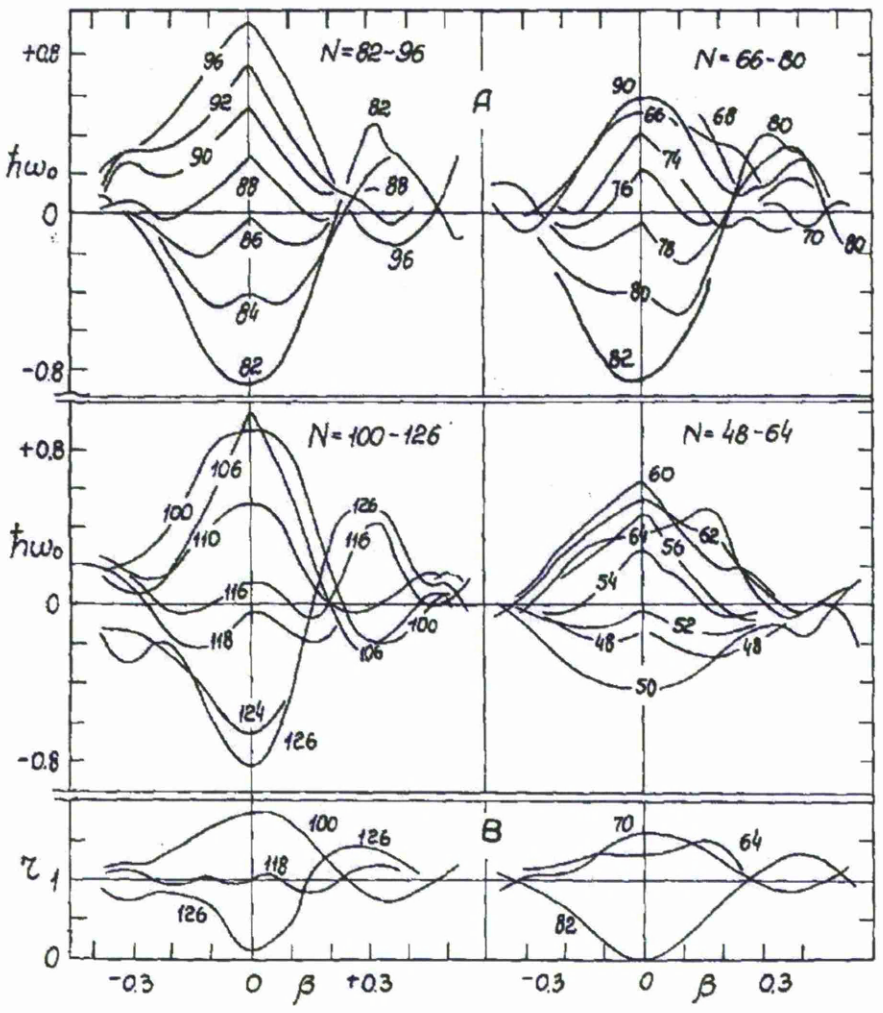

Figure 2.4: Shell corrections for varying neutron number (A) and ratio between shell model level densities to that of a smoothed form (B) shown as function of deformation β. Taken from [26].

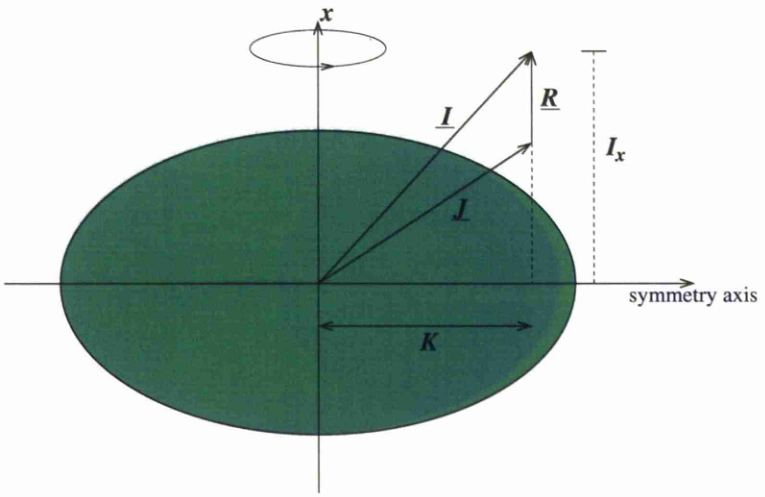

Figure 2.5: Coupling of single particle $\underline{J}$ and rotational $\underline{R}$ angular momenta to give total $\underline{I}$ in a deformed nucleus.

the K value such that $\underline{J}_z = K$ (this is $\underline{J}$ aligned with the symmetry axis).

Rotationally excited states may be labelled with the signature quantum number r which relates to the rotational invariance of the system when rotated through 2π. The r value of a state is given by

$$r = (-1)^I \tag{2.17}$$

which leads to two rotational bands of signature ± 1 with selection rules

$$\begin{aligned} I &= 0, 2, 4, ... \quad r = +1, \\ I &= 1, 3, 5, ... \quad r = -1 \end{aligned} \tag{2.18}$$

for $K = 0$ systems. When $K \neq 0$ the signature is given by $r = (\text{-}1)^{I+K}$ and the band consists now of both $r = \pm 1$ signature sequences with $I = K$, K+2, K+4... and $I = K$+1, K+3....

The relationship between the rotational frequency ω and the total angular momentum I of a nucleus may be defined by kinematic and dynamic moments of inertia given respectively as

$$\Im^{(1)} = \hbar \frac{I}{\omega} = \left(\frac{2}{\hbar} \frac{dE(I)}{d(I^2)} \right)^{-1}, \tag{2.19}$$

$$\Im^{(2)} = \hbar \frac{dI}{d\omega} = \left(\frac{1}{\hbar^2} \frac{d^2E(I)}{dI^2} \right)^{-1} \tag{2.20}$$

assuming the total angular momentum aligns with the x-axis so that $I_x \sim I$. A rigid body would require just one value for the moment of inertia as $\Im^{(1)} = \Im^{(2)}$, but the dynamic nature of the nucleus under rotation means that these values vary with ω.

2.5 K-isomerism

Isomeric, or meta-stable, states are excitations of nuclei in which their decay is inhibited due to structural effects. There is no strict definition for an isomer, but any states with decay lifetimes significantly longer than prompt decays may be considered isomeric.

The existence of K isomers depend on the difficulty to change the magnitude of the projection of their total angular momentum along their symmetry axis K. These may occur in prolate nuclei where the K value is given as the sum of all the contributing nucleons total angular momentum projections

$$K = \sum_i \Omega_i. \tag{2.21}$$

Contributions to K are from either broken pairs or odd nucleons, as pairs have $J^\pi = 0^+$. Also, no collective contributions are seen, as rotation about the symmetry axis is forbidden. This also means that K is a conserved quantity for a given single particle excitation. An isomer may exist if the change in K required for the nucleus to decay, ΔK, is large, as this implies a large shift in the orientation of the total nuclear spin vector $\underline{I}$ [27]. This means there are no states with similar wave functions

for the nucleus to decay into and the process is therefore inhibited. For this decay to proceed via an electromagnetic transition of multipole $\sigma\lambda$, it is said to have a degree of forbiddeness

$$\nu = \mid \Delta K \mid -\lambda. \tag{2.22}$$

This acts however to hinder not forbid the process. By comparing the observed partial half-life $T^{\gamma}_{1/2}$ with that of the Weisskopf estimate $T^{W}_{1/2}$ (see Section 2.7.1) a reduced hindrance factor scaled in relation to the forbiddeness may be given as

$$f_{\nu} = (T^{\gamma}_{1/2}/T^{W}_{1/2})^{1/\nu}. \tag{2.23}$$

This value should be considered in relation to its order of magnitude due to the crude model employed, but should remain at $\sim$ 100 for all degrees of forbiddeness for transitions from highly pure K-isomeric states [28]. A lower value would indicate significant mixing of other states in the isomer and the single particle excitation could not be considered pure.

2.6 g factors

The orbital magnetic dipole moment from a particle of charge e and mass m with orbital angular momentum l is given for a quantum system as

$$\mu = \frac{e\hbar}{2m} l \tag{2.24}$$

where vectors μ and l are anti-parallel (this is in direct analogy to a classical system of a current loop). By inserting the proton mass m_p into Equation 2.24 we can write it in the form

$$\mu = g_l l \mu_N \tag{2.25}$$

where the $e\hbar/2m_p$ term has been replaced by the nuclear magneton μ_N. A g_l factor is also included which, as a nucleon of mass m_p and charge e has been assumed, scales

the μ value depending on the system considered. Therefore, in the case of single free orbiting nucleons $g_l = 1$ for a proton and 0 for a neutron (these values become $\sim$1.1 and -0.1 respectively for nucleons in a bound nucleus). The intrinsic spin s of a nucleon also provides a magnetic dipole moment with associated g_s factor so that the total contribution from a single valence or excited nucleon is found from these two components. This has an overall g_K factor which may be estimated as

$$g_K = g_l \pm \frac{1}{2l+1}[g_s - g_l] \tag{2.26}$$

where the $\pm$ is determined by aligned or anti-aligned orbital angular momentum and spin respectively. The g_K factor is very much dependent upon the single particle orbital considered.

A two quasi-particle state, where the single particle components have g_K factors g_{K1} and g_{K2} combine using the Landé formula to give total g_K factor for the excitation of

$$g_K = \frac{(g_{K1} + g_{K2})}{2} + (g_{K1} - g_{K2}) \cdot \left(\frac{\Omega_1(\Omega_1+1) - \Omega_2(\Omega_2+1)}{2K(K+1)} \right). \tag{2.27}$$

Here Ω is the individual particles projection of total angular momentum onto the symmetry axis and K is the total combined projection for the isomer.

Collectively rotating nuclei will also clearly create a magnetic dipole moment due to the nuclear charge, so it follows that the g factor be given as the ratio $g_R = Z/A$ assuming a uniformly rotating, uniformly charged system. This however, is not always the case and g_R factors are seen at slightly below this value for many rotating nuclei. A quenching factor q is often added giving $g_R = q.(Z/A)$. A value of $q \sim 0.7$ is found to be appropriate for rotating nuclei in the mass region $140 \leq A \leq 200$ [29]. However no information is known about g_R values in the super-heavy region.

2.7 Electromagnetic decay

2.7.1 γ decay

A nucleus X decaying from a state of collective or single particle excitation which does not result in a change in the nuclear structure such that

$$X^* \rightarrow X + \gamma \tag{2.28}$$

can release the energy as a γ ray. The γ ray of given $\sigma\lambda$ relates to a magnetic (σ = M) or electric (σ = E) transition within the nucleus of multipole ordering λ (i.e. λ = 1(dipole), 2(quadrupole) etc.). Spectroscopic study of these γ rays enables us to map the energy levels in which a specific nucleus can exist, revealing intricate single particle structure and collective behaviour. Considering the electromagnetic transition from states with angular momenta I_i to I_f, selection rules relating to multipolarity $\sigma\lambda$ of the transition are given as

$$\mid I_f - I_i \mid \leq \lambda \leq \mid I_f + I_i \mid, \tag{2.29}$$

$$\Delta\pi(E\lambda) = (-1)^{\lambda}, \Delta\pi(M\lambda) = (-1)^{\lambda+1}, \tag{2.30}$$

dictating possible initial and final angular momenta and change in parity $\Delta\pi$ between states. For a considered electromagnetic transition leading to a photon emission the total transition probability is given as

$$T(\sigma\lambda; I_i \rightarrow I_f) = \frac{8\pi(\lambda+1)}{\hbar\lambda[(2\lambda+1)!!]^2}\left(\frac{E_\gamma}{\hbar c}\right)^{2\lambda+1} B(\sigma\lambda; I_i \rightarrow I_f), \tag{2.31}$$

where all the information about the transition in terms of the nuclear structure is given in the reduced transition probability $B(\sigma\lambda; I_i \rightarrow I_f)$ [29].

One useful way of calculating the decay rates in Equation 2.31 is to obtain reduced transition probabilities using an extremely simplified independent particle model. By assuming radiation is emmitted due to the transition of a single non-interacting proton

occupying single particle energy levels, then the Weisskopf estimates for a transitions half-life may be found [30]. By comparing these with observed half-lives, significant deviations from this model may be infered, such as transitions due to collective motion or the existance of isomeric states (see Section 2.5).

Comparison between experimental data and the collective rotational model of the nucleus may be achieved by using this model to find the reduced transition probabilities [29]. Considering strongly coupled rotational bands decaying in a $K \neq 0$ nucleus, the $B(E2)$ is given in relation to the nucleus' charge distribution, defined in relation to its electric quadrupole moment Q_0, as

$$B(E2; KI_i \rightarrow KI_f) = \frac{5}{16\pi} e^2 Q_0^2 \langle I_i K 20 | I_f K \rangle^2. \tag{2.32}$$

That of an $M1$ transition is determined from the g factors (see Section 2.6) of both its intrinsic nucleonic motion, g_K, and also its collective rotation, g_R, as

$$B(M1; KI_i \rightarrow KI_f) = \frac{3}{4\pi} \left(\frac{e\hbar}{2Mc} \right)^2 (g_K - g_R)^2 K^2 \langle I_i K 10 | I_f K \rangle^2. \tag{2.33}$$

Here the magnetic transition probability falls to 0 if $g_K = g_R$ as the magnetic moment becomes simply $g_R I$ and a constant of motion. Using these reduced transition probabilities, intensity ratios between competing transitions from within a rotational band may be found from Equation 2.31.

2.7.2 Internal conversion

Internal conversion is an electromagnetic process which competes with γ-ray emission, whereby a nuclear transition directly liberates an atomic electron emitting it from the atom. This may then be followed by one or more X rays as the electron hole is refilled by outer atomic electrons. The possible energies of the emitted electron E_{ce} from a converted transition, are discreet and found as the energy of the nuclear transition ΔE minus the quantised binding energy of the atomic electron emitted BE giving

$$E_{ce} = \Delta E - BE. \tag{2.34}$$

The conversion coefficient gives the decay probability ratio between a nuclear de-excitation being converted, λ_e, and proceeding via a γ decay, λ_γ, and may be calculated in relation to the multipolarity of the transition (i.e. M1, E1, etc.), the energy of the transition and the Z of the nucleus. Emission of atomic electrons from different shells have different decay rates (λ_K, λ_L and so forth) and these are represented by their associated conversion coefficients α_K, α_L. These sum to give the conversion coefficient α for the total rate of conversion λ_e given as

$$\alpha = \frac{\lambda_K}{\lambda_\gamma} + \frac{\lambda_L}{\lambda_\gamma} + ... = \frac{\lambda_e}{\lambda_\gamma}. \tag{2.35}$$

The details of the calculations of conversion coefficients can be found in [31] but will not be discussed here. Calculated α values display certain trends so that they are seen to play a significant role when studying super-heavy elements. Firstly, the coefficients increase as $\propto Z^3$ so a high proportion of converted transitions are expected for nuclei in the region of $Z \sim 100$. Secondly, the coefficients increase as the energy of the transition decreases. The collective rotational excitations seen in the super-heavy region will lead to lower energy transitions and again, a greater proportion being converted.

Chapter 3

Experiment and data analysis

3.1 Experimental setup

The experimental setup used at the accelerator laboratory in Jyväskylä is shown in Figure 3.1 and was used for the separation and detection of ^{252}No nuclei by means of recoil decay tagging methods. The setup consists of a target position with the JUROGAM Ge array surrounding it, measuring promptly emitted γ rays. The production of nuclei takes place at this target position via a reaction with a beam of nuclei accelerated by a cyclotron. Products are subsequently separated by the gas filled separator RITU. They are finally implanted in the GREAT focal plane array for identification and detection of subsequent decays.

3.1.1 Super-heavy nuclei production

Production of nuclei above Z = 100 require the fusion of two heavy nuclei and in the experiment this took the form of a fusion-evaporation reaction using a beam incident onto a target. This may be represented by

$$A + B \rightarrow C^* \rightarrow D + x\mathrm{n} \tag{3.1}$$

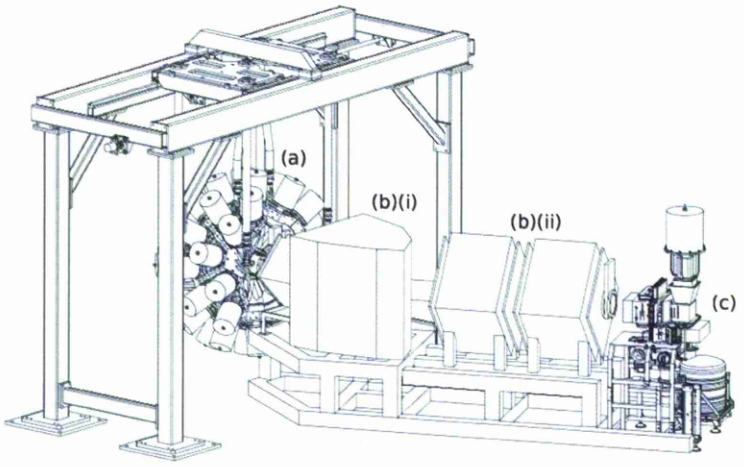

Figure 3.1: Separation and detection setup at the accelerator laboratory Jyväskylä. In-beam JUROGAM germanium array (a) at target position with the gas filled separator RITU (b)(i) and (b)(ii) showing the quadrupole and two of the subsequent dipole magnets respectively. The recoils are implanted in the GREAT focal plane spectrometer (c).

where the excited compound nucleus C^* may emit a number of excess neutrons xn after formation. Further de-excitations occur in energy and angular momentum from the emission of γ rays and conversion electrons to form a ground or isomeric state nucleus. However, cross-sections to produce these super-heavy evaporation residues are low, due to the high probability of the compound nucleus fissioning before de-exciting.

The ^{206}Pb(^{48}Ca, 2n)^{252}No reaction was employed using a ^{206}Pb rotating target of thickness 452 μg/cm^2. Cross sections of 290 nb and 130 nb have been found for the production of ^{252}No in the ground state and 8^- isomeric states respectively [24]. However, due to systematic uncertainties these values could be up to ~50% out. The ^{48}Ca beam was provided by the K130 cyclotron at an energy of 218 MeV and average current 30 pnA for approximatly 211 hours in total.

3.1.2 RITU recoil seperator

The production of low cross section super-heavy nuclei means that the number of desired recoils produced is always outweighed by events such as unwanted reaction products and unreacted beam. Pre-analysis separation of these is crucial and the design of the seperator used is dictated by the experimental requirements. The gas filled seperator works on the principle that when a heavy ion travels through a dilute gas, it will aquire an average charge state q_{ave} [32]. Using the Thomas-Fermi model of the atom, the average charge state of such an ion in terms of elementary charge e can be given as

$$q_{ave} = \frac{v}{v_0} e Z^{1/3} \tag{3.2}$$

where v and Z are the velocity and charge of the ion respectively, and $v_0 = (c/137)$ is the Bohr velocity. If this ion is also passing through a constant magnetic field B it will follow a circular trajectory with radius R so that

$$B \cdot R = \frac{mv}{q_{ave}} = \frac{mv}{(v/v_0)eZ^{1/3}} = \frac{0.0227A}{Z^{1/3}}(\mathrm{Tm}). \tag{3.3}$$

As the radius of trajectory depends on the charge state of the ion at any one time, it is necessary for the number of collisions, and therefore exchange of atoms electrons, to be large. This will give a small distribution of q_{ave} values for the ions passing through the gas and a smaller variation in trajectory. The radius then given is not dependent on the recoils velocity or initial charge state, so that B may be tuned to give the required trajectory to select a specific nucleus of Z and A. As all initial charge states and velocities of recoils are collected together, the transmission efficiencies observed for gas filled separators are good, but their mass resolution is poor compared with other seperator setups.

Studying super-heavy nuclei tends to be associated with low cross sections and few competing production channels along with good focal plane decay identification. Therefore, a large transmission of desired products is vital and mass resolution may be sacrificed. Gas filled separators fill these criteria and are a suitable experimental choice. At the Accelerator laboratory in Jyväskylä, the RITU gas filled separator [33] was constructed for, amongst other things, the study of super-heavy nuclei. It separates and focuses the products using dipole (D) and quadrupole (Q) magnets respectively and is of type QDQQ. An additional quadrupole was added to the conventional DQQ structure to initially focus the reaction products before separation, for better matching to the acceptance of the dipole magnet.

3.1.3 GREAT focal plane detector array

GREAT is a focal plane array located at the end of the RITU separator, the constituents of which are shown in Figure 3.2 and will each be described in this section [34]. The array serves two purposes; firstly, the identification of recoils entering through a multiwire proportional counter and implanting on a double-sided silicon strip detector (DSSSD). Secondly, to measure any subsequent delayed decays in the form of α particles, spontaneous fissions, γ rays, X rays, β particles or conversion electrons. These decays are used for identification of the recoils, but may also be of experimental interest themselves.

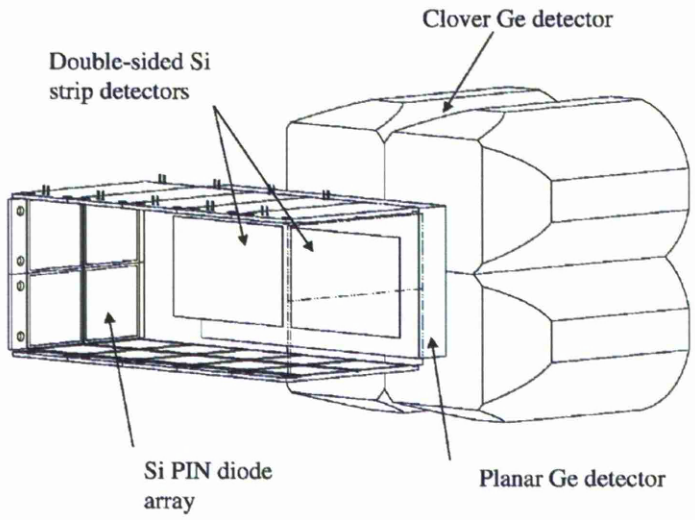

Figure 3.2: Schematic representation of the GREAT array with all detector components labeled. Recoils enter from the left out of the MWPC which is not shown. Figure taken from [34].

Multiwire Proportional Counter

Immediately upstream of GREAT, is a multiwire proportional counter (MWPC) with aperture 131 mm (horizontal) $\times$ 50 mm (vertical). The MWPC is filled with isobutane and has two thin Mylar entrance and exit windows separating it from the low pressure gas of RITU and the vacuum of the subsequent GREAT detectors. Incoming recoils are identified using their energy loss signal within the MWPC, along with the energy from their implantation onto the DSSSD and time of flight between the two (detailed in Section 3.3.1). An energy loss signal in the MWPC, also serves as a veto to distinguish between events in the DSSSD caused by incoming recoils implanting and those caused by a subsequent delayed decay which will not give a MWPC signal.

Double Sided Silicon Strip Detector

The recoils are finally implanted onto two double sided silicon strip detectors positioned adjacent giving ~85% recoil collection efficiency [34]. In total it consists of 120 horizontal (DSSSD-X) and 40 vertical (DSSSD-Y) strips giving 4800 pixels. This pixelation enables any alphas, spontaneous fissions, protons or electrons emitted by a decaying nucleus to be detected in the same pixel as that of the implantation. This then enables the whole event, including in-beam data, to be studied. The detectors are cooled to -20 °C and each DSSSD has an active area of 60 mm × 40 mm and a thickness of 300 μm. The DSSSD-X and Y channels are set to high and low gains respectively. This allows for the energies of decays to be determined up to ~1 MeV in the X channels and 1 to ~17 MeV in the Y channels.

PINS

Arranged upstream of the DSSSD are 28 silicon PIN diodes. Due to recoils implanting onto the surface of the DSSSD, some decay particles will be emitted back out and will therefore not be detected in the DSSSD. The PIN diodes are arranged to detect these with ~30% geometrical efficiency.

Segmented Clover and Planar detectors

To measure X rays and γ rays from the delayed decays of recoil implantations, the planar and clover germanium detector arrays are used. The planar is a double sided germanium strip detector placed 10 mm downstream of the DSSSD within the vacuum chamber of GREAT. It has an active area of 120 mm × 60 mm and detects X rays and lower energy γ rays. The clover detector consists of four germanium crystals each with four fold segmentation. They are placed behind the planar detector outside the vacuum chamber and measure higher energy γ rays. The efficiencies of both germanium arrays are shown in Figure 3.3 plotted as a function of γ-ray energy.

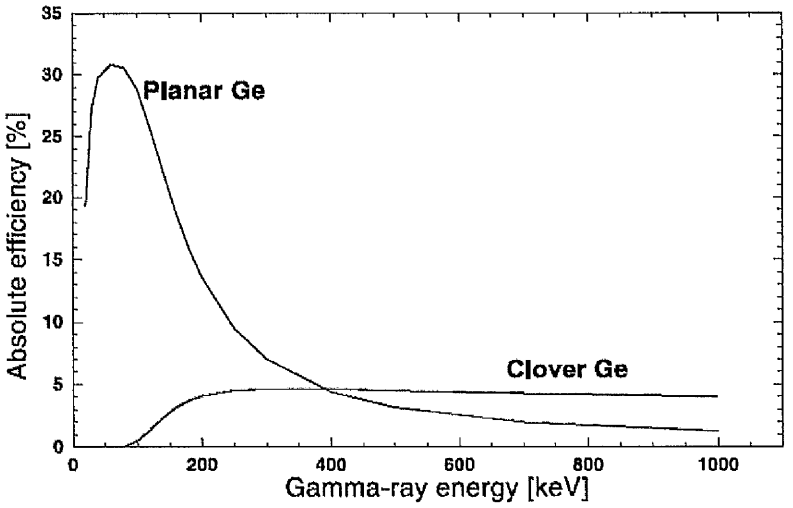

Figure 3.3: Efficiencies of both the Planar and Clover germanium arrays plotted as a function of γ-ray energy taken from [34].

3.1.4 JUROGAM in-beam array

Prompt γ rays emitted shortly after the formation of nuclei at the target position are measured using the JUROGAM array. This consists of 43 high purity germanium (HPGe) detectors, arranged to cover as high a fraction of the 4π solid angle around the target position, as possible.

One of the problems encountered when performing γ-ray spectroscopy, is the compton scattering and subsequent escape of γ rays within a detector, leading to an increase in the background. This problem is, to some extent, amended by the use of compton suppression detectors. These surround the germanium detectors of JUROGAM so that an escaping scattered γ ray will then pass through the suppression detector creating a signal that will veto any signal from the germanium [35].

3.2 Energy calibrations

Biased Si and Ge detector signal processing systems are calibrated to translate their digital data output into a correct energy value by using radioactive sources of known radiation energy. The sources were placed externally and the energy values taken from the Firestone Table of isotopes [36]. A calibration function was obtained of the form

$$E = a + bx + cx^2 + dx^3, \tag{3.4}$$

where x is the digital channel number output and E is the energy of the radiation in keV. Equation 3.4 is shown as a cubic polynomial up to coefficient d, but functions may be found up to only linear or quadratic, depending on the detectors used and the requirements for accuracy.

3.2.1 Si detector calibrations

A triple α source of ^{239}Pu (E_α = 5156.59 keV), ^{241}Am (E_α = 5485.56 keV) and ^{244}Cm (E_α = 5804.82 keV) was used to calibrate the low gain DSSSD-Y channels and conversion electrons from a ^{133}Ba source used for the high gain DSSSD-X channels and PIN detectors. The α particles from the externally placed source experience losses before detection as they pass through a dead layer of the DSSSD detector. This leads to higher values given by the calibration function for α energies emitted by directly implanted recoils where there are no losses. The α energies measured in the DSSSD-Y channels from implanted recoils will also include an energy contribution from the recoiling nucleus, which is not present when using the external source. This factor will again lead to higher energy values being measured. However, these detectors are used for identifying decays from recoils for tagging purposes and not for spectroscopic means. Therefore, this effect will not be a problem. Because of this, just a simple linear fit was required for the Si detectors. Figure 3.4 shows the calibrated calibration spectra of the triple α source from all the DSSSD-Y strips combined.

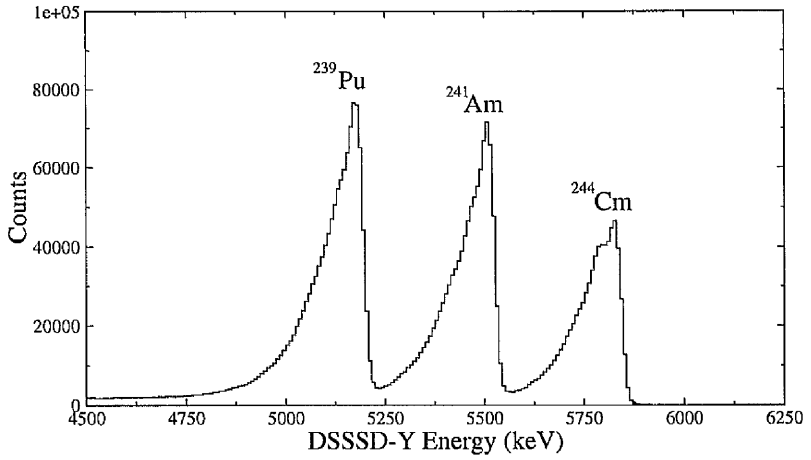

Figure 3.4: Calibrated calibration spectrum from all DSSSD-Y channels using a triple α source.

3.2.2 Ge detector calibrations

As one of the main purposes of the data analysis is γ-ray spectroscopy, the accuracy of the Ge calibration functions is key. ^{133}Ba and ^{152}Eu γ-ray sources were used to calibrate the energies of the Clover and JUROGAM detectors and X rays and γ rays from a ^{133}Ba source were used for the higher gain PLANAR detectors. The Planar and JUROGAM detectors were calibrated using a quadratic function and the Clover detectors using a cubic fit, all of which lead to deviations from known energies of calibration peaks of less than 0.5 keV. The energy calibrated spectrum for all the JUROGAM detectors combined, is shown in Figure 3.5 for the calibration run at the start of the experiment. A selection of the fourteen peaks used for the fit are highlighted. The calibrated energy of the 356.13 keV peak was compared between the calibration runs taken at the start and end of the experiment and the value was seen to almost invariably decrease. This decrease however, was seen to be below 0.5 keV for all detector channels, so no correction for this shift was necessary.

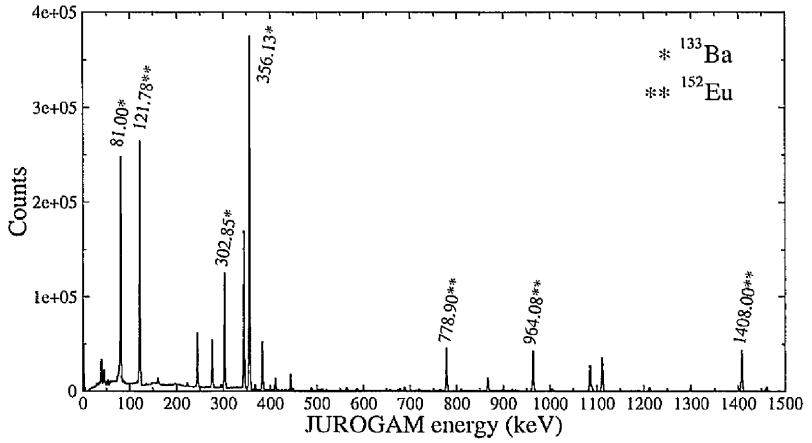

Figure 3.5: Calibrated calibration spectrum for all JUROGAM detector channels with selected peaks, used for calibration, highlighted.

3.2.3 Doppler correction

The reaction products move through the JUROGAM array with velocity $\beta(=v/c)$ causing the energy of any prompt γ rays detected in the lab frame of reference, E', to be significantly doppler shifted from its energy in the recoils frame of reference E. The γ-ray energy must be converted to the recoils frame using the non-relativistic formula

$$E_\gamma = \frac{E'_\gamma}{(1 + \beta cos\theta)}, \tag{3.5}$$

where θ is the angle subtended by the γ ray from the direction of β. The θ value is set for each detector in the array, but due to a solid angle being subtended by each detector and also a distribution of β values for products, an addition to the broadening of γ-ray peaks in spectra is seen due to the doppler shifting and subsequent correction. Using principles of conservation of momentum between the ^{48}Ca beam and ^{252}No products, the β value was found to be 0.0187. This allows us to use the non-relativistic formula as $\beta \ll 1$. Losses in the target mean that β will be lower than this, so by taking this value for the correction we are over compensating for the

doppler shifting. However, it is found that to produce a 1 keV shift in the corrected value of a 300 keV γ ray emitted in the recoil frame detected at $\theta = 157.6°$, (the angle of JUROGAM detector which produces the greatest doppler shift), the velocity must be degraded to a value of $\beta = 0.0152$. This would require an energy loss of 14.3 MeV by the ^{252}No, 76.0 MeV by the ^{48}Ca or 7.2 MeV and 38.0 MeV respectively for example, if losses were incurred by each. Calculations suggest energy losses much lower than this would be expected in the target [37].

3.2.4 JUROGAM efficiency

Relative intensities between γ rays emitted are vital tools in the analysis of spectra and a reliable efficiency function is therefore required for, in relation to the requirements of this experiment, the JUROGAM array. The intensities of the ^{133}Ba and ^{152}Eu γ rays from the calibration were used to find the relative efficiency when scaled with the intensities with which they are emitted [36]. The efficiency was fitted to the function

$$\text{efficiency}(E_\gamma) = exp[(A + Bx + Cx^2)^{-G} + (D + Ey + Fy^2)^{-G}]^{-1/G}, \qquad (3.6)$$

where $x = \ln(E_\gamma/100)$ and $y = \ln(E_\gamma/1000)$ [38]. The coefficients A to C define the low energy region and D to F that of the high energy with G then dictating the crossover. The fitted relative efficiency of the JUROGAM array is shown in Figure 3.6 with coefficient parameters given.

3.3 Recoil-decay tagging techniques

Performing γ-ray spectroscopy on an experiment with low cross sections requires detailed identification of the specific desired recoil evaporations, so that any results may be distinguished above the overwhelming background produced. This involves tagging events with the use of multiple energy and timing gates. Here, decay events from the recoiling nuclei and those from their subsequent implantation are only considered if they occur within these specific set ranges which identify them as decays

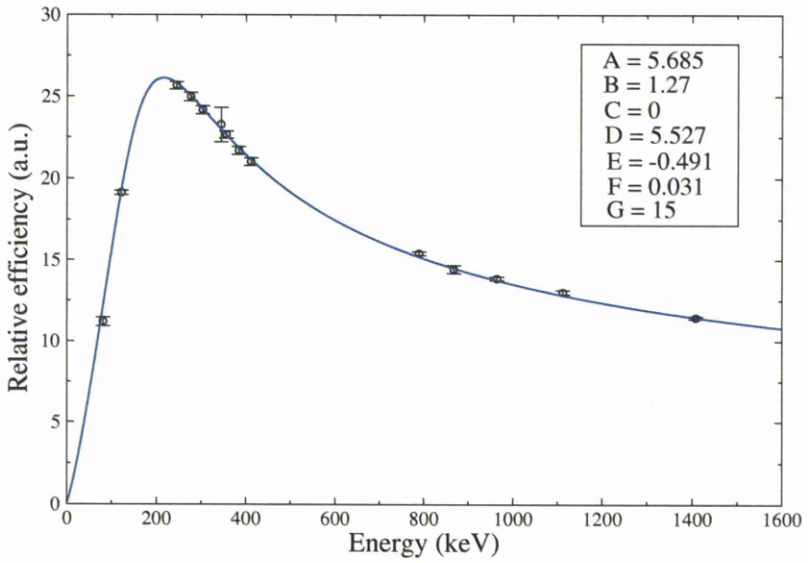

Figure 3.6: Relative efficiency of γ-ray detection for the JUROGAM array.

from a ^{252}No reaction product. A schematic representation of a single recoil travelling through the setup is shown in Figure 3.7, where selection of the recoil is made by using the different energies indicated and the time differences between events.

3.3.1 Recoil tagging gates

The recoiling products pass through the MWPC giving an energy loss (dE) value for each recoil implantation into the DSSSD which in turn gives a residual recoil energy value E. The time of flight (tof) for the recoil is given as the difference in time between the MWPC and the DSSSD signals t_o-t_o'. Three 2D histograms may be plotted using these variables to define each recoil in 3 dimensional variable space. Figures 3.8(a to c) show the histograms for all events entering the MWPC during the experimental run and Figures 3.8(d to f), (colour intensity scale enhanced), show the same histograms but only including those events which are identified as ^{252}No nuclei via their subsequent alpha or spontaneous fission decays in the DSSSD. Events corresponding to scattered beam and transfer products are not present in these

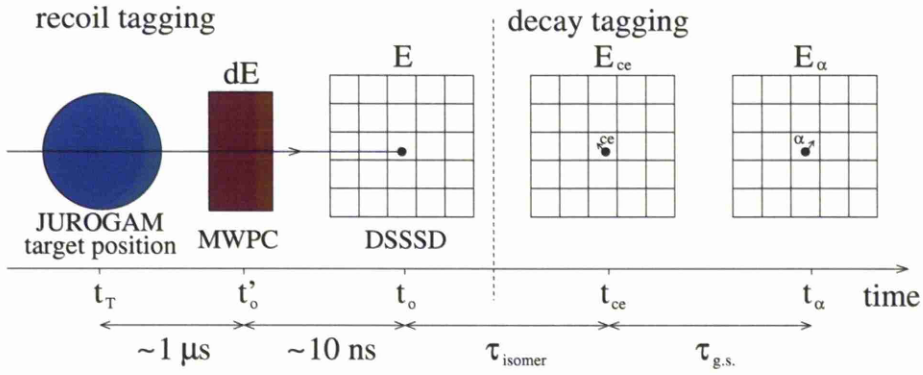

Figure 3.7: Recoil passing through the experimental setup before implanting in a pixel of the DSSSD and subsequently decaying. Time and energy signals used for tagging purposes are shown for a recoiling nucleus in an isomeric state.

histograms and only the region in each where ^{252}No recoils appear is then given. The 2D gates used for recoil tagging are then set corresponding to these regions shown. Recoils tagged using only these 2D recoil gates will be referred to as recoil tagged (RT) events.

The prominent intensities seen in Figure 3.8(a) at around tof = 2000 to 3000 are thought to be electrical phantoms. Only ~15% of these events have an associated energy deposition E in the DSSSD, compared with ~ 85% of those tagged in the neighbouring background region at tof = 4000. Also only background JUROGAM activity is observed associated with these events.

3.3.2 Decay tagging gates

After recoils implanting onto the DSSSD have been recoil tagged, they may be further identified from their subsequent decays which will occur in the same pixel as the implantation. Figure 3.9 shows the DSSSD-Y spectrum in anti-coincidence with the MWPC. This eliminates energies of implanting recoils and just gives their decays. The spectrum and energy gate values have been corrected for the effects described in

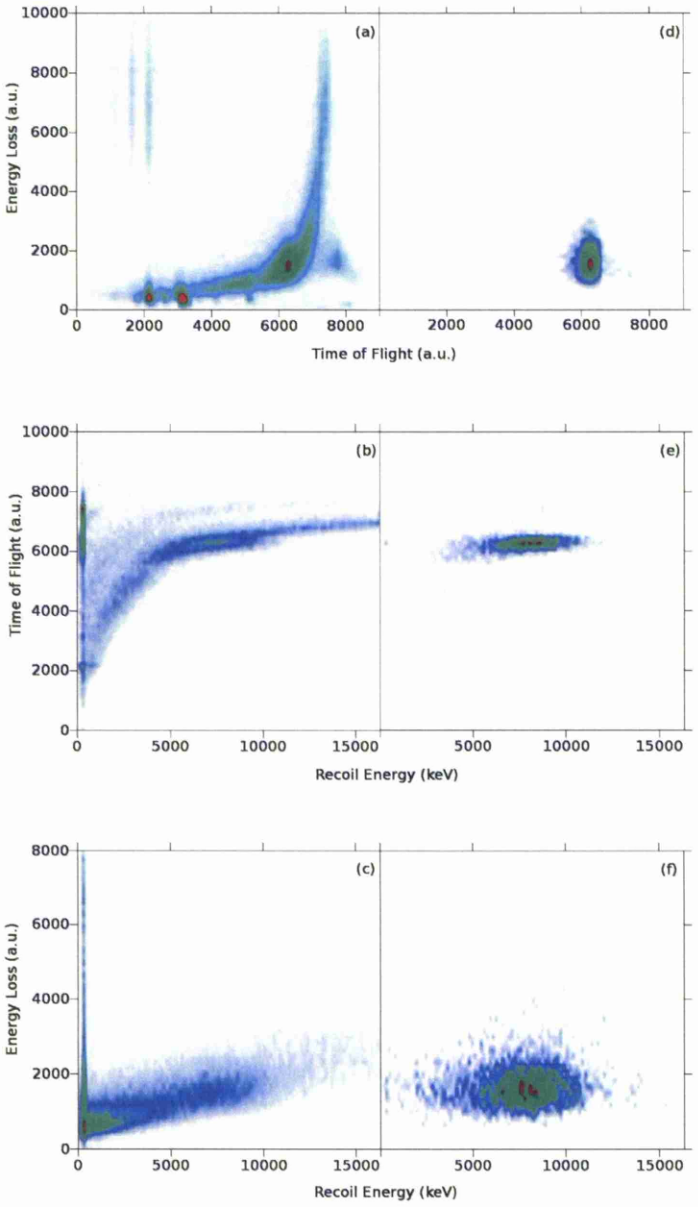

Figure 3.8: 2D histogram plots of tof vs dE (a), E vs tof (b) and E vs dE (c) for all incoming recoils. Respective plots (d) to (f) show recoils which subsequently decayed via α or spontaneous fission from the ^{252}No ground state.

Section 3.2.1 which caused the energies to appear ~100 keV above known values due to the use of an external calibration α source and additional energy of the recoiling nucleus. This was done by using the well known $^{252}No_{\alpha}$ energy (E_{α} = 8415 keV) to correct the energy calibration, using it as an internal source. A ^{252}No recoil is α decay tagged in the DSSSD-Y using an energy gate between 8315 $\rightarrow$ 8510 keV in anti-coincidence with the MWPC, only if it is seen to decay in the same DSSSD pixel as a recoil tagged implantation. The time between the recoil implantation, t_o, and the α decay, t_{α}, must also be between 0 and 20 s covering 8.33 half-lives of the ^{252}No nucleus for it to be considered a RDT event. Due to an efficiency of $\sim$ 50% (see Section 5.1.2) for the DSSSD detecting α decays, tagging of subsequent α particles in the decay chain is used to enhance statistics. The subsequent ^{248}Fm and ^{244}Cf decays are gated on between 7763 $\rightarrow$ 7941 keV from 0 to 240 s (6.66 half-lives), and 7141 $\rightarrow$ 7271 keV from 0 to 3500 s (3 half-lives) respectively. The number of half-lives over which each decay tag is accepted is a compromise between increasing statistics and limiting the expected number of random correlations (see Section 5.1.2). Double counting of events is prevented by accepting only the first decay observed in the α chain.

A spontaneous fission decay branch of b_{SF} = 32.2(5)% [39] is seen in ^{252}No which may also be used for the decay tagging of events. The energies of these decay events will be a broad distribution centred on around 160 MeV. This is well above the dynamic range set for the DSSSD-Y channels, so these events appear as 'overflow' signals around the upper limit at $\sim$ 17 MeV. Therefore, an energy gate of >15 MeV at a time from 0 to 20 s after implantation is used to identify ^{252}No spontaneous fission events.

Identifying those tagged ^{252}No nuclei that were created in the 8^- K-isomeric state [24] is a key part of the analysis. This is done by exploiting the decay of nuclei from isomeric states through lower order, highly converted, transitions to the ground state, whereby conversion electrons (ce) may be detected [17]. Recoil-ce-decay tagged (R-ce-DT) events are those which have been RDT as described above, but with the extra

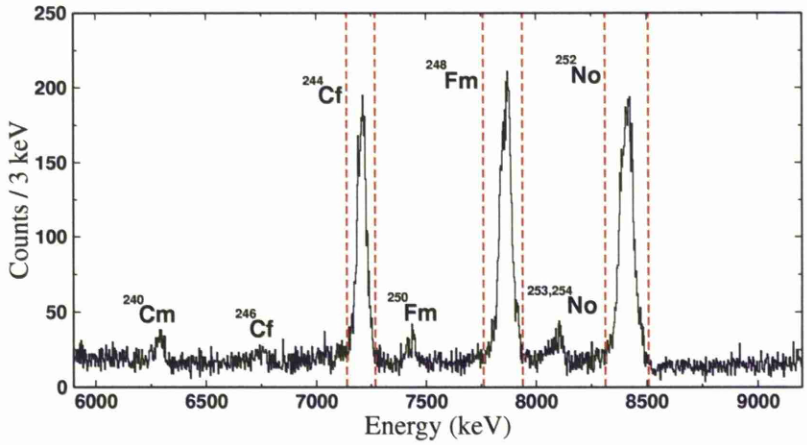

Figure 3.9: DSSSD-Y spectrum in anti-coincidence with the MWPC signal. Energy gates used for α decays are highlighted.

condition of a conversion electron detected between implantation and ground state decay all in the same pixel. The spectrum of detected conversion electron cascades in the DSSSD-X channels from these events are shown in Figure 3.10. The E_{ce} is gated between $37 \rightarrow 500$ keV and the time between t_0 and t_{ce} up to 0.7 s (6.3 isomeric half-lives). For isomeric events identified via recoil-ce tagging (R-ce-T), i.e. not requiring a subsequent ground state decay, a time gate of $650\mu s \rightarrow 0.7s$ was used. This was to eliminate events of a sparsely populated isomeric state found to have $t_{1/2} = 103(15)$ μs and which subsequently decayed with α energy of ^{253}No or ^{254}No. As this does not fit any of the known half-lives of isomeric states in these nuclei, it is likely that several states were populated.

3.3.3 JUROGAM time gates

When measuring in-beam data using the JUROGAM array from tagged recoils, prompt γ rays at the target position will precede the implantation and therefore must be selected using time gates. A finite transmission time between the recoil at the target position, t_T, and when it implants onto the DSSSD, t_0, means that, when

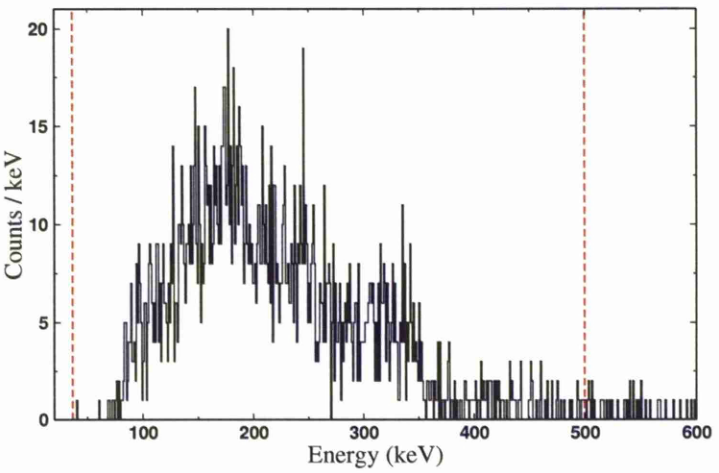

Figure 3.10: Conversion electron spectrum in DSSSD-X channels used for R-ce-DT events. The conversion electron energy gate set is also shown.

plotting the number of JUROGAM events against time preceding all tagged implantations, then an increase in γ-ray events above background is seen to correspond with the tramission time, shown for one detector in Figure 3.11. The peak of events represents the prompt X rays and γ rays from the tagged nuclei allowing individual time gates to be set for accepting desired JUROGAM events for each of the 43 detectors, as is highlighted in the Figure.

3.4 Data acquisition system

The electronics and data collection at JYFL works on the system of total data readout (TDR) [40]. This system involves data from each detector channel being independently stored, giving a triggerless acquisition system which virtually eliminates dead time losses. The data is then analysed entirely off line and requires each piece of data to be time stamped when collected, using a synchronised 100 MHz clock system. As well as reduction of dead time, TDR enables greater versatility in offline analysis.

Data from the JUROGAM detector channels was collected using the TNT data

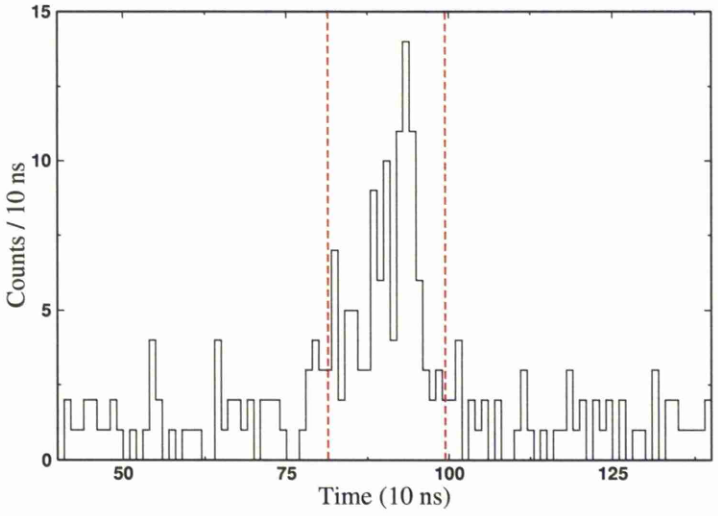

Figure 3.11: Events in one JUROGAM detector at time preceding the implantation for all RDT events. The time gate set is also shown.

acquisition system. The system digitises the signal at an earlier stage than that for TDR and provides the possibility for greater data collection rates.

Chapter 4

Analytical methods for γ-ray and X-ray spectra

A key aspect of the spectroscopic study of nuclei, is to use spectra in assigning structures of single particle excited states. Here, experimental results can guide the way for theoretical study by illuminating the ordering and energy of single particle levels within the many body nuclear system. A well established technique to do this utilises the experimentally observed ratio between interband and intraband transitions from a level within a rotational band built on the state. However, the low cross-sections associated with superheavy nuclei production often means the interband transitions are weak or missing.

This chapter presents two methods devised to fully utilise low statistic spectra in assigning structures of single particle excitations. These represent full statistical analyses of the available data giving p-value probabilities for the consistency between the experimental results and the possible assignments for the configuration. The methods will be illustrated using a simulated schematic spectrum of a rotational band system and also applied to previously obtained results for ^{250}Fm and ^{254}No. These results show the validity of the methods to be applied to the present data.

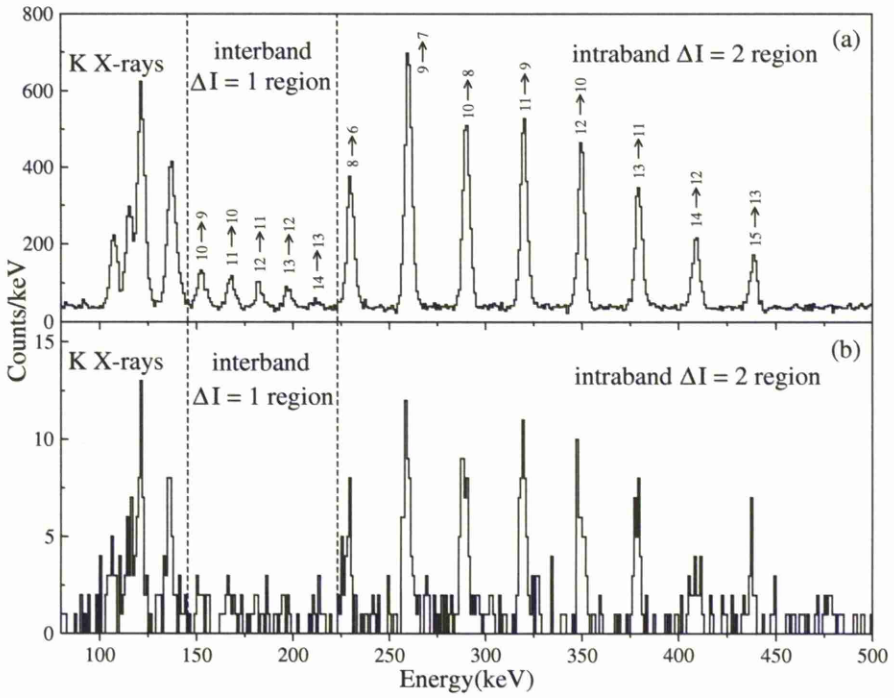

Figure 4.1: Schematic rotational band γ-ray transitions simulation of a hypothetical isomer with added background. Shown for high statistics in (a) and 60 times lower statistics in (b). Values of $Q_0 = 12.98$ eb, $g_K = +0.2$ and $g_R = 0.407$ were used.

4.1 Conventional method

Intensity ratios between competing transitions in a rotational band, can be compared with those theoretically expected for different isomeric structures to assign a configuration. Figure 4.1(a) shows a simulated γ-ray spectrum schematically adhering to the decays from strongly coupled rotational bands populated above a $K \neq 0$ isomeric state with added background. The theoretical γ-ray intensities for the possible transitions from a level I_i within the rotational band, as illustrated in Figure 4.2, may be found by first getting the reduced transition probabilities from Equations 2.32 and 2.33 for E2 and M1 transitions respectively. The γ-ray intensities are then found using the total transition probabilities from Equation 2.31 so that the theoretical ratio

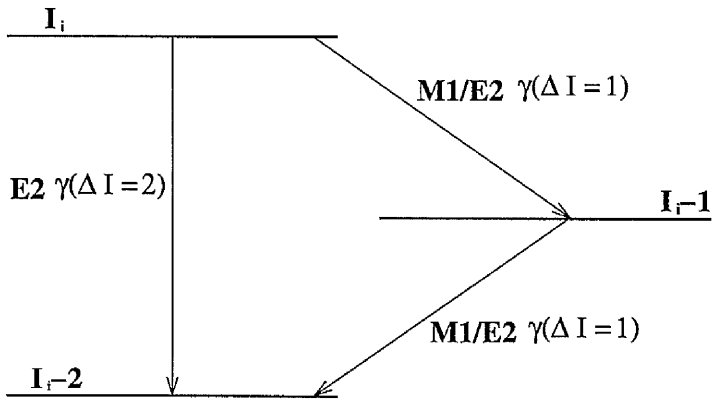

Figure 4.2: Possible γ-ray transitions from a level I_i in strongly coupled rotational bands built on a $K \neq 0$ state.

between interband ($\Delta I = 1$) and intraband ($\Delta I = 2$) γ-ray transition intensities from an initial level I_i is given as

$$R_{I_i} = \frac{T(M1; \Delta I = 1)_{I_i} + T(E2; \Delta I = 1)_{I_i}}{T(E2; \Delta I = 2)_{I_i}} = \frac{(g_K - g_R)^2}{Q_0^2}.F(I_i, K) \qquad (4.1)$$

which is found simply from the g_K, g_R and Q_0 of the nuclear state and a function of the K of the band and the I_i of the transition. Here the values of the nucleus' electric quadrupole moment, Q_0, may be found from its deformation and the I_i of the level and K of the band, known from spectroscopic analysis. As discussed in Section 2.6, the g_R factor may be estimated as the nucleus' ratio of Z/A and the g_K factor provided by the single particle excitation. It is therefore possible to use the g_K factors from various excited configurations that are predicted to be responsible for a state and find their corresponding theoretical inter/intraband γ-ray ratio R_{Ii}. Figure 4.3 shows this R_{Ii} value as a function of g_K for the $I_i = 11$ level within the simulated spectrum. The simulation used a hypothetical isomer based on a $K = 6$ state in a ^{246}Fm nucleus where values of $Q_0 = 12.98$ eb and $g_R = 0.407$ were set. It may be noted that the R drops to a minimum when $g_K = g_R$, as magnetic transitions are not possible. The value does not become zero however, due to the interband transition

proceeding via folded E2 and M1 mulitipole components so that the electric transition is still therefore present. The ratio between these two interband intensities is defined as the mixing ratio which is given as

$$\delta = \frac{T(E2; \Delta I = 1)}{T(M1; \Delta I = 1)}. \tag{4.2}$$

Highlighted are g_K factors of +0.2 (used in the simulation) and 0.0. These theoretical ratios can be compared with the observed ratio R_o between inter/intraband γ-ray fitted intensities from the high statistics simulated spectrum, which has also been shown in the Figure 4.3. This shows consistency with the $g_K = +0.2$ value for the state, and hence its configuration, as the statistics are high enough for the uncertainty in R_o to be low.

This method has previously been employed successfully in the assignment of isomeric states [22, 21] but, as will be shown, this approach is often inconclusive as a result of low statistic spectra.

4.2 Method: Cumulative γ-ray branching ratios

An extension to this method, applicable for low statistics, may be illustrated using the simulated spectra in Figure 4.1 with (a) showing high statistics, where peaks may be clearly fitted in both the interband and intraband γ-ray regions. Spectrum (b) is of the same rotational band but with 60 times less statistics than (a). Here the intensities of the intraband γ-ray transitions may still be fitted reasonably well, but the interband γ-ray peaks are now largely indistinguishable from the background. Clearly, we cannot find observed R_o values between transitions, but we may use fitted intensities in the intraband γ-ray region along with theoretical R values for a proposed structure, to find the expected number of counts in the interband γ-ray region from a corresponding γ-ray transition. By finding this expected number of counts using γ-ray intensities $\mathcal{I}(\Delta I = 2)$ for all corresponding interband γ-ray transitions expected within the clear region (highlighted in Figure 4.1), a total number of expected counts

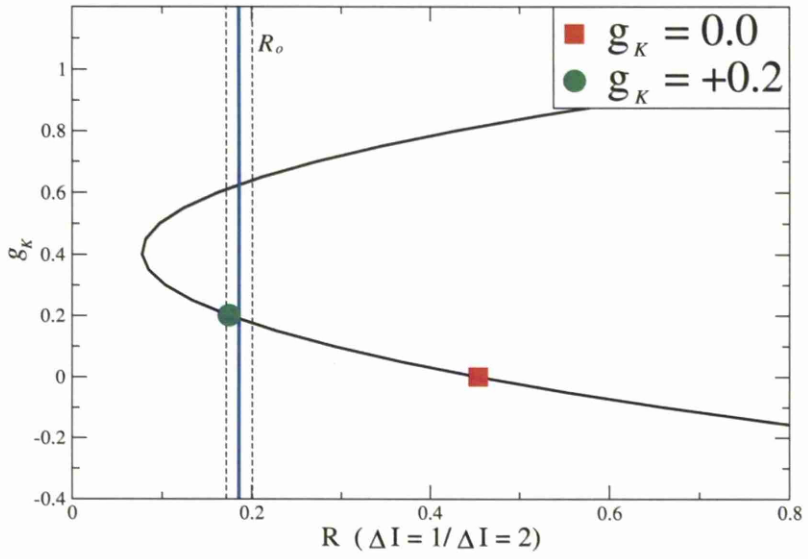

Figure 4.3: Inter/intraband γ-ray transition ratio as a function of g_K factor with two g_K factors highlighted. Compared with observed ratio R_o from high statistics simulated spectrum for $I_i = 11$.

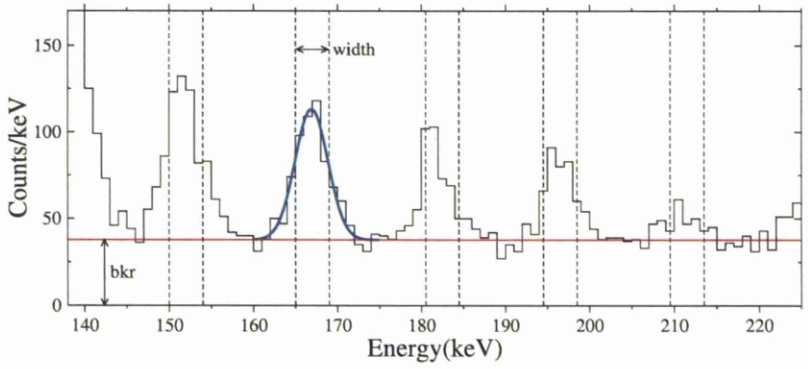

Figure 4.4: High statistic interband region with highlighted energy ranges used to obtain N_o (dashed line) and background rate estimate (red line). Range widths of 4 keV were used and the fitted gaussian of the $I_i = 11$ transition is shown (blue line).

corresponding to a structural assignment can be found. This value may be compared with the observed total number of counts N_o for interband γ-ray transitions, but as no peaks may be fitted, then the total number of counts across energy ranges centred on transition energies within the interband γ-ray region, must be used. This is illustrated in Figure 4.4 for the high statistics simulated case where counts over 4 keV ranges are taken over the five interband transitions within the clear region. The fitted gaussian distribution of the $I_i = 11$ peak is shown and in a low statistics case would represent a probability distribution for which counts would appear. The expected number of counts must therefore be scaled by a factor f representing the proportion of this distribution within the range of width chosen, considering also the width of peaks expected within the spectrum at that energy. The energy width is selected so that f is close to 1 in order to include as many counts as possible, but not too large as to greatly increasing the additional background. The total expected counts, must also include a background estimate so that it may be given as

$$N_s = \left(\sum_{I_i} (\mathcal{I}(\Delta I = 2)_{I_i} \cdot R_{I_i} \cdot \varepsilon(E_{I_i}) \cdot f) \right) + B_{tot}. \tag{4.3}$$

Here B_{tot} is the total expected background found as the product of an estimate of background/keV within the interband region and the total combined energy range over which N_o is taken. The ratio between detection efficiencies at $E_\gamma(\Delta I = 1)_{I_i}$ / $E_\gamma(\Delta I = 2)_{I_i}$ is given by $\varepsilon(E_{I_i})$ so that N_s gives the expected value of counts for a structural assignment, s.

In obtaining a value for the observed counts N_o in the interband region to compare with the theoretical N_s, we must take total counts over energy ranges centred on the γ-ray energies. If at least one interband transition energy may be reliably fitted, then the assumed transition energies of the rest may be found from the intraband energies. However, if no interband peaks may be fitted, then the energies can be estimated using the kinematic moment of inertia from a level I_i using the energy of

the intraband transition from the same level. Using Equation 2.19 this is found as

$$\Im^{(1)} = \hbar^2 \frac{2I-1}{E_{I\to I-2}}, \tag{4.4}$$

and the corresponding energy of the interband transition then given by

$$E_{I\to I-1} = \hbar^2 \frac{I}{\Im^{(1)}}. \tag{4.5}$$

This then gives energies assuming no relative energy shift between the signature partner bands. However, often one observes staggering between the bands which we take into account by considering a possible shift ΔE_0 between the bandheads of the signature partners, as illustrated in Figure 4.5 where intraband energies are known. This results in modified interband transition energies, shifted by $\pm\Delta E_0$ alternating between odd and even I_i where the peak N_o value obtained should relate to the ΔE_0 of the correct transition energies. This $\pm\Delta E_0$ may still be applied to all cases where a maximum N_o value should converge on the assumed known transition energies.

The errors in the observed $N_o \pm \sigma_o$ and expected $N_s \pm \sigma_s$ values, arise from the statistical uncertainties within the spectrum. The error in N_s derives from the combined error of the fitted set of intraband peaks, along with an uncertainty in the value of background added. This error in the added background is from the systematic uncertainty in the expected average background rate within the interband region and does not include the statistical uncertainty of the background observed. The error for N_o is simply an error in the counting statistics and is therefore given as

$$\sigma_o = \sqrt{N_o}, \tag{4.6}$$

which then includes the statistical error for the observed background. To test the consistency between the values $N_s \pm \sigma_s$ and $N_o \pm \sigma_o$, and hence the validity of the structural assignment s, the standard statistical quantity of the p-value is found. This gives the probability of obtaining the given results, or worse, assuming the null hypothesis, i.e. that the structural assignment s is correct. Our experimentally obtained difference value

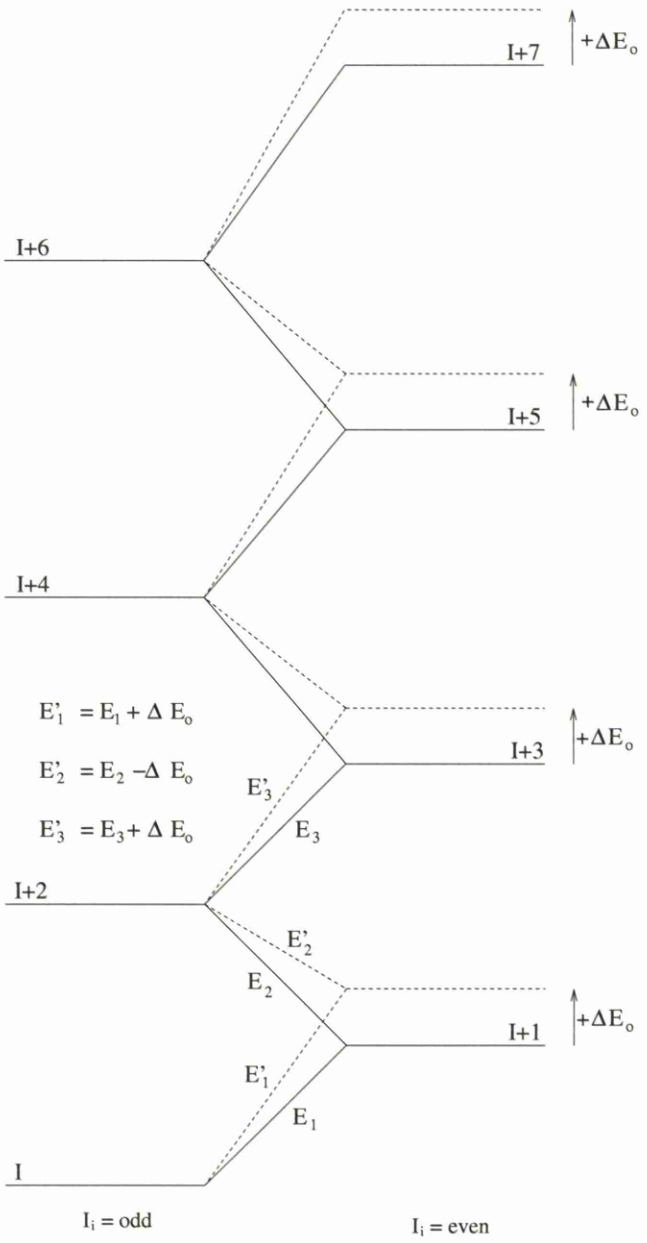

Figure 4.5: Rotational band level scheme of two signature partners with set intraband transition energies and interband energies varying with relative band shift energy ΔE_0.

$$D_e = N_s - N_o \tag{4.7}$$

is found and the null hypothesis that the mean of the distribution of difference values is taken as $\bar{D} = 0$. All $N \pm \sigma$ values are assumed reasonably large enough to be treated using Gaussian statistics, so by applying standard normal Gaussian distribution statistics, a two tailed probability of the difference being greater than or equal to the $|D_e|$ obtained, gives the p-value as

$$p = P(\mid D \mid \geq \mid D_e \mid) = 2\left\{1 - \Phi\left(\frac{\mid D_e \mid}{(\sigma_s^2 + N_o)^{\frac{1}{2}}}\right)\right\}. \tag{4.8}$$

Here Φ gives the cumulative distribution function of a standard normal distribution where the combined uncertainty is given by $({\sigma^2}_s + N_o)^{1/2}$ which is the standard deviation of the observed difference values D. This is used to normalise the function to one with a standard deviation of 1. The p-values found between N_o and two N_s values are illustrated in Figure 4.6 where the p-value found, relates to both N_{s1} and N_{s2} values shown. An unreasonably low result, i.e. $p \leq 0.01$, would indicate that the assumed structure s is not valid, as one would expect statistically to see these results less than one out of a hundred times, if it were the case. It should be noted that the p-value obtained from Equation 4.8 may produce a value close to 1 if $N_s \simeq N_o$ even if large statistical errors are present. These probabilities must therefore be considered in conjunction with results from other assumed structures in order to be fully interpreted.

The present method has been applied to the schematic simulations in Figure 4.1 for high and low statistics. Energies and intensities of five intraband γ-ray peaks with $I_i = 10$ to 14 were used. Estimates of the background in the interband region were found to be 41.1±0.7 counts/keV for (a) and 0.73±0.08 counts/keV for (b). Figure 4.7 compares the values of N_o for a varying ΔE_0 of ± 4 keV with N_{s1} ($g_K = +0.2$, green) and N_{s2} ($g_K = 0.0$, red) for high (a) and low (b) statistics, p-values for $\Delta E_0 = 0$ keV (as used in the simulation) are also given in Table 4.1. Results consistent with the $g_K = +0.2$ (s_1) value used in the simulations are shown in all cases.

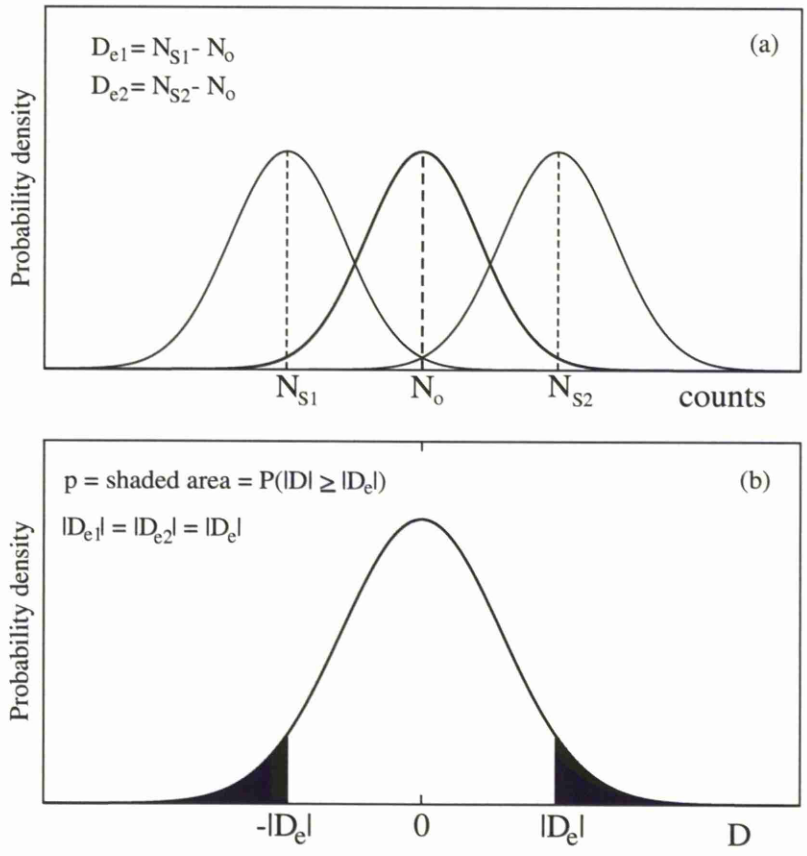

Figure 4.6: (a) Representation of observed count, $N_o \pm \sigma_o$ with expected counts $N_s \pm \sigma_s$ for two possible structures s_1 and s_2. (b) Probability distribution of expected difference D between N_s and N_o assuming the null hypothesis giving p as the shaded area applying to both D_{e1} and D_{e2}.

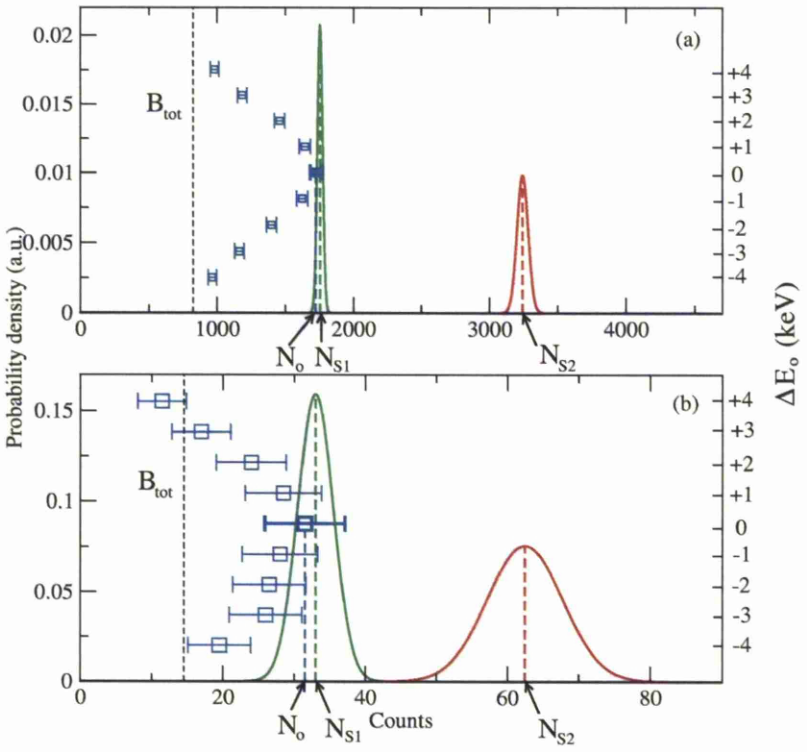

Figure 4.7: Cumulative γ-ray branching ratios method applied to schematic simulated spectra from a hypothetical isomeric state with (a) high and (b) low statistics. Expected intensity N_s found for structures s_1 ($g_K = +0.2$) and s_2 ($g_K = 0.0$) and observed intensity N_o shown for relative band shift energy $\Delta E_0 = \pm$ 4 keV. Error in values represented by width of distribution for N_s values and error bars for N_o values. Total expected background is shown as B_{tot}.

Table 4.1: p-values using cumulative γ-ray branching ratios method for high and low statistics schematic spectra shown for $\Delta E_0 = 0$ keV.

structure	$\lvert D_e \rvert$	$(\sigma_s{}^2+N_o)^{1/2}$	p
high statistics			
s_1	31.73	45.81	0.49
s_2	1520.71	58.09	<0.01
low statistics			
s_1	1.51	6.15	0.81
s_2	30.99	7.71	<0.01

s_1 ($g_K = +0.2$)
s_2 ($g_K = 0.0$)

As this method allows us to use interband γ-ray counts that are not abundant enough to distinguish as peaks, as well as combining the statistics from multiple γ-ray pair ratios, it helps to fully utilise the data in assigning a single particle state.

4.2.1 ^{250}Fm

This method of analysis was carried out using a spectrum of the rotational band built on an 8^- isomeric state in ^{250}Fm shown in Figure 4.8 and taken from reference [41], fitted intensities, energies and transition assignments are shown in Table 4.2. The seven intraband γ-ray peaks used in the analysis with $I_i = 13 \rightarrow 19$ are highlighted as (**) in the spectrum along with the interband energy range. Theoretical R values were obtained using $Q_0 = 12.60$ eb and an estimate of $g_R = 0.400$. Values of g_R factors below the estimate have been seen in other regions (see Section 2.6) so a quenching will also be added giving $g_R = q{\cdot}(Z/A)$ and a value of $q = 0.7$ taken. Two quasi-particle states of $8^-\{\frac{7}{2}^+[624]_\nu \otimes \frac{9}{2}^-[734]_\nu\}$ (s_1) and $8^-\{\frac{7}{2}^-[514]_\pi \otimes \frac{9}{2}^+[624]_\pi\}$ (s_2)

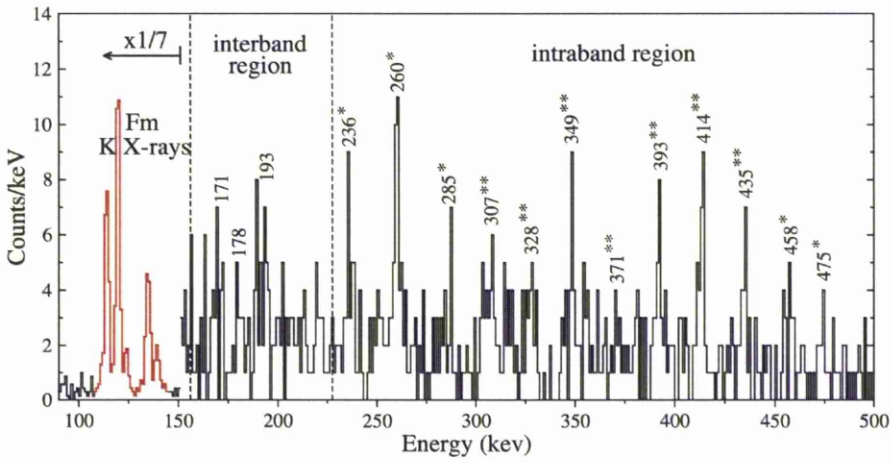

Figure 4.8: Spectrum of γ rays from rotational band above an 8^- isomeric state in ^{250}Fm. The inter and intraband transition energy regions are highlighted along with the range over which X-ray region intensities were taken (red). Peak intensities used in both methods labelled (**) and those used only in X-ray region intensities labelled (*). Spectrum taken from [41].

Table 4.2: Transitions and energies of observed γ rays in the rotational band above an 8^- K-isomeric state in ^{250}Fm. Fitted γ-ray intensities, $\mathcal{I}$, and those corrected for detector efficiency and scaled to 260 keV transition, $\mathcal{I}^*$, are shown. Spectra taken from [41].

$I_i \rightarrow I_f$	$E\gamma$(keV)	$\mathcal{I}$(counts)	$\mathcal{I}^*$(a.u.)
$10^- \rightarrow 8^-$	236	14.7(47)	47(15)
$11^- \rightarrow 9^-$	260	30.8(62)	100(20)
$12^- \rightarrow 10^-$	285	6.8(34)	22(11)
$13^- \rightarrow 11^-$	307	15.2(46)	51(15)
$14^- \rightarrow 12^-$	328	14.4(44)	49(15)
$15^- \rightarrow 13^-$	349	6.5(42)	22(14)
$16^- \rightarrow 14^-$	371	3.7(35)	13(12)
$17^- \rightarrow 15^-$	393	16.2(49)	58(17)
$18^- \rightarrow 16^-$	414	20.7(55)	75(20)
$19^- \rightarrow 17^-$	435	8.0(43)	29(16)
$20^- \rightarrow 18^-$	458	6.6(41)	25(15)
$21^- \rightarrow 19^-$	475	3.7(32)	14(12)
$14^- \rightarrow 13^-$	171	9.2(67)	32(23)
$15^- \rightarrow 14^-$	178	9.9(40)	33(13)
$16^- \rightarrow 15^-$	193	12.1(45)	40(15)

Table 4.3: Selected p-values for ^{250}Fm 8^- isomer results using cumulative γ-ray branching ratios method. The values for $\Delta E_0 = +2$ keV found are highlighted with analysis performed using $q = 1$ and 0.7.

ΔE_0(keV)	$\lvert D_e \rvert$	$(\sigma_s{}^2+N_o)^{1/2}$	p	ΔE_0(keV)	$\lvert D_e \rvert$	$(\sigma_s{}^2+N_o)^{1/2}$	p
s_1 ($q = 1$)				s_2 ($q = 1$)			
-4	27.29	10.41	0.01	-4	70.52	15.13	<0.01
-2	14.54	11.01	0.19	-2	57.77	15.54	<0.01
0	7.04	11.34	0.53	0	50.27	15.78	<0.01
+2	1.54	11.59	0.89	+2	44.77	15.96	<0.01
+4	19.58	10.78	0.07	+4	62.81	15.38	<0.01
s_1 ($q = 0.7$)				s_2 ($q = 0.7$)			
-4	7.88	8.93	0.38	-4	106.05	19.67	<0.01
-2	4.87	9.62	0.61	-2	93.3	19.99	<0.01
0	12.37	10.00	0.22	0	85.8	20.17	<0.01
+2	17.87	10.27	0.08	+2	80.3	20.31	<0.01
+4	0.17	9.35	0.99	+4	98.34	19.86	<0.01

$$s_1 = 8^-\{\tfrac{7}{2}^+[624]_\nu \otimes \tfrac{9}{2}^-[734]_\nu\}\ (g_K = \text{-}0.03)$$
$$s_2 = 8^-\{\tfrac{7}{2}^-[514]_\pi \otimes \tfrac{9}{2}^+[624]_\pi\}\ (g_K = +1.02)$$

are predicted with correct spin and parity at low energies [42] and were therefore taken as possible structural assignments of the isomeric state giving g_K factors of -0.03 and +1.02 respectively. N_o values were obtained using 4 keV energy ranges and a relative band shift energy ΔE_0 of $\pm$4 keV was used from the interband energies obtained using Equations 4.4 and 4.5. The results of the $N_o \pm \sigma_o$ values, compared with the expected values for the two configurations $N_{s1} \pm \sigma_{s1}$ and $N_{s2} \pm \sigma_{s2}$, are shown in Figure 4.9 with the p-values given in Table 4.3 with correct ΔE_0 indicated in both. A clear indication for the band shift energy ΔE_0 is obtained as a maximum

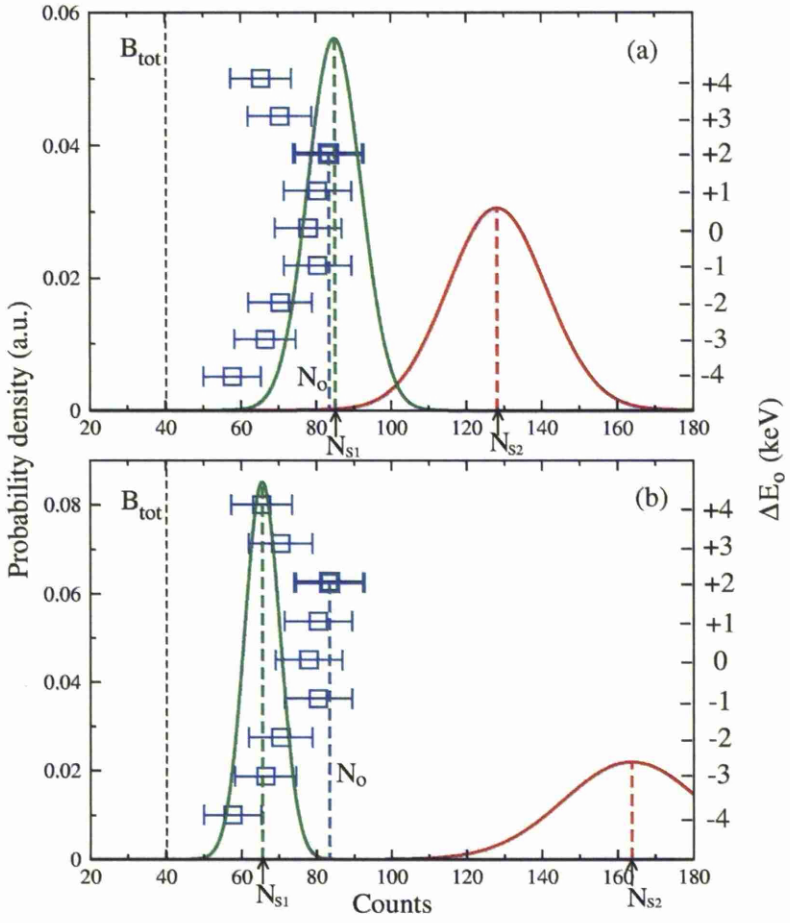

Figure 4.9: Expected total counts $N_s \pm \sigma_s$ found for two structures s_1(green) and s_2(red) using γ-ray spectrum of rotational band above an 8^- isomer in ^{250}Fm applying cumulative γ-ray branching ratios method. Observed counts $N_o \pm \sigma_o$ (blue) highlighted for $\Delta E_0 = +2$ keV. Performed without (a) and with quenching of $q = 0.7$(b), also shown is the total background B_{tot} added for N_s values.

of the N_o value, in this case around +2 keV. As expected this value of +2 keV is in line with the three fitted energies for intraband γ-ray transitions. The results conclusively assign the isomer to the state $8^-\{\frac{7}{2}^+[624]_\nu \otimes \frac{9}{2}^-[734]_\nu\}$ as the p-values between expected and observed counts are <0.01 assuming the s_2 structure for both unquenched and quenched g_R. High p-values are also seen for the s_1 state with q from 0.7 to 1 indicating consistency with the structure; this is in line with results found in [21] and [41]. It should be noted that the N_o values do not fall to the B_{tot} level when moving away from the $\Delta E_0 = +2$ keV value. This is thought partly to be due to counts from the interband transitions existing between the central peak energies and the closeness of the interband peaks accentuating this. It is also possible that the increase in observed intensities is contributed to by transitions from other populated bands not considered or an underestimation of the background rate in the interband region.

4.2.2 ^{254}No

The γ-ray spectrum of the rotational band above an isomeric state in ^{254}No taken from the reference [43] is shown in Figure 4.10 along with two published interpretations of the level scheme (a)[43] and (b)[44]. In this case as opposed to having just one set of clear peaks, there are three pairs of peaks that may be cleanly fitted. This example provides the opportunity to apply the cumulative γ-ray branching ratios method in a modified form, using fitted intensities for both intraband and interband γ-ray transitions. Again, the fitted intensities of the intraband peaks highlighted with $I_i = 13 \rightarrow 15$ are used and assuming three possible configurations using the $K^\pi = 8^-$ interpretation (a), and one for the $K^\pi = 10^+$ interpretation (b), four possible N_s values are obtained. The N_o value however, is taken as the combined intensities of the three fitted interband peaks highlighted: (inter and intraband transitions may be used either for N_s or N_o with no effect on p-values when using fitted intensities). As fitted peaks are used, the B_{tot} and f terms in Equation 4.3 are not needed, so that now

$$N_s = \sum_{I_i} (\mathcal{I}(\Delta I = 2)_{I_i} \cdot R_{I_i} \cdot \varepsilon(E_{I_i})) \,. \tag{4.9}$$

Also no ΔE_0 needs to be applied in obtaining values of N_o. The analysis was performed using values of $Q_0 = 13.28$ eb and $g_R = 0.402$ with both unquenched and quenched ($q = 0.7$) values. The possible configurations and g_K factors used for the state, along with results, are shown in Table 4.4 and Figure 4.11.

Due to the parabolic relationship $R(g_K) \propto (g_K - g_R)^2$, then two g_K factors relate to the same R values. In this case this leads to the N_s values for the s_2 and s_3 configurations to be very similar and also cross over when changing q from 1 to 0.7. The uncertainty of q would therefore make it difficult to identify the structure using this method even with increased statistics. This analysis cannot therefore rule out an s_3 two proton or s_2 two neutron quasi-particle structure for the isomeric state. The s_1 configuration may be dismissed by the results which also show that the s_4 is unlikely unless a relatively large quenching factor is taken. The suggested level scheme in [44] claims that the deduced g_K factor is consistent with the tentative 10^+ structure, our analysis shows that it is unlikely that the 10^+ configuration is a pure one, should the level scheme be borne out by further experiments.

4.3 Method: X-ray region intensities

A further method which may be used to assign isomeric structures from rotational band γ-ray spectra above them, again utilises combined transition peak intensities. In this case, however, it is the expected number of counts within the energy range of the K X rays that is found assuming possible structural assignments to provide N_{xs} values. An observed N_{xo} value, independent from the N_o value given by the previous method, is then found as the total counts across the K X-ray range within the spectrum.

Populated rotational bands will emit both γ rays and conversion electrons when decaying; the latter of which may lead to the emission of an X ray from atomic electron

Table 4.4: p-values for ^{254}No isomer results using the cumulating γ-ray branching ratios method, performed using $q = 1$ and 0.7.

structure	$\lvert D_e \rvert$	$(\sigma_s{}^2+N_o)^{1/2}$	p	structure	$\lvert D_e \rvert$	$(\sigma_s{}^2+N_o)^{1/2}$	p
$(q = 1)$				$(q = 0.7)$			
s_1	78.80	17.04	<0.01	s_1	100.99	14.76	<0.01
s_2	6.01	23.52	0.83	s_2	44.15	22.02	0.05
s_3	30.22	24.31	0.21	s_3	10.81	31.57	0.73
s_4	136.56	57.19	0.02	s_4	49.69	39.81	0.21

$s_1 = 8^-\{\frac{7}{2}^+[624]_\nu \otimes \frac{9}{2}^-[734]_\nu\}$ (g_K = -0.02)
$s_2 = 8^-\{\frac{7}{2}^+[613]_\nu \otimes \frac{9}{2}^-[734]_\nu\}$ (g_K = -0.28)
$s_3 = 8^-\{\frac{7}{2}^-[514]_\pi \otimes \frac{9}{2}^+[624]_\pi\}$ (g_K = +1.01)
$s_4 = 10^+\{\frac{11}{2}^-[725]_\nu \otimes \frac{9}{2}^-[734]_\nu\}$ (g_K = -0.23)

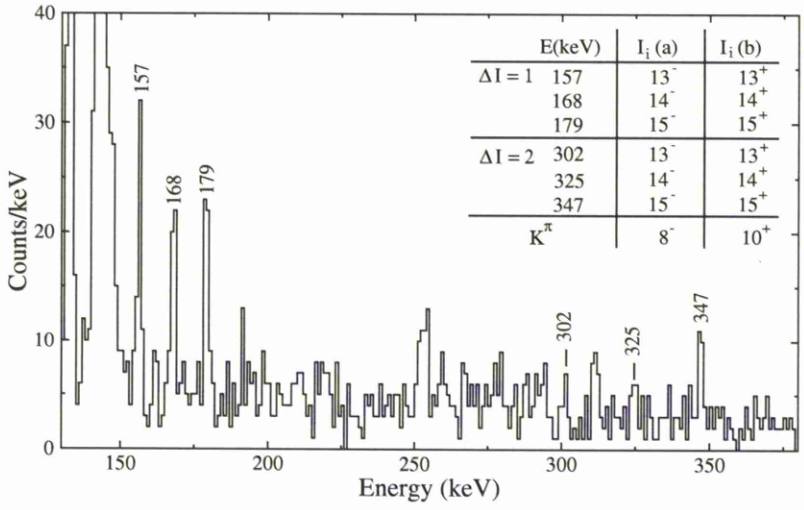

Figure 4.10: Spectrum of γ-rays from rotational band built above an isomer in ^{254}No taken from [43]. Two different K^{π} assignments to the isomer are given from different interpretations (a) and (b), and fitted peaks used in analysis are highlighted.

reordering. If the intensities of γ-ray transitions of given mulitipolarity and spin change are known from within the band, then by using their conversion coefficients, (see Section 2.7.2), the intensity of conversion electrons ejected from the K shell may be found. Using then the probabilities of emission for each of the prominent K X rays from a K shell electron vacancy, the expected K X-ray intensity in the spectrum may be found. The γ-ray intensities and conversion coefficients will be labelled accordingly in this section;

$$\mathcal{I}_{\lambda L} = \mathcal{I}_{\gamma}(\sigma\lambda, \Delta I = L), \tag{4.10}$$

$$\alpha_{\lambda L}^{tot,K} = \alpha^{tot,K}(\sigma\lambda, \Delta I = L), \tag{4.11}$$

giving conversion coefficients for total converted transitions, α^{tot}, or only those from the K shell, α^{K}. As an interband γ-ray transition is mixed between E2 and M1 multipoles, which give different conversion coefficients, it is necessary to use the mixing ratio δ given in Equation 4.2. The mixing ratios, along with R values, are a function

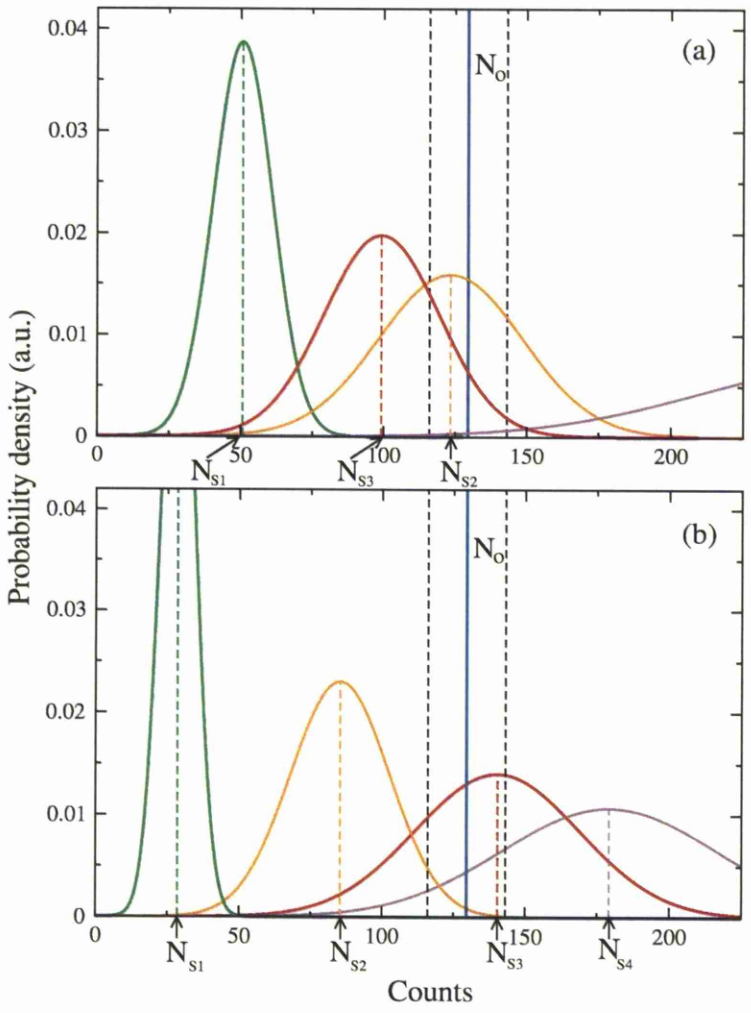

Figure 4.11: Expected total counts $N_s \pm \sigma_s$ found for structures s_1(green), s_2(orange), s_3(red) and s_4(brown) from γ-ray spectrum of rotational band above isomer in ^{254}No using the cumulating γ-ray branching ratios method. Compared with total fitted observed counts $N_o \pm \sigma_o$ (blue), performed without(a) and with quenching of $q = 0.7$(b).

of the g_K factor and hence the underlying structure. By using a known set of $\mathcal{I}_{22}$ intraband intensities, one may now find the expected $\mathcal{I}_{21}$ and $\mathcal{I}_{11}$ interband intensities from a given level I_i for an assumed structure s as

$$\mathcal{I}_{21I_i} = \frac{R_{I_i} \cdot \mathcal{I}_{22I_i}}{(\frac{1}{\delta_{I_i}} + 1)}, \mathcal{I}_{11I_i} = \frac{R_{I_i} \cdot \mathcal{I}_{22I_i}}{(\delta_{I_i} + 1)} \tag{4.12}$$

(these are not efficiency corrected at this stage). Using the $\mathcal{I}_{21}$, $\mathcal{I}_{11}$ and $\mathcal{I}_{22}$ γ-ray intensities, the intensity of converted transitions from the K atomic shell is found using the K conversion coefficients. The probability of one of the possible K X rays, labelled X, being subsequently emitted as a result of this K shell vaccancy, is given by the corresponding w_X factor [36], so that the total K X-ray intensity expected may be given as

$$t = \sum_{I_i} \sum_{X} w_X (\mathcal{I}_{21I_i} \alpha^K_{21I_i} + \mathcal{I}_{11I_i} \alpha^K_{11I_i} + \mathcal{I}_{22I_i} \alpha^K_{22I_i}) \cdot \epsilon(E_{XI_i}) \tag{4.13}$$

summed over all K X rays and all I_i levels occupied in the rotational band. The atomic shells are assumed to be full when transitions occur, meaning that all prominent K X-ray emissions are considered. The efficiency ratio $\epsilon(E_{XI_i})$ is found between efficiencies at energies $E(\text{X ray})_X / E(\Delta I = 2)_{I_i}$, correcting for efficiency discrepancy between the intraband and X-ray intensities. Our observed N_{xo} value is taken as the total counts in an energy range incorporating all K X rays considered with error given as $\sigma_{xo} = \sqrt{N_{xo}}$. The N_{xs} value must also therefore, include expected γ-ray intensities from interband transitions within this range and are given by the corresponding values obtained in Equation 4.12. The ratio between detector efficiencies at $E_\gamma(\Delta I = 1)_{I_i} / E_\gamma(\Delta I = 2)_{I_i}$ is also needed and is given as $\epsilon(E_{I_i})$. A background estimate B_{tot} is also added to give the total expected value

$$N_{xs} = t + B_{tot} + \sum_{I_i} (\mathcal{I}_{21I_i} + \mathcal{I}_{11I_i}) \cdot \epsilon(E_{I_i}), \tag{4.14}$$

summed over all I_i levels with interband transition energies within the K X-ray range. The error σ_{xs} is determined by the uncertainty in the fitted set of $\mathcal{I}_{22}$ values and the

systematic uncertainty of the background estimate.

A problem arises in that $\mathcal{I}_{21}$ and $\mathcal{I}_{11}$ intensities may not be found from the $I_i = K{+}1$ level due to no intraband transition. Here the original population of the level $\mathcal{T}$ is estimated to be equal to that of the level above i.e. $\mathcal{T}_{I_i=K+1} = \mathcal{T}_{I_i=K+2}$. This is found by initially finding the total number of transitions from a level given by

$$\mathcal{T}^*_{I_i} = \mathcal{I}_{21I_i}(\alpha^{tot}_{21I_i} + 1) + \mathcal{I}_{11I_i}(\alpha^{tot}_{11I_i} + 1) + \mathcal{I}_{22I_i}(\alpha^{tot}_{22I_i} + 1) \tag{4.15}$$

and then getting the initial population by subtracting the transitions that feed the level from

$$\mathcal{T}_{I_i} = \mathcal{T}^*_{I_i} - (\mathcal{I}_{21I_i+1}(\alpha^{tot}_{21I_i+1} + 1) + \mathcal{I}_{11I_i+1}(\alpha^{tot}_{11I_i+1} + 1) + \mathcal{I}_{22I_i+2}(\alpha^{tot}_{22I_i+2} + 1)). \tag{4.16}$$

Now we find $\mathcal{T}^*_{I_i=K+1}$ as $\mathcal{T}_{I_i=K+2}$ for its initial population, plus the transition intensities fed to it from the levels above. All intensities used are efficiency corrected in relation to their energies.

A limiting factor of this method, is that X-ray emission may occur for any converted transition within a nucleus or atomic electron de-excitation. We have assumed only rotational band transitions here, but the spectrum may contain excess X rays from transitions not considered. For this reason the N_{xo} value represents an upper limit when compared with N_{xs}. The p-values are now given as a standard normal Gaussian distribution single tailed probability

$$p = P(D \geq D_e) = 1 - \Phi\left(\frac{D_e}{(\sigma^2_{xs} + N_{xo})^{\frac{1}{2}}}\right) \tag{4.17}$$

where the sign of the D value is now relevant. Again Φ gives the cumulative distribution function of a standard normal distribution which is normalised by the combined uncertainty given as $(\sigma^2{}_{xs} + N_{xo})^{1/2}$. Finding these p-values is illustrated in Figure 4.12 using the D_e values shown in Figure 4.6(a).

A p-value of 0.5 will be given if $N_{xo} = N_{xs}$ with the value diminishing as D_e increases positively, relating to a greater expected N_{xs} than observed upper limit

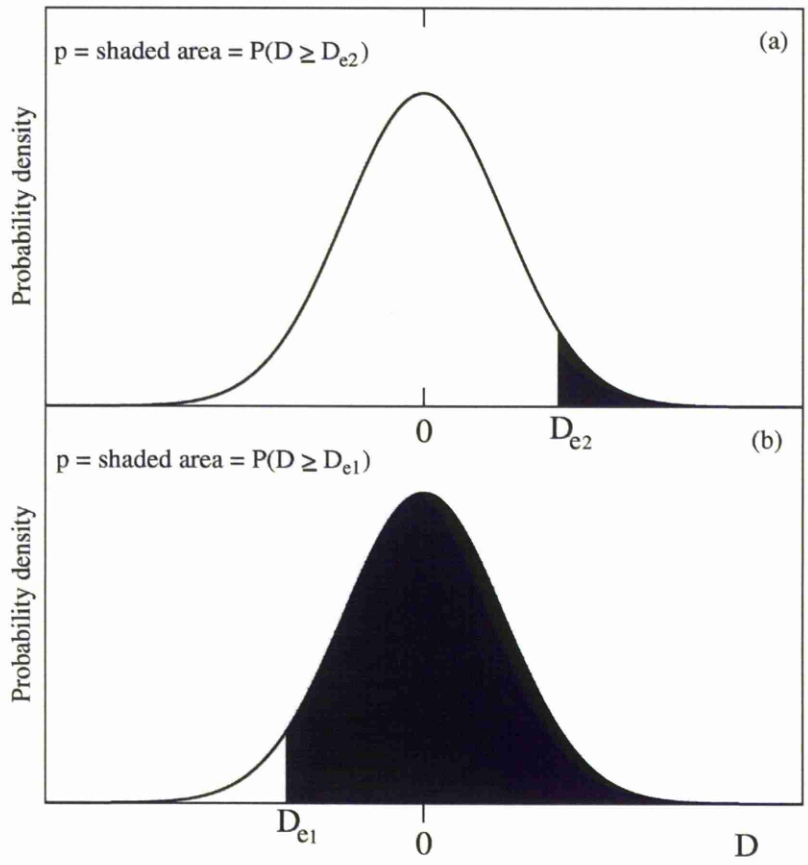

Figure 4.12: Represents single tailed normal Gaussian p-values found for X-ray region intensities results D_{e2}(a) and D_{e1}(b) from Figure 4.6.

N_{xo}. Conversely, p will increase as D_e increases negatively, relating to an increasing consistency between the observed upper limit, and N_{xs} for a structure. Using N_{xo} as an upper limit clearly means that high p-values can only be taken as representing consistency with a structural assignment without providing direct evidence, whereas low values may still be used to dismiss structures.

This analysis was carried out on the high and low statistic simulated schematic spectra in Figure 4.1. Values for N_{xs} were obtained using all intraband peaks with $I_i = 8$ to 15 and N_{xo} was taken between 102 and 145 keV (X-ray emissions and conversion coefficients based on fermium were used in the simulation). This range was set to encorporate the ten most prominent K X rays listed in reference [36] and interband transitions with $I_i = 7 \rightarrow 9$. Structures s_1 (green) with $g_k = +0.2$ (in which the simulation was based) and s_2 (red) with $g_k = 0.0$ were taken. Analysis was performed taking N_{xo} values obtained not as upper limits as obviously no excess X rays are present in the schematic simulation. Figure 4.13 compares the values of N_{xs} with N_{xo} (blue) and p-values found, using double tailed probabilities, are given in Table 4.5. These results again reproduce the $g_K = +0.2$ value used in the simulation.

4.3.1 ^{250}Fm

This method has been applied to the rotational band spectrum above the 8^- isomer in ^{250}Fm with the set of intraband γ-ray peaks used and K X-ray energy range from 108 keV$\rightarrow$145 keV highlighted in Figure 4.8. This was set to incorporate the ten most prominent K X rays listed in reference [36] and interband transitions with $I_i = 9 \rightarrow 11$. As no more peaks at higher energies are visible, the rotational band is assumed to significantly populate up to level $I^\pi = 21^-$. The structures s_1 and s_2 used were the same as in the previous section and the results are shown in Figure 4.14, with N_{xo} shown as a dashed black line and $1\sigma_{xo}$ upper error bar as a blue line (acting as an upper limit). The p-values are given in Table 4.6.

It should be noted that as N_{xo} is an upper limit, the method is still applicable to cases where not all intensities from I_i levels populated, are known. However, it is of

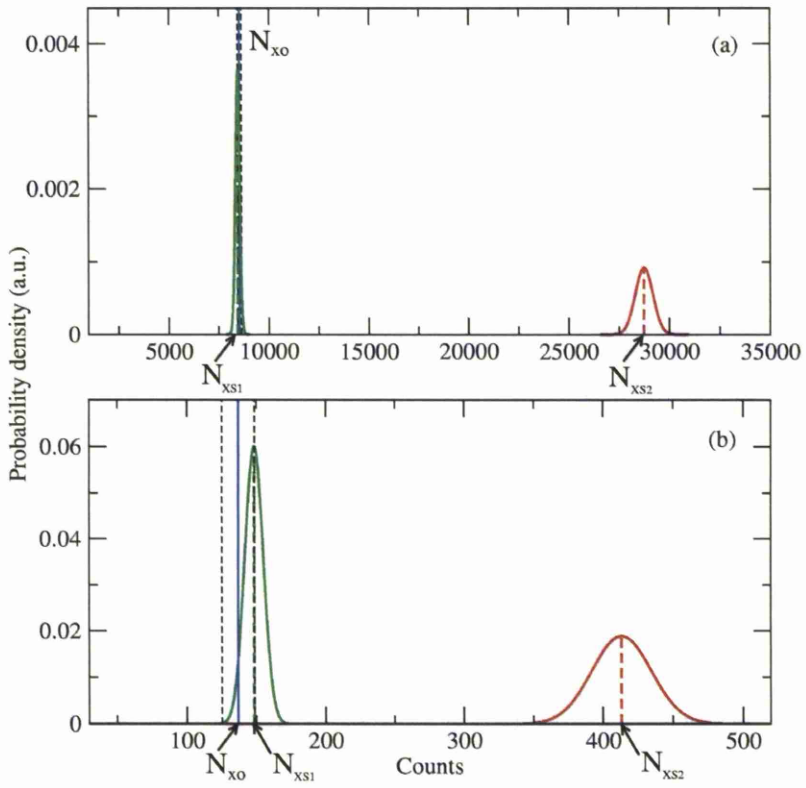

Figure 4.13: X-ray region intensities method applied to schematic simulated spectrum from a hypothetical isomeric state with (a) high and (b) low statistics. Expected intensity N_{xs} found for structures s_1 ($g_K = +0.2$) and s_2 ($g_K = 0.0$) with observed intensity given as N_{xo}.

Table 4.5: p-values from X-ray region intensities method found using schematic spectra with double tailed probabilities.

structure	$\lvert D_e \rvert$	$(\sigma_{xs}{}^2+N_{xo})^{1/2}$	p
high statistics			
s_1	100.97	144.06	0.48
s_2	20218.48	444.69	<0.01
low statistics			
s_1	11.46	13.46	0.39
s_2	276.31	24.20	<0.01

s_1 ($g_K = +0.2$)
s_2 ($g_K = 0.0$)

little use when applied to the ^{254}No spectrum in Figure 4.10, as γ-ray intensities are not known from most of the levels populated in the transitions above the isomer.

The results for ^{250}Fm again indicate that the $8^-\{\frac{7}{2}^-[514]_\pi \otimes \frac{9}{2}^+[624]_\pi\}$ (s_2) state is not responsible for the isomer with negligible p-values for both values of q used. They are also consistent with the $8^-\{\frac{7}{2}^+[624]_\nu \otimes \frac{9}{2}^-[734]_\nu\}$ (s_1) state, but this cannot itself be taken as direct evidence for the configuration.

This method uses a greater number of peak intensities in finding N_{xs} and a larger number of counts for N_{xo} than the method in Section 4.2 which gives a reduced final error factor $(\sigma_{xs}{}^2+N_{xo})^{1/2}$. It also provides an independent value of N_{xo} from the cumulative γ-ray branching ratios method.

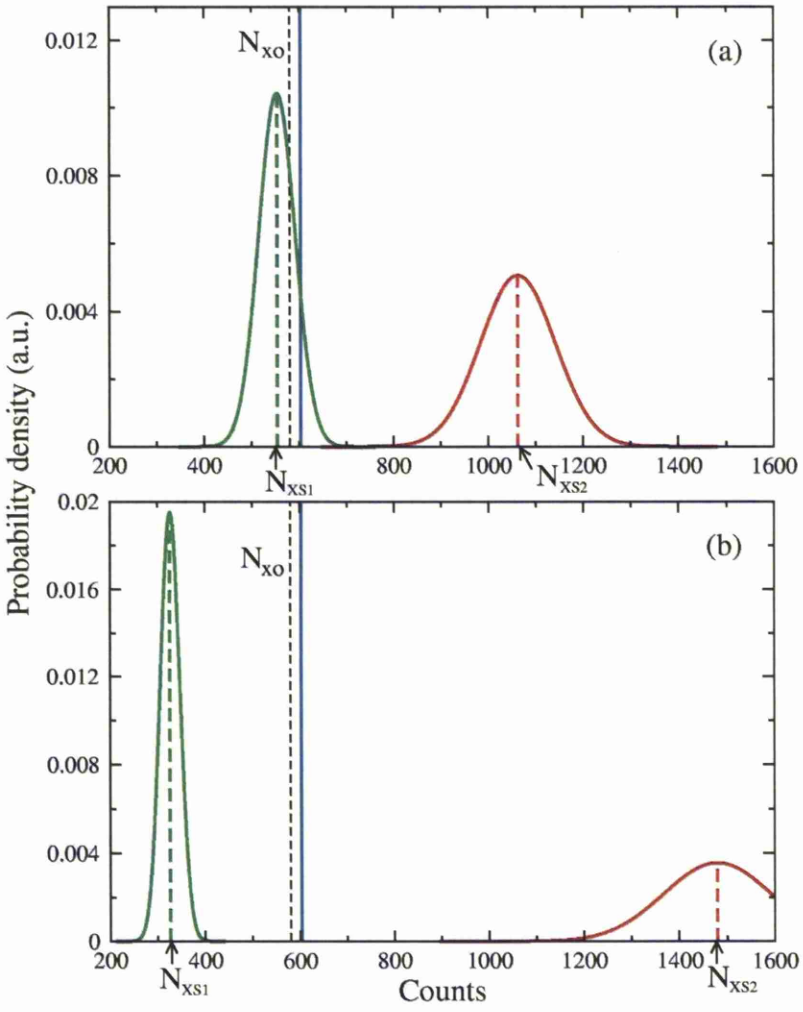

Figure 4.14: Expected total counts $N_{xs} \pm \sigma_{xs}$ found for structures s_1(green) and s_2(red) applied to γ-ray spectrum of rotational band above 8^- isomer in ^{250}Fm using X-ray region intensities method. Compared with observed counts $N_{xo} \pm \sigma_{xo}$ (black dashed) and $1\sigma_{xo}$ upper limit (blue) performed with $q = 1$(a) and 0.7(b).

Table 4.6: p-values from expected X-ray region intensities method found using spectrum from the 8^- isomer in ^{250}Fm. Performed with $q = 1$ and 0.7.

structure	D_e	$(\sigma_{xs}{}^2+N_{xo})^{1/2}$	p
$q = 1$			
s_1	-26.02	45.30	0.72
s_2	483.52	82.14	<0.01
$q = 0.7$			
s_1	-252.96	31.61	~1
s_2	900.25	114.84	<0.01

$s_1 = 8^-\{\frac{7}{2}^+[624]_\nu \otimes \frac{9}{2}^-[734]_\nu\}$ (g_K = -0.03)
$s_2 = 8^-\{\frac{7}{2}^-[514]_\pi \otimes \frac{9}{2}^+[624]_\pi\}$ (g_K = +1.02)

Chapter 5

Results

The nucleus ^{252}No has been studied in various previous experiments leading to well established values for many of its properties. Its half-life was first found to be 2.3(3) s [45] and further results have yielded values of 2.30(22) s [46] and 2.4(3) s [47]. Ground state decays proceed via α emission, with E_α = 8415(6) keV with $\mathcal{I}_\alpha$ = 75% and E_α = 8372(8) keV with $\mathcal{I}_\alpha$ = 25% [48], spontaneous fission and electron capture. The branching fraction for the electron capture process, has been found as b_{EC} = 0.8% [49] with the b_{SF} given as various values ranging from 21.6(42)% [50] to 32.2(5)% [39]. The ground state level scheme has been established by Herzberg [47] up to $I^\pi = 20^+$.

A K-isomeric state with $K^\pi = 8^-$, was first studied by Sulignano [24] and was found to have an excitation energy of 1254 keV and a half-life of 110(10)ms; these results were reproduced by Robinson [20]. The results from Sulignano were used to find the reduced hindrance factors (See Section 2.5) for transitions from this 8^- K-isomer to both the ground state band and a $K = 2^-$ side band. Values of f_ν(E1, ΔK = 8) = 178 and f_ν(M1, ΔK = 6) = 218 [51] indicate the high purity of the state with little mixing of either the ground state or 2^- bands. This state was assigned the configuration $8^-\{\frac{7}{2}^+[624]_\nu \otimes \frac{9}{2}^-[734]_\nu\}$ by comparison between the assigned spin, parity and excitation energy of the observed state with those of theoretically predicted two quasi-particle excitations in the nucleus [52]. A summary of previous results from

Table 5.1: Summary of results obtained from previous investigations of ^{252}No.

$T_{1/2}$ (s):	2.3(3) [45], 2.30(22) [46], 2.4(3) [47]			
E_α (keV):	8415(6) (I_α = 75%) and 8372(8) (I_α = 25%) [48]			
b_{SF} (%):	23.1(6) [53], 32(3) [54], 32.2(5) [39], 26.9(19) [46], 21.6(42) [50]			
b_{ec} (%):	0.8 [49]			
Band spin	Excitation energy	Measured up to I^π	Half-life	reference
GS	0 keV	20^+	-	[47]
2^-	929 keV	7^-	prompt	[24]
8^-	1254 keV	8^-	110(10) ms	[24]

the study of ^{252}No is given in Table 5.1.

Using the tagging methods described in Section 3.3, a total number of 9,670 evaporations were recoil-decay tagged (RDT), of which 2,127 were R-ce-DT and identified in the 8^- isomeric state. Without the requirement of a subsequent ground state decay, the number of RT evaporations were 35,359 with 3,172 of those R-ce-T in the isomeric state (full details of tagged events are given in Table 5.2). Analysis yielded consistent values for all quantities previously mentioned and in-beam spectra of γ-ray transitions in rotational bands built on the 8^- isomer, were obtained for the first time. This was used to give direct evidence that the state has structural assignment $8^-\{\frac{7}{2}^+[624]_\nu \otimes \frac{9}{2}^-[734]_\nu\}$ confirming the previous conjecture [24]. The level scheme of ^{252}No could therefore be extended and is given in Figure 5.1 highlighted in blue.

5.1 Focal plane decays

5.1.1 Half-lives

The half-life of a decaying state is measured using the experimental setup by identifying the desired recoils using recoil decay tagging methods. This allows for the time between the implantation in the DSSSD and subsequent decay of these recoils to be

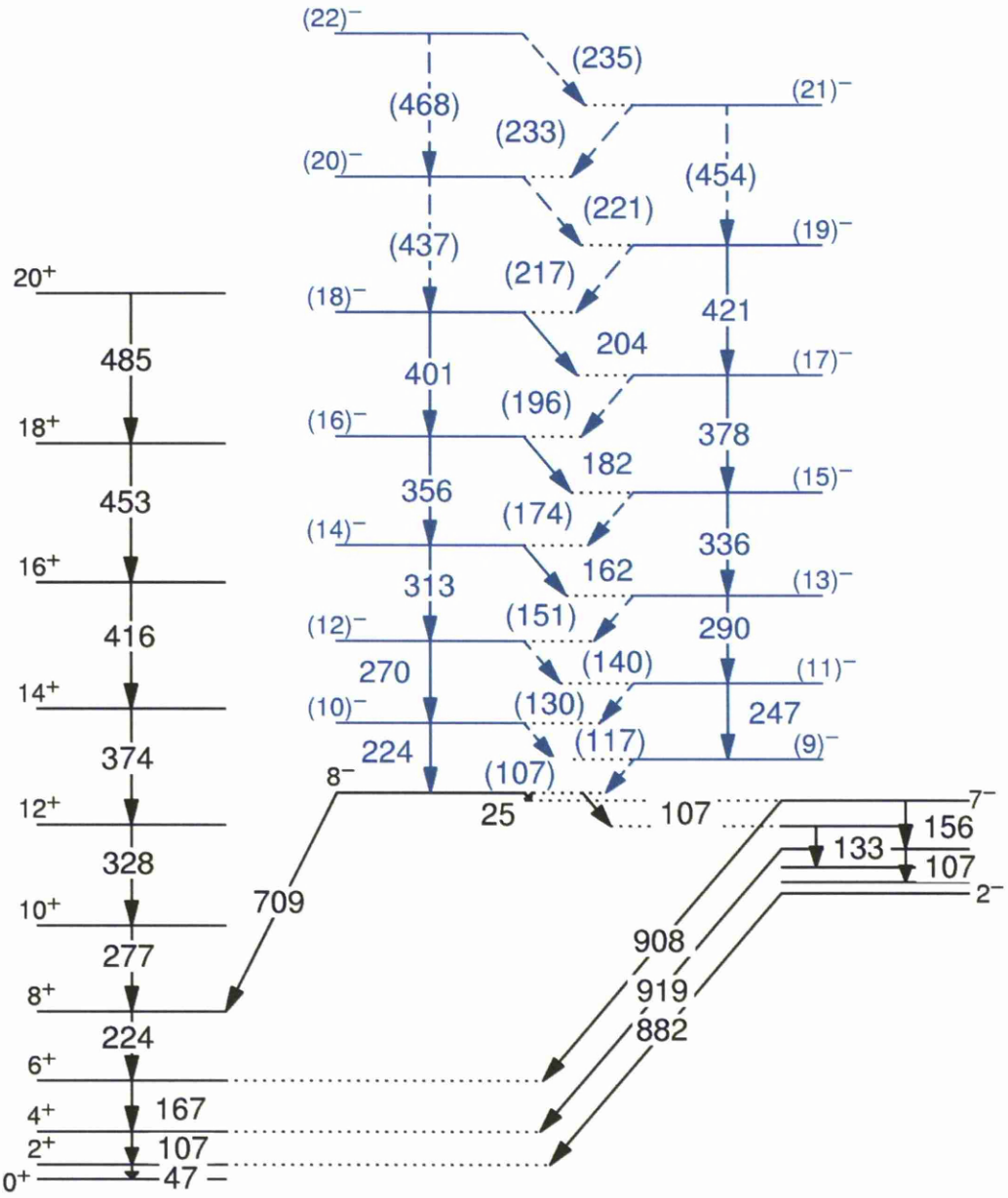

Figure 5.1: Level scheme of ^{252}No extended to include newly observed transitions above the 8^- isomeric state (highlighted in blue). Tentative transition and level spin assignments are shown in brackets.

plotted, giving their characteristic exponential decay. This is shown in Figure 5.2 where alpha and spontaneous fission events of ^{252}No tagged recoils have been subsequently tagged separately from their decay; the time after implantation of which has been plotted.

The ^{252}No recoils implant onto the focal plane with ~80% in their ground state and ~20% in the 8^- isomeric state which decays to the ground state (N.B. the intermediate 2^- state is not isomeric). The function giving the activity A of the ground state at time t, will then take the form

$$A_2(t) = N_{o1} \cdot \lambda_2 \cdot \frac{\lambda_1}{\lambda_2 - \lambda_1} \cdot (e^{-\lambda_1 t} - e^{-\lambda_2 t}) + N_{o2} \cdot \lambda_2 \cdot e^{-\lambda_2 t} \qquad (5.1)$$

where N_o and λ represent the number of nuclei implanted in a state at $t = 0$ and the decay constant, respectively. A quantity assigned to the isomeric state has subscript 1 with those of the ground state, 2. The second term on the right hand side concerns the decay of nuclei implanted in the ground state at $t = 0$ and the first term gives the ground state activity produced by nuclei which originally occupied the isomeric state at $t = 0$. The background, due to random misassignments, was not considered in the fit, as this was found to be negligable (detailed in Section 5.1.2).

To find the ground state half-life, the decay plot for RDT events was fitted to the form of Equation 5.1 and the λ_2 in the exponentially decaying terms were used giving $T_{1/2} = \ln 2/\lambda$. The errors for the points in the decay plot were given as $(\text{counts}+1)^{1/2}$ so as to not allow bins with zero counts to dominate the fit. The half-life found for combined alpha and spontaneous fission decaying ground state events was $T_{1/2} = 2.35(4)$ s, which is in good agreement with previous measurements. The two half-lives found for exclusively alpha or spontaneous fission decaying recoils were consistent at $T_{1/2} = 2.32(9)$ s and 2.26(5) s respectively, indicating that the method of using high energy overflow signal for spontaneous fission tagging is sound.

To find the isomeric half-life, the ^{252}No nuclei implanted in the 8^- isomeric state were identified from R-ce-DT events using only subsequent decay tags from the ^{252}No ground state (the reason for not including those events which were identified via a

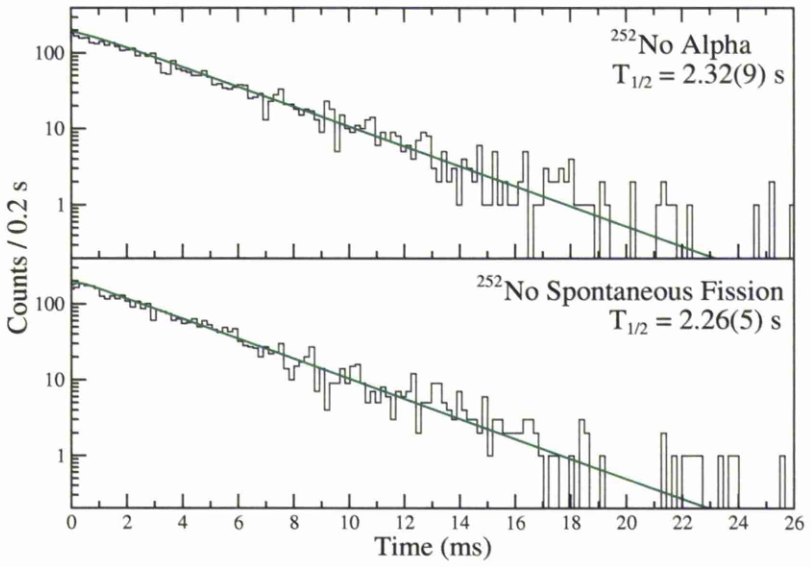

Figure 5.2: Time of ^{252}No decays after implantation via alpha (top panal) and spontaneous fission (bottom panel) ground state modes. Fitted functions to find half-lives also shown.

subsequent ^{248}Fm or ^{244}Cf alpha emission will be explained in detail in Section 5.1.3). The half-life of the state was found by fitting the decay curve shown in Figure 5.3 to the function

$$A_1(t) = N_{o1} \cdot \lambda_1 \cdot e^{-\lambda_1 t}. \tag{5.2}$$

Again a consideration of the random background was found not to be necessary. The $T_{1/2}$ was given as 99.9(31) ms and is in line with that previously found of 110(10) ms [24].

5.1.2 Branching fractions of ground state decays

In finding the branching fractions from the decaying ground state ^{252}No nuclei, we must estimate the random misassignment rate due to background in the DSSSD and

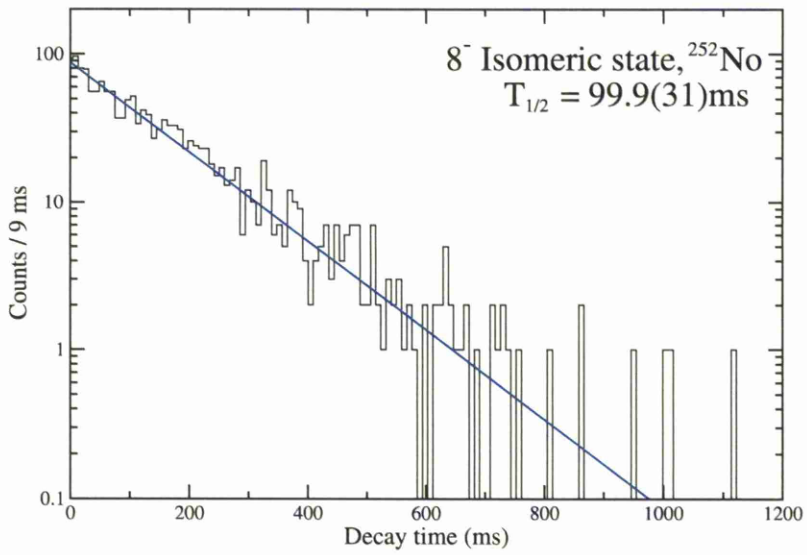

Figure 5.3: Time of decay after implantation of ^{252}No recoils from the 8^- isomeric state. Fitted function to find half-life also shown.

Table 5.2: Details of RDT and RT ground state decays and of which those tagged also in the isomeric state. Half-lives and isomeric proportions found using RDT results are also shown. The total half-lives were found using spectra of all constituent events combined.

Nuclei tagged via mode	$^{252}No_{SF}$	$^{252}No_{\alpha}$	$^{248}Fm_{\alpha}$	$^{244}Cf_{\alpha}$	total
RDT	3720	3657	1667	626	9670
$T_{1/2}$ of ^{252}No (s)	2.26(5)	2.32(9)	-	-	2.35(4)
R-ce-DT	797	747	429	154	2127
$T_{1/2}$ of 8^- state (ms)	100.0(48)	96.3(46)	119.9(93)	100(18)	99.9(31)*
Isomeric proportion(%)	21.4(8)	20.4(8)	25.7(14)	24.6(22)	20.9(6)*
RT	-	-	-	-	35359
R-ce-T	-	-	-	-	3172

* Calculated excluding $^{248}Fm_{\alpha}$ and $^{244}Cf_{\alpha}$ decay tagged events (see 5.1.3 for details).

the efficiency of detection for tagging recoils by each decay mode.

To estimate the random misassignment rate, where background events are mistakenly assigned as the decay from a tagged recoil, we may employ a somewhat simplified model. The assumption was taken that recoil tagged implants and background events were evenly distributed upon the DSSSD pixels. This leads to the consideration of the number of RT events, R, per pixel multiplied by the length of the decay tagging time gate, t, giving the possible time over which a background event would cause a missassignment per pixel. This may be found as a proportion of the total experiment time T, giving $R{\cdot}t/T{\cdot}P$ where P is the number of pixels. An estimate of the number of missassignments may be given by the number of background events in anti-coincidence with the MWPC which occur within the gated energy, B, per pixel multiplied by this proportion. Multiplied over all pixels P, an estimate is given as

$$N_{random} = \frac{R \cdot B \cdot t}{T \cdot P}. \tag{5.3}$$

This model makes the assumption that either $R{\cdot}t/P$ or $B{\cdot}t/P \ll T$, so that these values as a proportion of T may sum linearly with no consideration of overlaps. It was also assumed that any background events in the DSSSD were randomly occurring and that the background and tagged recoil rates remained constant over the run. The proportion of recoil tagged events which measured a subsequent real event were ignored, leaving it to a possible misassignment over the whole time gate t.

The number of randomly occurring misassignments has been estimated using Equation 5.3 for the different tagged events and the results are given in Table 5.3. For ^{252}No α decay events the random misassignment estimate is negligible.

When tagging recoil decays via spontaneous fission, an overflow energy signal is used with an energy gating of >15 MeV. This makes it difficult to estimate the number of background events in anti-coincidence with the MWPC and hence, the amount of misassignments. However, the total background B was taken to be equal to the number of counts seen >15 MeV in anti-coincidence with the MWPC (B = 18,700), this gives an estimate for the number of random misassignments of around

Table 5.3: Estimate of the number of misassigned tagged events due to randomly correlated background N_{random} for all possible recoil decay tagging methods calculated using Equation 5.3. R gives the total number of recoil tagged events implanted onto the DSSSD and B is the total background events in the DSSSD occurring within the energy gate used. T is the total time of the experimental run and t is the time of the gate used to look for a subsequent decay, with P giving the total number of DSSSD pixels.

event	R	B	t (s)	T ($\times 10^5$ s)	P	N_{random}
RDT						
$^{252}No_{\alpha}$	3.54×10^4	788	20	7.96	4.8×10^3	0.2
$^{252}No_{SF}$*	3.54×10^4	1.87×10^4	20	7.96	4.8×10^3	4
$^{248}Fm_{\alpha}$	3.54×10^4	980	240	7.96	4.8×10^3	2
$^{244}Cf_{\alpha}$	3.54×10^4	757	3.50×10^3	7.96	4.8×10^3	25
R-ce-DT	9.67×10^3	3.66×10^6	0.7	7.96	4.8×10^3	6
R-ce-T	3.54×10^4	3.66×10^6	0.7	7.96	4.8×10^3	24

* Value is overestimate, see text for details.

4. It can therefore be concluded, that a negligible number of random misassignments are present for the spontaneous fission tagged RDT events. This is borne out by the results in Table 5.2 which details the tagged events via the 4 different ground state decays and also, those additionally tagged in the isomeric state. The fact that the isomeric proportions are consistent along with the half-lives obtained from alpha and spontaneous fission decay tagging, suggest no significant difference in the number of misassignments occurring between the two. Also this again shows the spontaneous fission tagging method is sound.

The efficiency of ^{252}No α decay detection in the DSSSD-Y strips, ϵ_{α}, may be measured using the assumption that α decays that do not deposit their full energy, will deposit at least some. By tagging all ^{248}Fm α decays after a recoil tag, in the same pixel, a clean ^{252}No α spectrum may be acquired by looking at events in the pixel between the recoil and ^{248}Fm α. The spectrum is then used to find the number of counts falling in the $^{252}No_{\alpha}$ gate used, N_{tagged}, and the number of counts with

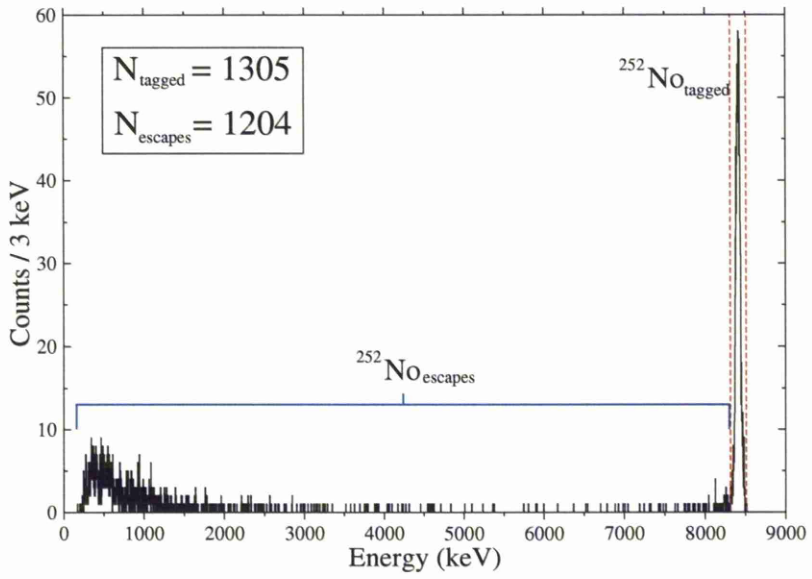

Figure 5.4: Energies of events in DSSSD-Y after a recoil tagged implant and before a ^{248}Fm α decay all in the same pixel. Shows full and partial ^{252}No α energy deposition in the detector with ^{252}No$_\alpha$ energy gate used in analysis highlighted as red dashed lines.

energies below this, N_{escape}. The efficiency of ^{252}No α detection is then given by

$$\epsilon_\alpha = \frac{N_{tagged}}{N_{escape} + N_{tagged}}. \tag{5.4}$$

To avoid including any ^{252}No recoils decaying via conversion electron emission from the isomeric state, a time gate of 0.8 s $\rightarrow$ 15 s was set for the events. The resulting spectrum is shown in Figure 5.4 where N_{tagged} = 1305$\pm$36 and N_{escape} = 1204$\pm$35. From the isomeric proportion it was estimated a negligible number of the low energy events were due to isomeric decays occurring after 0.8 s. The resulting efficiency was found to be ϵ_α = 0.521$\pm$0.018. This is consistent with geometric considerations of implants on the DSSSD surface emitting the α particle away from the detector 50 % of the time. A value of ϵ_{SF} = 1 was assumed, as fission fragments are projected in opposite directions.

The ground state of ^{252}No decays via alpha, spontaneous fission and an electron capture process for which the known value of $b_{EC} = 0.8\%$ [49] was taken. By taking the ratio between the branching fractions of the α and spontaneous fission decay modes, it can be written

$$\frac{b_\alpha}{b_{SF}} = \frac{N^*_\alpha}{N^*_{SF}} = \frac{N_\alpha}{N_{SF}} \cdot \frac{\epsilon_{SF}}{\epsilon_\alpha} \tag{5.5}$$

where N^* is the number actually emitted and N is the number detected from RDT events given in Table 5.2. Given also that

$$b_\alpha + b_{SF} + b_{EC} = 1 \tag{5.6}$$

then Equations 5.5 and 5.6 may be substituted and rearranged to give the α and spontaneous fission branching fractions as

$$b_\alpha = \frac{1 - b_{EC}}{(N_{SF}/N_\alpha) \cdot (\epsilon_\alpha/\epsilon_{SF}) + 1}, \tag{5.7}$$

$$b_{SF} = \frac{1 - b_{EC}}{(N_\alpha/N_{SF}) \cdot (\epsilon_{SF}/\epsilon_\alpha) + 1}. \tag{5.8}$$

Values given as percentages of $b_\alpha = 64.8(27)\%$ and $b_{SF} = 34.4(14)\%$ were found and the value of b_{SF} is compared with those previously found in Figure 5.5. The result compares well with those previously found from [54] and [39], but the spontaneous fission fraction is somewhat above that quoted in [53, 46, 50].

5.1.3 Isomeric state

It is firstly important to discuss a misassignment effect observed when tagging nuclei in an isomeric state from their conversion electron emissions as proposed by Jones [17].

Figure 5.6 shows the time of the conversion electron decay for all R-ce tagged events after the tagged recoil implantation with both linear and logarithmic scales. Over the short time scale we see the desired isomeric decays and also a low level random misassignment rate due to background in the DSSSD. From the rate observed

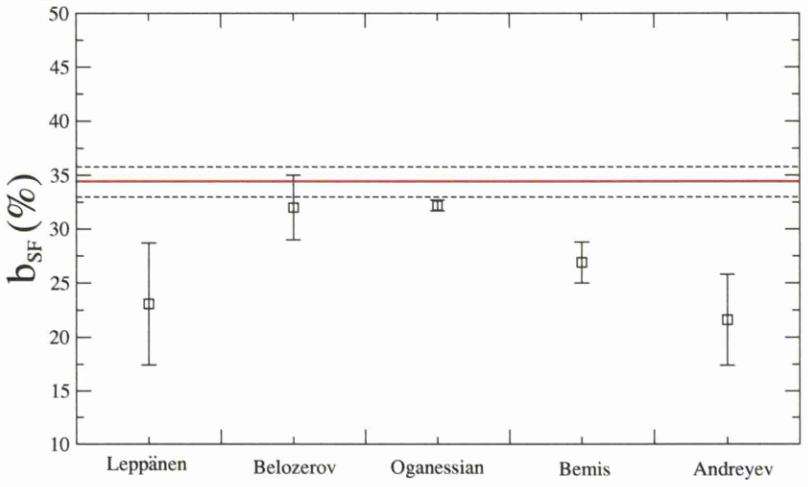

Figure 5.5: Value obtained for the spontaneous fission branching fraction in ^{252}No b_{SF} (red line) compared with those found in [54], [39], [53], [46] and [50] respectively.

in the Figure, this would give around 31 random misassignments within the isomeric time gate, which compares well with the result from the approximated model given in Table 5.3 which gave 24. This value, along with $N_{random} = 6$ for R-ce-DT events are satisfactorily low. There is also however, a clear contribution from the decaying ground state of ^{252}No, indicated by the half-life, when gating for conversion electrons between 37 and 500 keV. These events are thought to be predominantly due to ^{252}No recoils implanted in the ground state where by ~50% of their emitted α particles are away from the surface of the DSSSD. They then deposit only a small fraction of their full α energy as shown in Figure 5.4. This can cause a tagged recoil, implanted in the DSSSD in its ground state, to be misassigned as an isomeric event. From the decay curves in Figure 5.6 it was found that 7.2(10)% of isomeric R-ce tagged events were actually implanted in the ground state. This proportion is enhanced by the fact that the half-lives of the isomeric and ground state decays are not several orders of magnitude apart. It can be seen that this misassignment effect is much more prominent than that caused by random background in the DSSSD in this case, which accounts for only 1.0(1)% of R-ce-T events. It should also be noted that this effect is

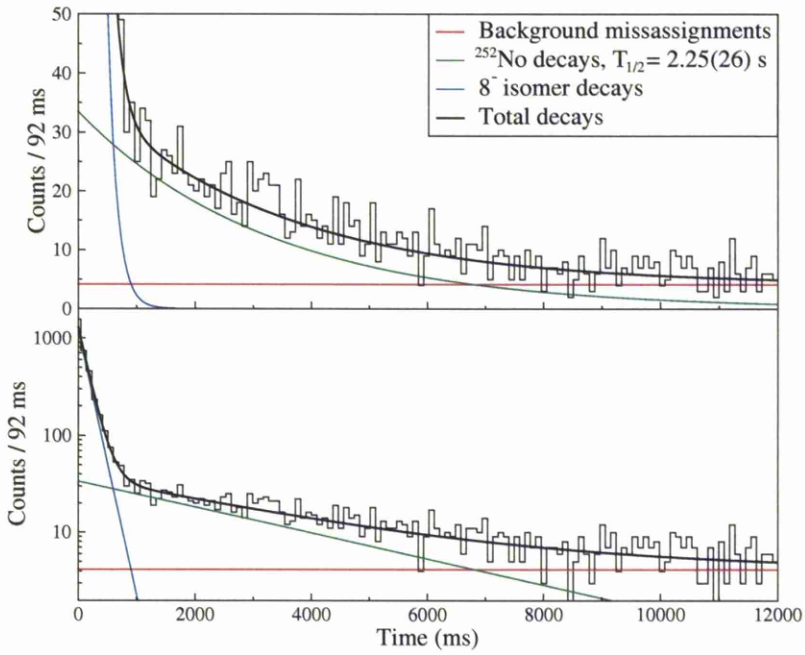

Figure 5.6: Time after implantation of R-ce tagged isomeric decay events, with fitted functions for the constituent decays are shown. Given with both linear (a) and logarithmic (b) scales.

not predicted by the model represented in Equation 5.3, due to the assumption taken that the background was randomly occurring.

This effect is also present in R-ce-DT isomer events if the ground state decay tag used is that of $^{248}\mathrm{Fm}_{\alpha}$ or $^{244}\mathrm{Cf}_{\alpha}$. Figures 5.7 and 5.8 show the isomer conversion electron and decay time spectra respectively of R-ce-DT events, split between the four possible ground state decay mode tags used. In both cases the spectra are clean for a subsequent ^{252}No ground state decay, but significant background appears >500 keV for E_{ce} and >700 ms for decay time when using the $^{248}\mathrm{Fm}_{\alpha}$ or $^{244}\mathrm{Cf}_{\alpha}$ tags. This again indicates ^{252}No α decays present in the spectra and shows once more the dominance of this as a cause for misassignments, over those due to random background which will be present using all ground state decay tags. The proportion of these misassignments when using $^{248}\mathrm{Fm}_{\alpha}$ or $^{244}\mathrm{Cf}_{\alpha}$ tags will be around twice that for R-ce tagged events at 14.4(20)% as preceeding ^{252}No α decays will be emitted away from the DSSSD ~100% of the time as opposed to ~50%. These misassignments explain the increased proportion of ^{252}No recoils produced in the isomeric state when using $^{248}\mathrm{Fm}_{\alpha}$ or $^{244}\mathrm{Cf}_{\alpha}$ as opposed to ^{252}No ground state tags, as shown in Table 5.2. This is also the reason that these events are omitted when finding properties such as the isomeric half-life. The total misassignment proportion due to this effect for R-ce-DT isomeric events, including also those using ^{252}No ground state tags, is then found to be 4.0(6)%. In light of this effect it is important to take care when analysing isomer tagged spectra. Reference to the R-ce-DT spectra using only ground state ^{252}No decays as tags is important, as these are not susceptible to this misassignments effect.

Focal plane γ-ray spectroscopy was performed using the PLANAR and CLOVER detectors and Figure 5.9 shows spectra in coincidence with the conversion electron decay tag for R-ce-DT events. The transitions observed are from the decay of the 8^- isomeric state and transitions from both within the 2^- side band and those to and within the ground state band, can be seen. This is consistent with the observations by Sulignano [24] as given in the level scheme in Figure 5.1.

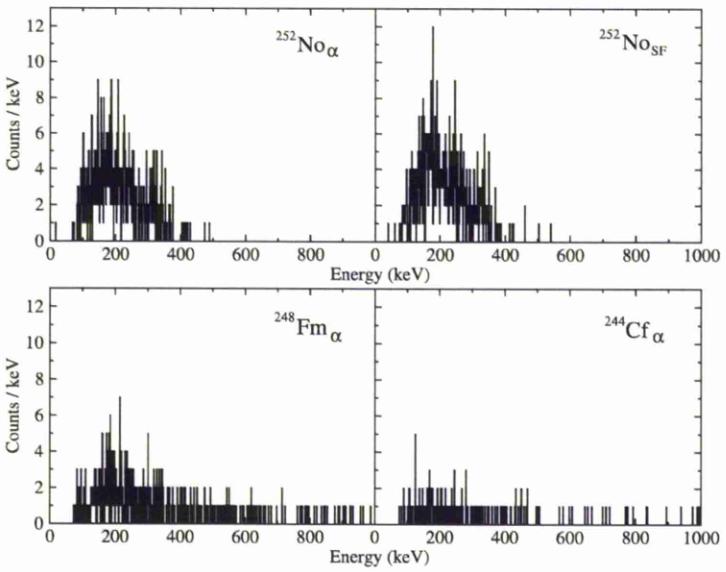

Figure 5.7: R-ce-DT isomer decay conversion electron energy spectra in the DSSSD-X strips using ground state decay tags of $^{252}\mathrm{No}_{\alpha}$, $^{252}\mathrm{No}_{SF}$, $^{248}\mathrm{Fm}_{\alpha}$ and $^{244}\mathrm{Cf}_{\alpha}$.

5.2 In-beam decays

5.2.1 Ground state

The ground state rotational band has been studied previously [47] up to $I^{\pi} = 20^{+}$. The present study does not add to these prvious results but is included for the sake of completeness.

In-beam JUROGAM spectra were obtained for RT and RDT ^{252}No recoils in the ground state. In this case the RDT events, where a time and energy gated conversion electron signal was detected in the DSSSD-X strips after implantation and before the ground state decay, were dismissed as they were taken to have been formed in the isomeric state. These spectra gave prompt γ rays from the ground state rotational band of ^{252}No and are shown in Figure 5.10, with RT events shown in the top panel. The middle panel shows RDT spectra where only $^{252}\mathrm{No}_{\alpha}$ and $^{252}\mathrm{No}_{SF}$ decay tags have been used, whereas the bottom panel uses additional subsequent decay tags

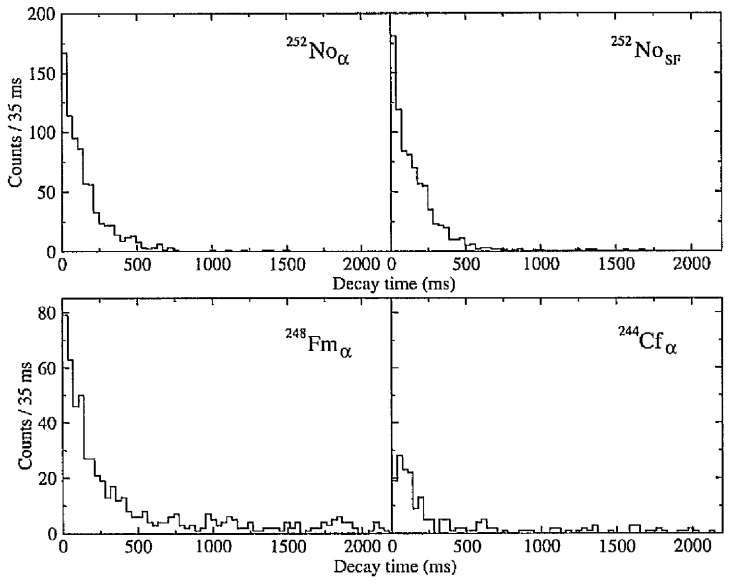

Figure 5.8: R-ce-DT isomeric state decay time spectra using ground state decay tags of $^{252}\mathrm{No}_{\alpha}$, $^{252}\mathrm{No}_{SF}$, $^{248}\mathrm{Fm}_{\alpha}$ and $^{244}\mathrm{Cf}_{\alpha}$.

from $^{248}\mathrm{Fm}_{\alpha}$ and $^{244}\mathrm{Cf}_{\alpha}$ and an improvement to statistics can be seen. The energies of the ground state transitions for RT and RDT spectra are given in Table 5.4. The fitted intensities of the RDT peaks are given along with those corrected for efficiency and also with an additional correction for internal conversion. The internal conversion coefficients α, were found using reference [31] and are also given in the Table. The 107 keV ($4^+ \rightarrow 2^+$) transition, which will appear as a doublet as shown in Figure 5.1, may be fitted in the RT spectrum. By using the other fitted intensities in the spectrum along with the energy efficiencies and conversion coefficients for the transitions, then an expected intensity of around 12 counts is found for this transition. As an intensity of 36(12) was fitted, this indicates possible contributions from the 2^- band transition, along with other backgrounds that are present in this lower energy region. The fitted energy has therefore been assigned as tentative. The ground state band transition energies are fully consistent with those previously found [47], but unfortunately, no additional transitions from higher spin states were observed.

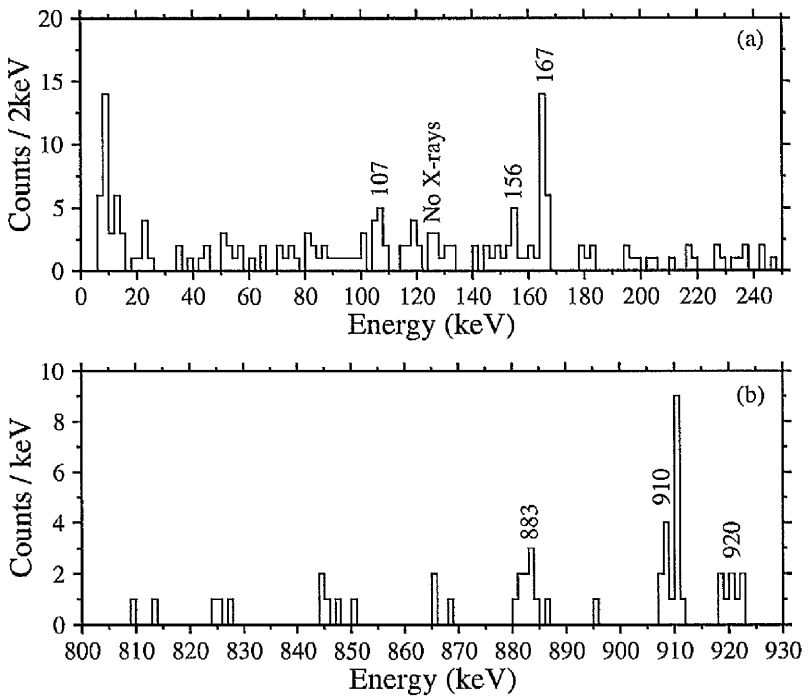

Figure 5.9: Focal plane γ-ray spectra in coincidence with conversion electron tag of R-ce-DT events obtained by PLANAR (a) and CLOVER (b) detectors.

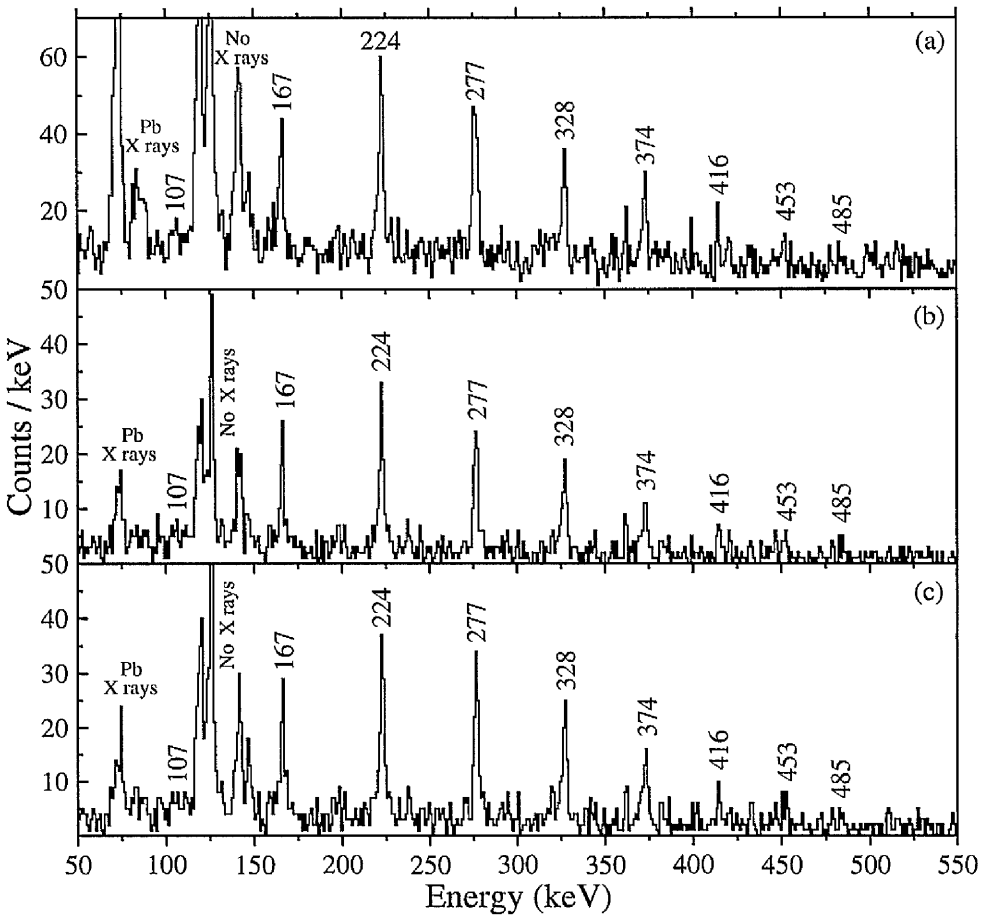

Figure 5.10: In-beam γ-ray spectra of decays within the ground state rotational band. Ground state recoils were tagged via (a) RT, (b) RDT, whereby a subsequent $^{252}\mathrm{No}_{\alpha/SF}$ tag was selected and (c) RDT which also used $^{248}\mathrm{Fm}_{\alpha}$ and $^{244}\mathrm{Cf}_{\alpha}$ tags.

Table 5.4: Transition energies from the ground state rotational band of ^{252}No from both RT and RDT spectra. Fitted intensities of transitions from RDT spectra are shown and also those corrected for detector efficiency and normalised to $8^+ \rightarrow 6^+$ transition are given, along with those given additional correction for conversion coefficients. The values for the total conversion coefficient for each transition is given as α [31].

$I_i \rightarrow I_f$	RT (keV)	RDT (keV)	$\mathcal{I}$	$\mathcal{I}^{\dagger}$	$\mathcal{I}^{\dagger\dagger}$	α
$2^+ \rightarrow 0^+$	46.39(3)*	46.54(5)*	-	-	-	1180
$4^+ \rightarrow 2^+$	(106.6(8))	107.74(12)*	-	-	-	22.4
$6^+ \rightarrow 4^+$	166.85(21)	167.16(25)	64(10)	66(10)	139(21)	3.24
$8^+ \rightarrow 6^+$	223.56(15)	223.65(18)	103(11)	100(11)	100(11)	1.02
$10^+ \rightarrow 8^+$	277.34(17)	277.59(16)	96(11)	97(11)	71(8)	0.470
$12^+ \rightarrow 10^+$	328.39(19)	328.02(21)	65(10)	70(10)	44(6)	0.273
$14^+ \rightarrow 12^+$	374.25(21)	373.8(5)	58(9)	66(10)	39(6)	0.184
$16^+ \rightarrow 14^+$	415.53(18)	415.6(3)	16(5)	20(6)	11(3)	0.137
$18^+ \rightarrow 16^+$	452.6(4)	453.3(4)	9.1(4)	11(5)	6(3)	0.109
$20^+ \rightarrow 18^+$	-	484.6(6)	9.1(4)	12(5)	6(3)	0.092

* Energy extrapolated using Harris fit.

† Intensities corrected for detector efficiency.

†† Intensities corrected for detector efficiency and conversion coefficients.

As the conversion coefficients for the lower order transitions are large, then the γ-ray peaks from the $I^{\pi} = 4^{+}$ and 2^{+} levels are not clearly observed in the spectra. They can however, be extrapolated from the other transition energies in a band using a Harris fit as detailed in [55, 56, 57]. This involves fitting the kinematic and dynamic moments of inertia to even powers of their rotational frequency to give the relationships

$$\Im^{(1)} = J_0 + J_1\omega^2, \tag{5.9}$$

$$\Im^{(2)} = J_0 + 3J_1\omega^2 \tag{5.10}$$

where J_0 and J_1 are the Harris parameters to be found. The assigned spins and transition energies in the rotational band may be used to find the moments of inertia from Equations 2.19 and 2.20 as

$$\Im^{(1)}(I) = \hbar^2 \frac{(2I-1)}{E_{I\rightarrow I-2}}, \tag{5.11}$$

$$\Im^{(2)}(I) = \frac{4\hbar^2}{E_{I+2\rightarrow I} - E_{I\rightarrow I-2}}. \tag{5.12}$$

The rotational frequencies associated with the kinematic and dynamic moments inertia are found as

$$\hbar\omega = \frac{E_{I\rightarrow I-2}}{\sqrt{I(I+1)} - \sqrt{(I-2)(I-1)}}, \tag{5.13}$$

$$\hbar\omega = \frac{E_{I+2\rightarrow I} + E_{I\rightarrow I-2}}{4} \tag{5.14}$$

respectively. Equation 5.10 is then integrated as $\Im^{(2)}(\omega) = dI/d\omega$ to give

$$I(\omega) = J_0\omega + J_1\omega^3 + \frac{1}{2}. \tag{5.15}$$

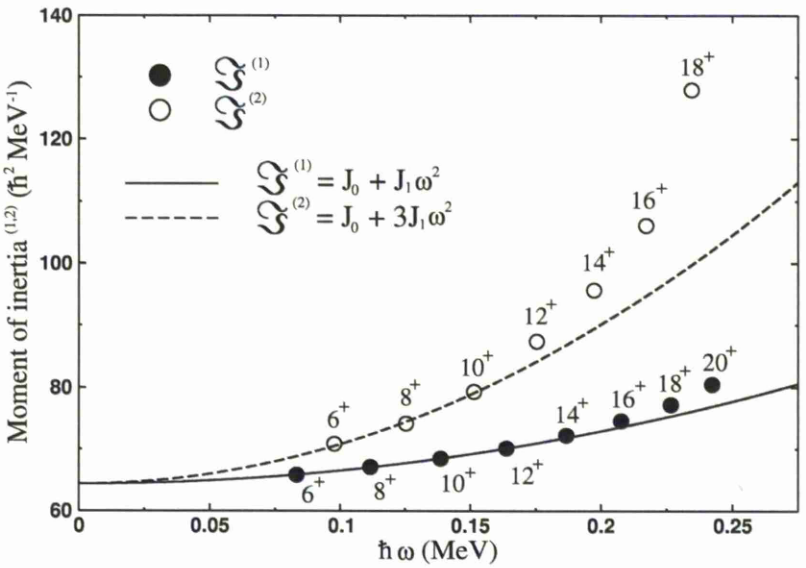

Figure 5.11: Plot of kinematic (black points) and dynamic (white points) moments of inertia against rotational frequency for the ground state band of ^{252}No, from RDT spectra energies. The first 4 points for the kinematic and first 3 for the dynamic have been used to obtain the Harris parameters $J_0 = 64.35(7)\ \hbar^2\text{MeV}^{-1}$ and $J_1 = 215(3)\ \hbar^4\text{MeV}^{-3}$.

The ω value can therefore be found for the spin I of an unobserved transition. The energy of the transition may then be obtained as $\omega = dE/dI$ where $dI = 2$ and therefore $E_\gamma = 2\omega$.

Figure 5.11 shows the kinematic and dynamic moments of inertia plotted as a function of the rotational frequency for the first eight visible transitions using the RDT spectra. Harris parameters of $J_0 = 64.35(7)\ \hbar^2\text{MeV}^{-1}$ and $J_1 = 215(3)\ \hbar^4\text{MeV}^{-3}$ were found using points from levels I_i $6 \rightarrow 12$ for $\Im^{(1)}$ and $6 \rightarrow 10$ for $\Im^{(2)}$. At higher spin, the fit breaks down as individual nucleon's angular momenta begin to align with the collective rotation. These contributions mean that the assumption of the classically rotating relationships 5.9 and 5.10 are no longer valid. The energies obtained for the two lowest ground state band transitions are given in Table 5.4.

5.2.2 Isomeric state

In-beam γ-ray spectra were obtained showing transitions above the 8^- isomeric state for the first time and are given in Figure 5.12(a) using R-ce-T (upper panel), R-ce-DT with $^{252}\mathrm{No}_{\alpha/SF}$ tags (middle panel) and R-ce-DT with additional $^{248}\mathrm{Fm}_{\alpha}$ and $^{244}\mathrm{Cf}_{\alpha}$ tagged events (lower panel). Figure 5.12(b) shows the γ-γ coincidence spectra from R-ce-T (upper panel) and the R-ce-DT (lower panel) events whereby γ-ray events were only accepted if they occurred in coincidence with another in the JUROGAM array. The prompt γ-ray transitions detected are interpreted as decays from a rotational band built upon the 8^- isomeric state, their fitted energies, intensities and efficiency corrected relative intensities are given in Table 5.5, found from the R-ce-T spectrum, along with their spin and mulitipolarity interpretations. The somewhat weaker transitions with $I_i = 20 \rightarrow 22$ have been shown as tentatively assigned; a contributing factor to this is that they do not appear significantly in the γ-γ coincidence spectra. The level scheme has been extended to include these transitions and is shown in Figure 5.1. Interband transitions shown in brackets are those inferred from the observed transitions between the two signature bands.

The justification for assigning the γ-ray transitions above the isomer to a rotational band structure of two signatures, is in line with the theoretical model described in Section 2.4 of strongly coupled rotational bands for deformed nuclei in $K \neq 0$ states. Other nuclei in the region such as ^{254}No and ^{250}Fm also display similar K-isomeric states with analogous rotational band structures [43, 21].

The misassignment effect discussed in Section 5.1.3, means that possible ground state band transitions may be observed in isomer tagged rotational band spectra. This would throw into question the 224 keV peak, as it is present also in the ground state band but the R-ce-DT spectra using only $^{252}\mathrm{No}_{\alpha/SF}$ decay tags also shows this peak. This is the only spectrum unaffected by this misassignment mechanism, therefore the transition may be taken as occurring within the isomeric rotational band. Also no other prominent ground state peaks significantly appear in any of the spectra.

To help assign the spins of the levels, a Harris fit may be performed as detailed

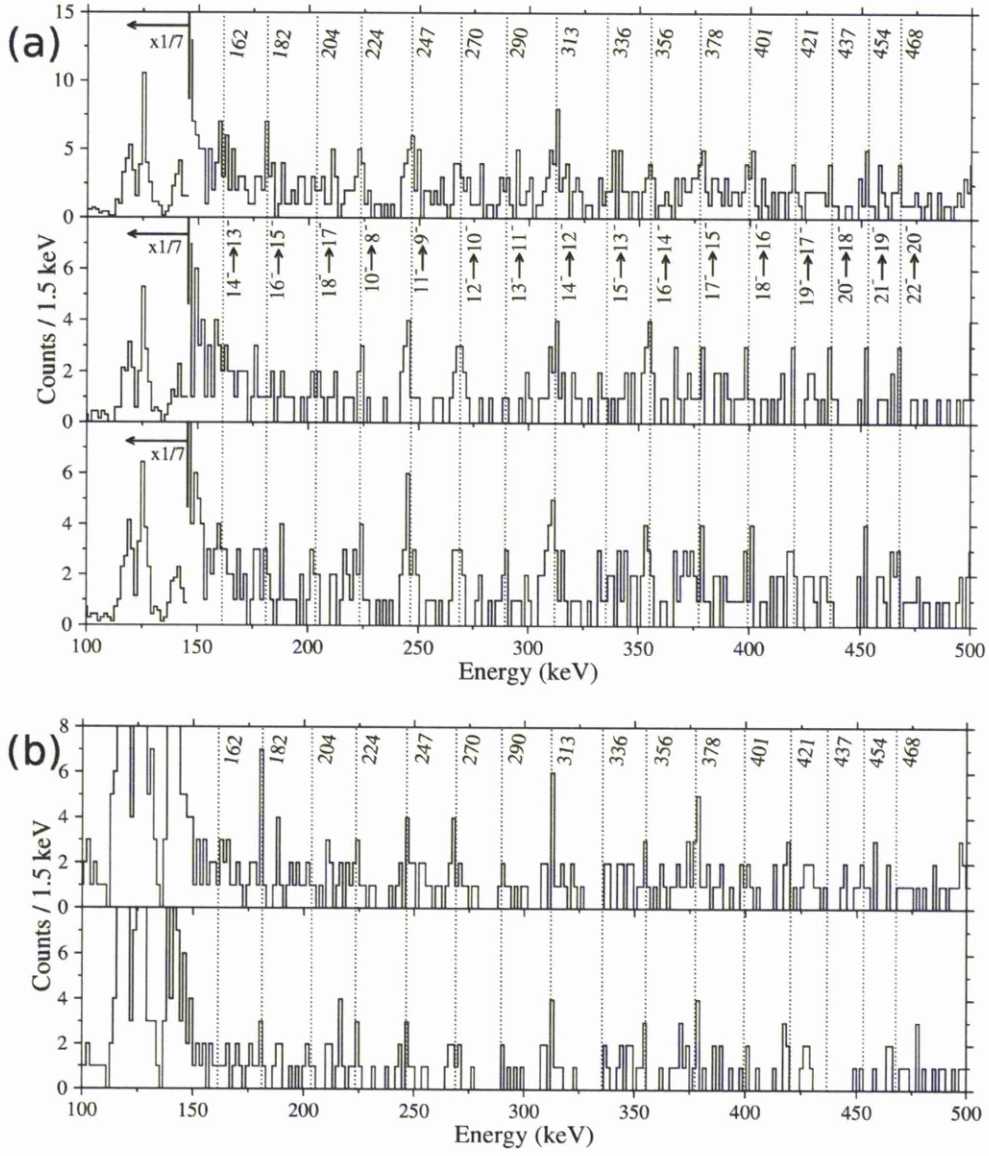

Figure 5.12: In-beam γ-rays of transitions within rotational band above 8^- isomeric state (a). Events are R-ce-T (upper panel), R-ce-DT with $^{252}\mathrm{No}_{\alpha/SF}$ decay tags (middle panel) and R-ce-DT with additional $^{248}\mathrm{Fm}_{\alpha}$ and $^{244}\mathrm{Cf}_{\alpha}$ tags (lower panel). Spectra (b) show γ-γ coincidences of R-ce-T (upper panel) and R-ce-DT (lower panel) events.

Table 5.5: Energies, spin assignments and multipolarities of transitions in rotational band built on the 8^- isomeric state from spectrum of R-ce-T events. Efficiency corrected intensities also shown and scaled to the the 312.8 keV transition.

$I_i \rightarrow I_f$	$\sigma\lambda$	$E\gamma$	$\mathcal{I}$	$\mathcal{I}^\dagger$
$(10)^- \rightarrow (8)^-$	E2	224.2(7)	5.9(32)	47(25)
$(11)^- \rightarrow (9)^-$	E2	247.2(6)	8.2(34)	66(27)
$(12)^- \rightarrow (10)^-$	E2	269.6(8)	6.8(33)	56(27)
$(13)^- \rightarrow (11)^-$	E2	290.3(14)	5.1(31)	43(26)
$(14)^- \rightarrow (12)^-$	E2	312.8(8)	11.6(38)	100(33)
$(15)^- \rightarrow (13)^-$	E2	336.1(14)	4.0(28)	36(25)
$(16)^- \rightarrow (14)^-$	E2	355.9(7)	4.1(29)	37(26)
$(17)^- \rightarrow (15)^-$	E2	378.3(20)	5.4(33)	51(31)
$(18)^- \rightarrow (16)^-$	E2	400.7(7)	5.8(32)	56(31)
$(19)^- \rightarrow (17)^-$	E2	421.0(6)	2.1(23)	21(23)
$(20)^- \rightarrow (18)^-$	E2	(437.4(7))	2.1(28)	21(28)
$(21)^- \rightarrow (19)^-$	E2	(453.9(6))	4.4(34)	45(35)
$(22)^- \rightarrow (20)^-$	E2	(468.5(8))	3.5(33)	36(34)
$(14)^- \rightarrow (13)^-$	E2/M1	162.1(10)	11.7(40)	100(34)
$(16)^- \rightarrow (15)^-$	E2/M1	181.9(7)	8.2(36)	67(29)
$(18)^- \rightarrow (17)^{-*}$	E2/M1	204.3(9)	-	-

† Intensities corrected for detector efficiency.

* Energy fitted from the R-ce-DT spectrum.

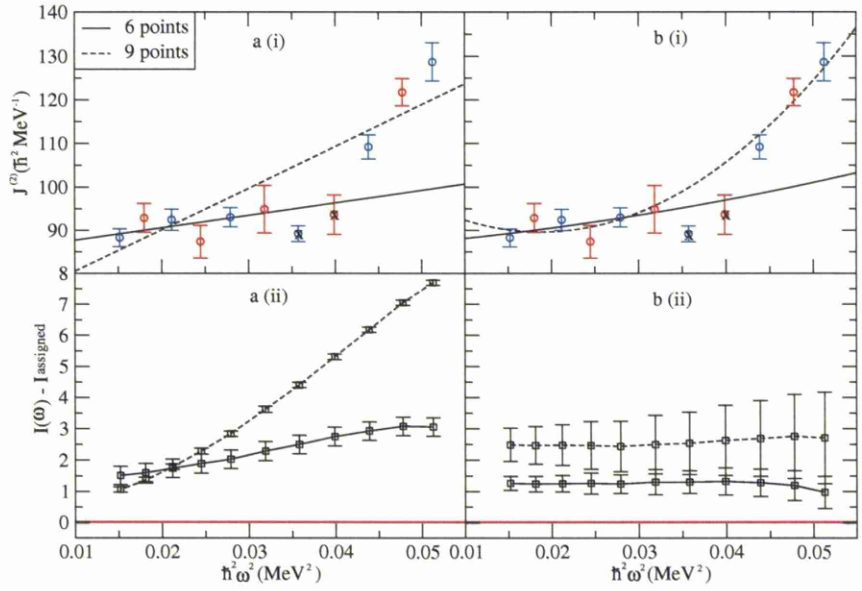

Figure 5.13: a(i) and b(i) show the dynamic moment of inertia fitted as a function ω^2 using linear and quadratic polynomials respectively. The solid lines show fits using the first six points, whereas the dashed show those using all but the two omitted points highlighted with crosses. a(ii) and b(ii) show the difference between the subsequently found spin of each level and the assigned value.

in [55, 56, 57]. Here the $\Im^{(2)}$ is plotted against ω as in Section 5.2.1 for the ground state but fitted also with the addition of the next term in the ω^2 series giving

$$\Im^{(2)} = A + B\omega^2 + C\omega^4, \tag{5.16}$$

to obtain values of the coefficients A, B and C. The fits are shown in Figures 5.13 (a)(i) and (b)(i) using coefficients up to B and C respectively. The odd and even spin partner band levels are shown as the red and blue points respectively, as they may be considered as two separate bands of $\Delta I = 2\hbar$ transitions. The points highlighted with black crosses have been omitted, which will be discussed further in Section 6.1, and the dashed line represents the fit using all nine remaining points, whereas the solid line gives that using only the first six. Equation 5.16 is integrated with respect to ω to give

$$I(\omega) - I_0 = A\omega + (B/3)\omega^3 + (C/5)\omega^5 + \frac{1}{2} \tag{5.17}$$

which gives the spin of the state $I(\omega)$ minus any aligned spin I_0 as a function of ω. The difference between the spin found from Equation 5.17 and that assigned, is given in Figures 5.13 (a)(ii) and (b)(ii) and does not appear to confirm the spin assignment when considering any of the fits.

Firstly, the method of the Harris fit appropriated to this case must be discussed. The method has been seen to work well when considering even-even nucleus' ground state rotational bands, but in this case, the transitions arise from two signature partner bands of $\Delta I = 2\hbar$. Shifting in energy may occur between them due to various effects and a smooth $\Im^{(2)}$ vs ω^2 may not be seen. This method should be taken as, at best, a guide to the spin assignments of transitions in this case and the uncertainty is exacerbated by the low statistics leading to large errors in the transition energies. This also makes it difficult to infer the rotational frequency at which the assumptions of the Harris fit break down. The inherent uncertainty in both the method applied and the transition energies, means that the implication of results in Figure 5.13 of an unobserved $10^- \rightarrow 8^-$ transition below the 224 keV should not be

assumed. Instead, the fact that no clear transition is seen below the 224 keV, where one would be expected, leads to the somewhat tentative assignment of this as the $10^- \rightarrow 8^-$ transition, accepting the $I^\pi = 8^-$ spin of the isomer found in [24]. More data in this case would act to further enlighten the situation.

5.3 Structural assignment of the 8^- K isomer

Predictions of quasi-particle excitations in ^{252}No by Delaroche et al. [52] using Hartree-Fock-Bogoliubov, mean field method finds the lowest lying 8^- state as a two quasi-particle neutron $8^-\{\frac{7}{2}^+[624]_\nu \otimes \frac{9}{2}^-[734]_\nu\}$ (s_1) excitation expected at an energy of 1070 keV, with no two quasi-particle proton excitations below 2.5 MeV. However, quasi-particle energies predicted by self-consistent mean field methods are generally less reliable than those found using macroscopic-microscopic methods. The single quasi-particle energies were found to be at best only within 500 keV of the observed energies for calculations found by Afanasjev [58] in this mass region and can be up to 1 MeV out. Macroscopic-microscopic calculations using a Woods-Saxon potential by Xu [42] show also a possible two quasi-particle proton $8^-\{\frac{9}{2}^+[624]_\pi \otimes \frac{7}{2}^-[514]_\pi\}$ (s_2) state at an energy of 1480 keV. The difference in predicted K-isomeric states is due to the variations in single particle energy levels found when using the two theoretical approaches.

To identify the structure of the isomeric state, we can exploit the difference in the nuclear g_K factors associated with different configurations. This will alter the inter/intraband γ-ray branching ratios from levels within strongly coupled rotational bands according to the Equation 4.1. The g_K factors for the two quasi-neutron (s_1) and proton (s_2) configurations detailed above, are given as +0.01 and +1.01 respectively. The low statistics provided for the rotational band spectra above the 8^- isomeric state shown in Figure 5.12(a), means that the use of γ-ray intensity ratios between inter/intraband transitions from single levels in the rotational band are inconclusive in assigning its structure. The analytical methods discussed in Chapter

Table 5.6: Proposed configurations of the 8^- isomeric state in ^{252}No.

symbol	configuration	g_K factor
s_1	$8^-\{\frac{7}{2}^+[624]_\nu \otimes \frac{9}{2}^-[734]_\nu\}$	+0.01
s_2	$8^-\{\frac{9}{2}^+[624]_\pi \otimes \frac{7}{2}^-[514]_\pi\}$	+1.01

4 will therefore be employed, whereby the intensities from multiple levels are cumulated. In the analysis a quadrupole moment of $Q_0 = 12.98$ eb was used and the core gyromagnetic factor was taken as $g_R\ (= Z/A) = 0.405$ with results also given when applying a quenching of $q = 0.7$, this was taken in line with the discussion in Section 2.6. The transition energies and spin assignments shown in Figure 5.1 will be used for this analysis. The spins of the levels are tentatively assigned, but it is seen that a change of $\pm 1\hbar$ on these values produces only a small deviation in the N_s and N_{xs} values obtained.

5.3.1 Cumulative γ-ray branching ratios

The cumulative γ-ray branching ratios method described in Section 4.2 was applied to the R-ce-T γ-ray spectrum of transitions above the 8^- isomer in ^{252}No shown in Figure 5.12(a) (upper panel). The p-values found using Equations 4.7 and 4.8 were 0.59 for s_1 and 0.14 for s_2 using an unquenched g_R with values and results shown in Table 5.7 and Figure 5.14(a). The N_s values from Equation 4.3 were obtained using six intraband peak intensities from $I_i = 14 \rightarrow 19$ and a background rate of 1.04 counts/keV was used for the interband region in the spectrum. N_o was found using ranges of 4 keV width with ΔE_o values of ± 4 keV used. A value of ΔE_o = -2 keV, highlighted in the Figure and Table, is indicated by the correspondence to the maximum N_o and also relates to those energies observed for the interband transitions. An investigation into the effect of quenching is shown in Figure 5.14(b) for a value of $q = 0.7$. Here the p-values are reduced to 0.10 and 0.02 for s_1 and s_2 respectively, indicating an inclination towards an unquenched g_R.

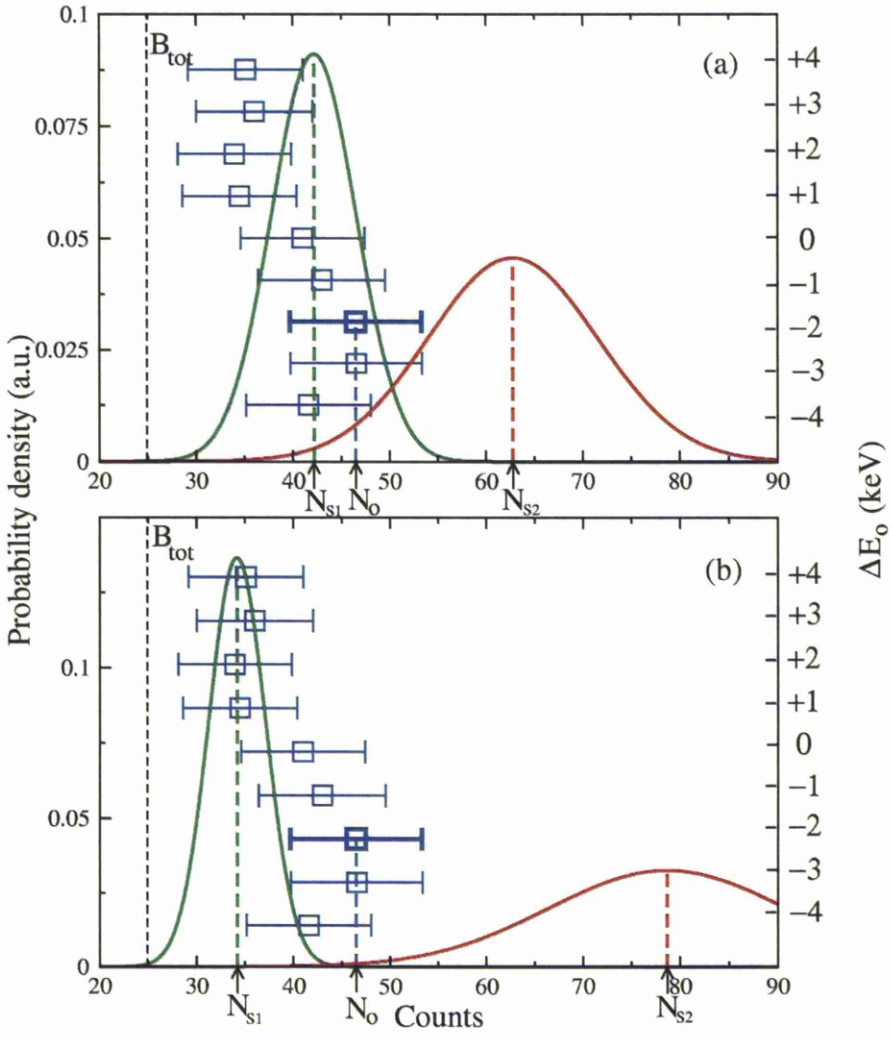

Figure 5.14: Expected total counts $N_s \pm \sigma_s$ found for two structures s_1 (green) and s_2 (red) using R-ce-T γ-ray spectrum of rotational band above 8^- isomer in ^{252}No applying cumulating γ-ray branching ratios method. Observed counts $N_o \pm \sigma_o$ (blue) highlighted for ΔE_o = -2 keV. Performed with $q = 1$(a) and 0.7(b), also shown is the total background B_{tot} added for N_s values.

Table 5.7: Selected p-values and quantities in finding them for ^{252}No 8^- isomer using cumulative γ-ray branching ratios method for R-ce-T results. The values for ΔE_o = -2 found are highlighted.

structure	ΔE_o(keV)	N_s	N_o	$\lvert D_e \rvert$	$(\sigma_s{}^2+N_o)^{1/2}$	p
s_1 $(q = 1)$	-4	42.17(4.39)	41.5	0.55	7.81	0.94
	-2	42.17(4.39)	46.5	4.33	8.11	0.59
	0	42.17(4.39)	41	1.17	7.76	0.88
	+2	42.17(4.39)	34	8.17	7.30	0.26
	+4	42.17(4.39)	35	7.05	7.38	0.34
s_2 $(q = 1)$	-4	62.79(8.75)	41.5	21.17	10.88	0.05
	-2	62.79(8.75)	46.5	16.29	11.10	0.14
	0	62.79(8.75)	41	21.79	10.84	0.04
	+2	62.79(8.75)	34	28.79	10.52	<0.01
	+4	62.79(8.75)	35	27.67	10.57	<0.01
s_1 $(q = 0.7)$	-4	34.20(2.92)	41.5	7.41	7.09	0.30
	-2	34.20(2.92)	46.5	12.30	7.42	0.10
	0	34.20(2.92)	41	6.80	7.04	0.33
	+2	34.20(2.92)	34	0.20	6.52	0.98
	+4	34.20(2.92)	35	0.92	6.61	0.89
s_2 $(q = 0.7)$	-4	78.67(12.25)	41.5	37.05	13.85	<0.01
	-2	78.67(12.25)	46.5	32.17	14.02	0.02
	0	78.67(12.25)	41	37.67	13.82	<0.01
	+2	78.67(12.25)	34	44.67	13.57	<0.01
	+4	78.67(12.25)	35	43.55	13.61	<0.01

$s_1 = 8^-\{\frac{7}{2}^+[624]_\nu \otimes \frac{9}{2}^-[734]_\nu\}$ $(g_K = +0.01)$

$s_2 = 8^-\{\frac{7}{2}^-[514]_\pi \otimes \frac{9}{2}^+[624]_\pi\}$ $(g_K = +1.01)$

When considering the significance of the results, one must keep in mind the definition in this case of a p-value, as the probability of obtaining an equally, or less, consistent result between the proposed and observed values, given that the structural assignment is correct. This result therefore, shows good agreement with the s_1 configuration when taking $q = 1$. The results are most consistent with the s_2 configuration again when taking $q = 1$, with a p-value of 0.14, indicating that once in only around seven reproductions of this data, would we expect to see such a great difference between the N_{s2} and N_o values if the proton state were responsible. This is by no means an insignificant probability, but may still serve as an indication as to the dismissal of the s_2 state.

5.3.2 X-ray region intensities

The X-ray region intensities method described in Section 4.3 was applied to the R-ce-T γ-ray spectrum of transitions above the 8^- isomer in ^{252}No shown in Figure 5.12(a) (upper panel). The p-values found using Equations 4.7 and 4.17 were ~ 1 for s_1 and 0.05 for s_2 using an unquenched g_R with values and results shown in Table 5.8 and Figure 5.15 (a). The Figure shows N_{xo} as a dashed black line, with a $1\sigma_{xo}$ upper limit as a blue line. The ten most prominent K X-rays with their associated w_X values taken from Firestone [36] were considered and the energy range over which N_{xo} was taken was therefore 112 $\rightarrow$ 156 keV. This incorporated all the K X-ray transition peaks and also interband transition energies from four transitions with $I_i = 10 \rightarrow 13$. The background in the region was taken as 1.04 counts/keV. N_{xs} values were found using Equations 4.13 and 4.14 for s_1 and s_2 using intraband transition intensities from all thirteen observed peaks with $I_i = 10 \rightarrow 22$, where higher spin values were assumed to be not significantly populated. The conversion coefficients for all transitions were found using reference [31]. An investigation into the effect of quenching is shown in Figure 5.15 (b) for a value of $q = 0.7$. Here the p-values are found to be ~ 1 for s_1 and <0.01 for s_2.

The results show consistency with the neutron s_1 configuration for both $q = 1$ and

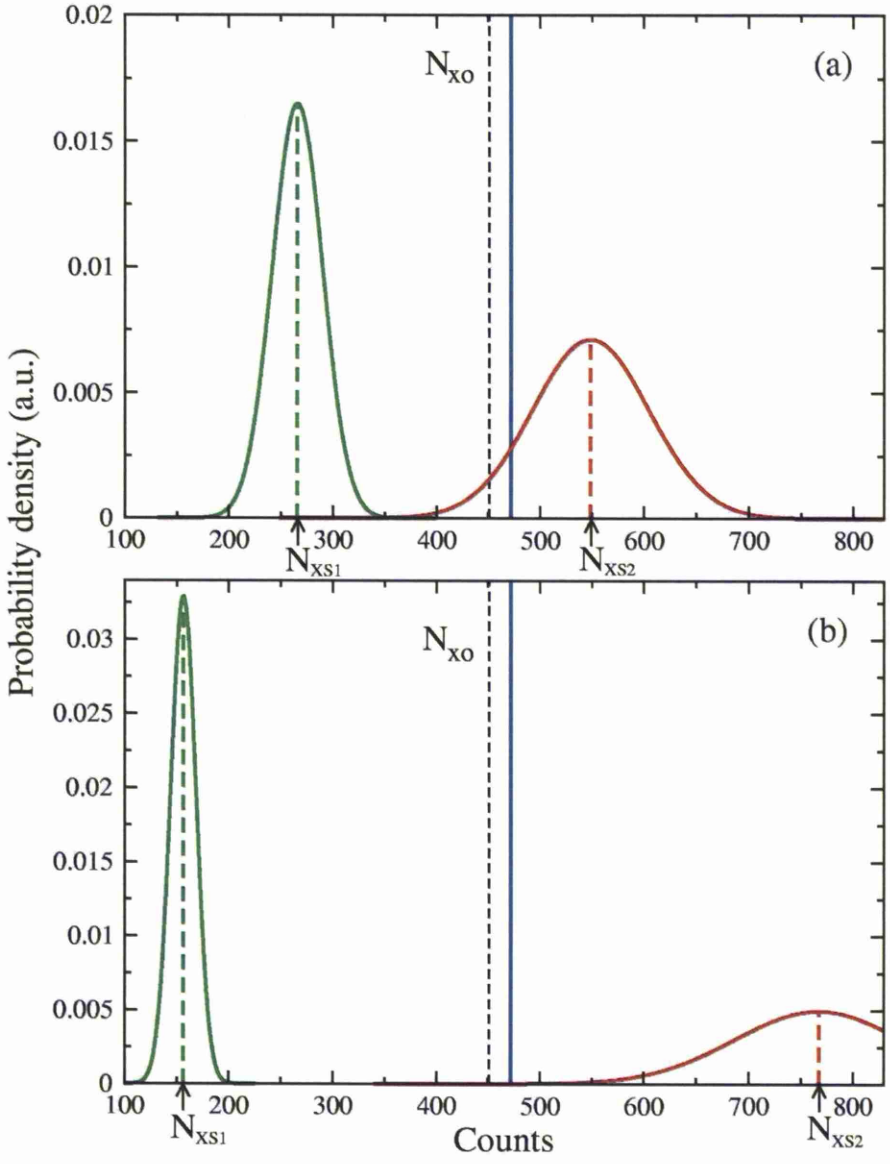

Figure 5.15: $N_{xs} \pm \sigma_{xs}$ found for structures s_1(green) and s_2(red) applying X-ray region intensities method using R-ce-T γ-ray spectrum of rotational band above 8^- isomer in ^{252}No, performed with $q = 1$(a) and 0.7(b). Compared with the observed counts $N_{xo} \pm \sigma_{xo}$ (black dashed) and $1\sigma_{xo}$ upper limit (blue).

Table 5.8: Obtained p-values and quantities in finding them for ^{252}No 8^- isomer using X-ray region intensities method for R-ce-T results.

structure	N_{xs}	N_{xo}	D_e	$(\sigma_{xs}{}^2+N_{xo})^{1/2}$	p
$q = 1$					
s_1	265.96(24.19)	451(21.20)	-185.04	32.17	$\sim$1
s_2	548.85(56.10)	451(21.20)	97.85	59.97	0.05
$q = 0.7$					
s_1	156.63(12.13)	451(21.20)	-294.37	24.42	$\sim$1
s_2	767.32(80.78)	451(21.20)	316.32	83.52	<0.01

$$s_1 = 8^-\{\tfrac{7}{2}^+[624]_\nu \otimes \tfrac{9}{2}^-[734]_\nu\}\ (g_K = +0.01)$$
$$s_2 = 8^-\{\tfrac{7}{2}^-[514]_\pi \otimes \tfrac{9}{2}^+[624]_\pi\}\ (g_K = +1.01)$$

0.7. However, this cannot be taken as direct evidence when using this method, due to the observed N_{xo} representing an upper limit when comparing with the expected intensity N_{xs}. A useful result may only be obtained if X-ray intensities are well below those expected for a configuration, hence dismissing the hypothesis. This is possible when considering the proton excitation s_2 as $D_e > 0$; here the most consistent result is seen for a $q = 1$ giving a p-value of 0.05. This is equivalent to expecting to obtain equally or less consistent results, once in twenty reproductions of the data, assuming s_2 is correct. Again this is not an insignificant probability, but clearly indicates the dismissal of the proton configuration s_2. It should be noted that these two p-values are not completely statistically independent, as the N_s and N_{xs} values are found using some of the same intraband transition intensities. The N_o and N_{xo} values however are fully independent. This means that the results from both the cumulative γ-ray branching ratios method and the X-ray region intensities method, may be considered as separate evidence for the assignment of the $8^-\{\frac{7}{2}^+[624]_\nu \otimes \frac{9}{2}^-[734]_\nu\}$ configuration

of the 8^- isomeric state in ^{252}No.

Chapter 6

Discussion

6.1 Moments of inertia

The kinematic and dynamic moments of inertia as a function of rotational frequency are shown in Figure 6.1 for both the ground state and 8^- isomeric state rotational bands in ^{252}No, along with those found for the analogous bands in ^{250}Fm [41].

The behaviour of the moments of inertia can give indications as to the rigidity and stability of a K-isomeric state and its rotational band. In the case of the ^{252}No 8^- configuration, the fact that the kinematic moment of inertia remains almost constant for increasing rotational frequency, indicates a rigid rotor. Also the robustness of the high K configuration, means that there is little difference between $\Im^{(1)}$ and $\Im^{(2)}$ initially, implying only small alignment of the unpaired nucleons' angular momenta along the rotational axis. This is consistent with the implications of the reduced hindrance factor values obtained of $f_\nu(\mathrm{E1},\ \Delta K = 8) = 178$ and $f_\nu(\mathrm{M1},\ \Delta K = 6) = 218$ for transitions from the state [51].

The effect of the quasi-particle excitation may be seen by comparing the $\Im^{(1)}$ for the ground state and 8^- rotational bands. As we see the ground state band increasing in rotational frequency, the antipairing Coriolis force aligns the angular momenta with that of the collective rotation and a steady increase is seen. For the 8^- band however, the two quasi-particle excitation acts to block the neutron pairing so that the initial

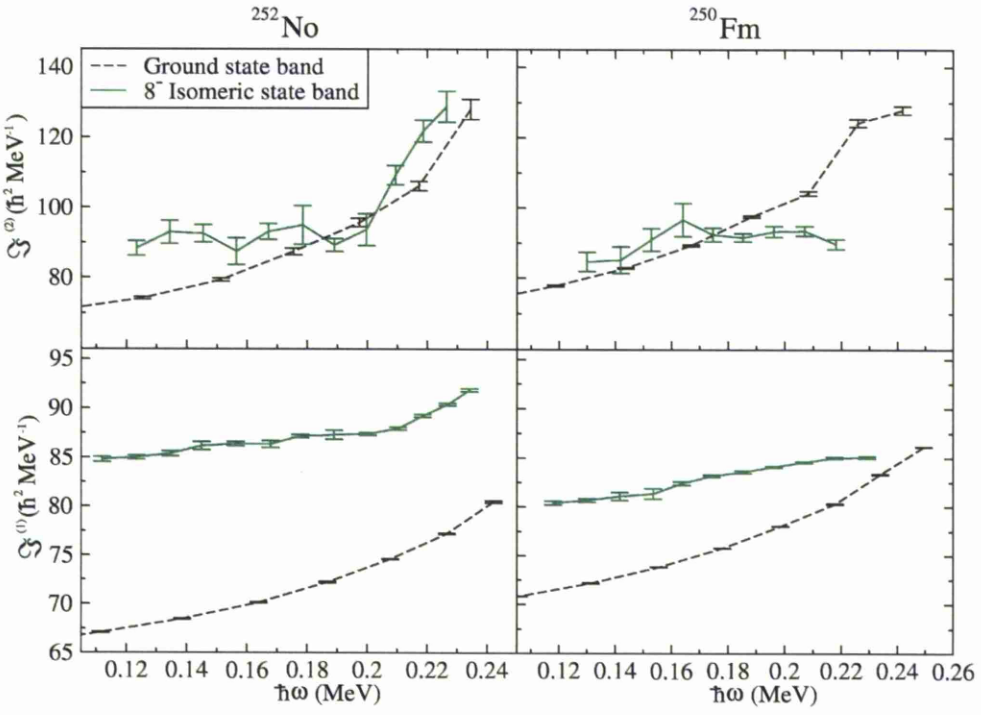

Figure 6.1: Kinematic and dynamic moments of inertia against rotational frequency for 8^- isomeric (green) and ground state (black) rotational bands in both ^{252}No and ^{250}Fm [41].

$\Im^{(1)}$ is higher, before remaining relatively flat as the rotational frequency increases. This initially increased $\Im^{(1)}$ is not thought to be due to any difference in deformation, as Hartree-Fock-Bogoliubov calculations predict similar quadrupole moments for both isomeric and ground state configurations [52].

The apparent steady behaviour of the $\Im^{(2)}$ seems to be disturbed at $\omega\hbar \sim 0.19$ MeV for the isomeric rotor in ^{252}No and also for that of ^{250}Fm. This could be due to interactions with other bands, but the situation is unclear at this point in relation to any structural significance. This effect however, should not be overstated, as the last three points for the $\Im^{(2)}$ for the ^{252}No isomeric band contain the tentative energy values from $I_i = 20 \rightarrow 22$.

6.2 Systematics in N = 150 and Z = 102 region

The single particle energy levels of a ^{252}No nucleus are shown in Figure 6.2 calculated within a Woods-Saxon potential with deformation parameter $\beta_2 = 0.25$ (as prescribed by Cwiok [59]) using universal parameters [18]. When using self consistent mean fields [52, 19], the energy level positions, and hence the spherical and deformed shell gap values, are found to be different from each other and also from those found when using macroscopic-microscopic methods. An inspection of the experimental regional systematics of excited states around ^{252}No should illuminate the single particle structure and help to compare and constrain the theoretical methods.

Excitations observed from five nuclei in the N = 150 isotone chain are given in Figure 6.3 for $94 \leq Z \leq 102$. As all isotones have an excitation at $I^\pi = 8^-$ with roughly the same energy (within 80 keV), it is likely that they are all a result of the same quasi-particle excitation. Also as this is an isotone chain with neutron number remaining at N = 150, this would suggest a neutron configuration is responsible. Direct evidence has been obtained from γ-ray intensity ratios to indicate that the $8^-\{\frac{7}{2}^+[624]_\nu \otimes \frac{9}{2}^-[734]_\nu\}$ configuration produces this state in both the ^{250}Fm [21],[this work] and now the ^{252}No nuclei [this work]. It is a reasonable conclusion then, that

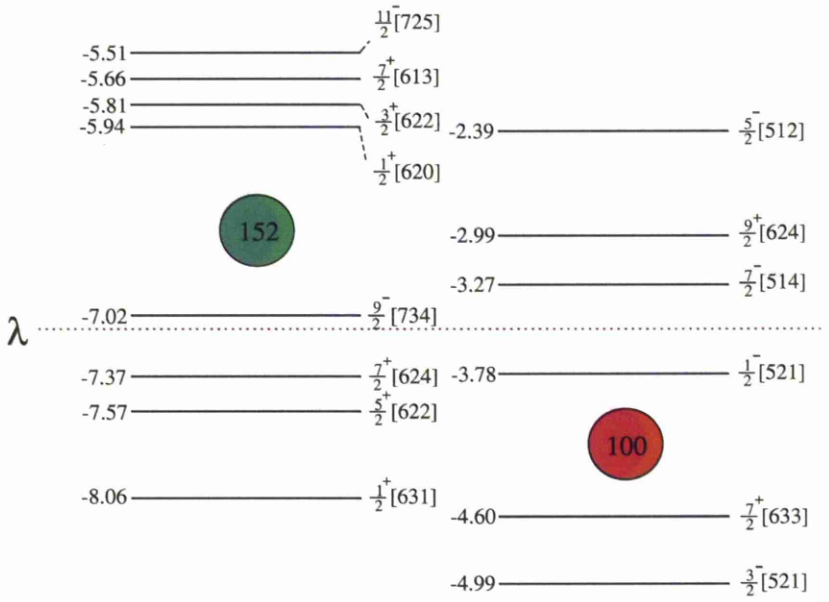

Figure 6.2: Single particle neutron and proton energy levels, calculated in a Woods-Saxon potential for ^{252}No [18]. The position of the Fermi surface is illustrated as λ.

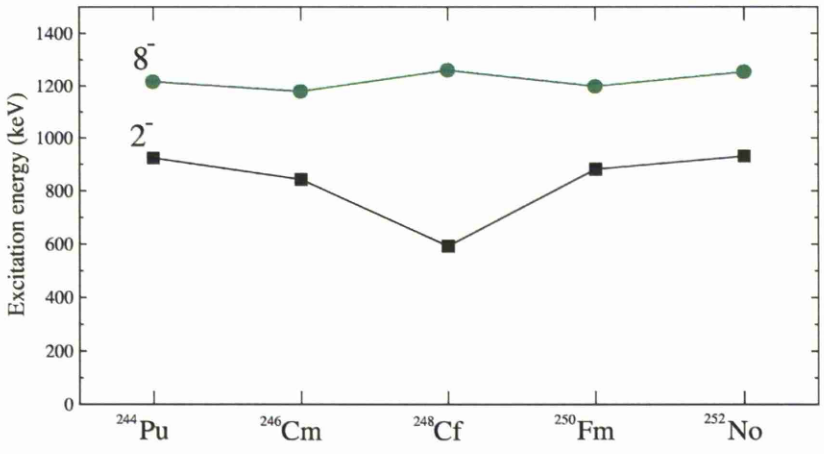

Figure 6.3: Excitation energies of $I^{\pi} = 2^{-}$ and 8^{-} excitations in the N = 150 isotonic chain. Results for ^{244}Pu [60, 61] and ^{248}Cf [62, 63] had spin and parities reassigned by Robinson [20]. Also shows results for ^{246}Cm [20, 64], ^{250}Fm [21] and ^{252}No [24, 20].

this same neutron configuration is present along the whole five member isotone chain.

The $I^{\pi} = 2^{-}$ states are seen to have energies significantly lower than those expected for pure quasi-particle excitations (see Section 2.3.1) and are therefore expected to be mixed states with contributions from octupole vibrations [20]. The ordering of the single particle levels, predicted using a Woods-Saxon potential, would suggest a low energy for the two quasi-particle $2^{-}\{\frac{9}{2}^{-}[734]_{\nu} \otimes \frac{5}{2}^{+}[622]_{\nu}\}$ configuration and results from Yates [62] suggests it contributes significantly to the excitation for ^{248}Cf. This is backed up by γ-ray intensity ratio results for the ^{250}Fm state [21] which also indicates the dominance of the same neutron 2 quasi-particle structure. The similarity in energy of these $I^{\pi} = 2^{-}$ excitations, leads to the conclusion that the neutron state indicated, contributes significantly to all these excitations in the N = 150 chain. The exception of the ^{248}Cf excitation, where a marked dip in energy is seen, is thought to be caused by a near degeneracy of the $\frac{7}{2}^{+}[633]_{\pi}$ and $\frac{3}{2}^{-}[521]_{\pi}$ proton states in this Z = 98 nucleus [20]. A 2^{-} excitation is possible with contributions from both proton and the neutron configurations, as well as the octupole vibration. This additional

contribution then acts to lower the overall energy of the state.

The presence of single particle neutron excitations in this N = 150 isotone, may be understood in terms of the Woods-Saxon energy level predictions in Figure 6.2. Here we see the neutron Fermi surface λ lies just below the predicted deformed shell gap at N = 152, leading to excitations into the $\frac{9}{2}^-[734]_\nu$ level to produce multi quasi-particle states. Further evidence for this N = 152 deformed shell gap may be found by investigating the next even isotone of N = 152. Here we would expect a large increase in the energies of neutron excitations, as the Fermi surface lies in the shell gap, making proton excitations more favourable. Two states have been observed in ^{254}No with the assignment of the lower energy state, at energy $E = 988$ keV, made as the $3^+\{\frac{1}{2}^-[521]_\pi \otimes \frac{7}{2}^-[514]_\pi\}$ configuration from γ-ray intensity ratios [22, 23]. Another excitation with $K^\pi = 8^-$ was assigned to the $8^-\{\frac{7}{2}^-[514]_\pi \otimes \frac{9}{2}^+[624]_\pi\}$ configuration in line with predicted macroscopic-microscopic excitation energies [22, 23] and with γ-ray intensity ratio measurements backing up this assertion [43],[present work]. These results, along with the absence of proton excitations in the Z = 100 nucleus ^{250}Fm, would suggest a consistency with the energy levels produced by such Woods-Saxon calculations, when considering the region around the deformed shell gaps [16, 59].

The self consistent mean field calculations [58, 65] by contrast, produce quasi-particle energies inconsistent with those observed and also do not reproduce the deformed shell gaps at N = 152 and Z = 100 for which experimental evidence has been presented. Figure 6.4 shows the single particle levels produced from self-consistent mean field calculations for a $^{250}_{100}\mathrm{Fm}_{150}$ nucleus as a function of prolate deformation, with the deformations expected within the region highlighted [19]. It is suggested that the $1j\frac{15}{2}^-$ neutron shell is too high in energy in these predictions and that by lowering it then the $\frac{9}{2}^-[734]$ and $\frac{7}{2}^+[624]$ states would be closer in energy and be in line with experimental evidence of the 2 quasi-particle excitations in the N = 150 isotones. This would also act to open the N = 152 deformed shell gap. Likewise, if the proton shell $1i\frac{13}{2}^+$ were lowered in energy, this would reproduce the energy of the $8^-\{\frac{7}{2}^-[514]_\pi \otimes \frac{9}{2}^+[624]_\pi\}$ state in ^{254}No and also open the Z = 100 shell gap. This

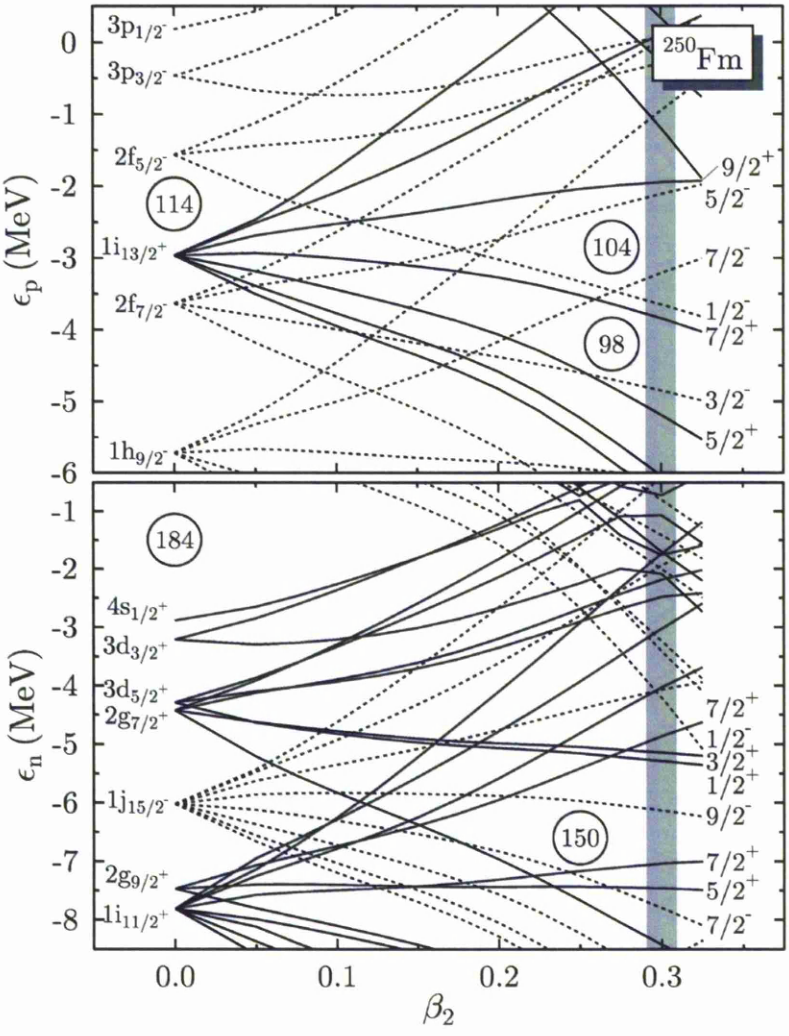

Figure 6.4: Single particle energy levels as a function of prolate deformation parameter β_2 for protons and neutrons found for a $^{250}_{100}\mathrm{Fm}_{150}$ nucleus in a self-consistent mean field. Figure taken from [19].

$1i\frac{13}{2}+$ proton shell is of particular interest as it resides around the predicted next spherical proton magic number.

Chapter 7

Summary and outlook

A spectroscopic study has been carried out on the nucleus ^{252}No, produced using the fusion evaporation reaction ^{206}Pb(^{48}Ca,2n)^{252}No (E_{beam} = 218 MeV) at the accelerator laboratory in Jyväskylä, Finland. The ^{252}No recoils were identified using recoil-decay tagging techniques. Values consistent with previous studies have been found for the ground state half-life, $T_{1/2}$ = 2.35(4) s, and decay branching fractions, b_α = 64.8(27)% and b_{SF} = 34.4%, and decays observed in the rotational band up to $I^\pi = 20^+$. Nuclei produced in the $K^\pi = 8^-$ K-isomeric state were identified using the conversion electron cascade of the isomer decay as a tag and values of its half-life, $T_{1/2}$ = 99.9(31) ms, and transition energies to the ground state via a 2^- excitation were confirmed. Spectra of γ-ray transitions within the signature partner rotational bands above the 8^- state were observed for the first time. The level scheme up to $I^\pi = 19^-$ has been established, with energies up to $I^\pi = 22^-$ tentatively assigned. The spin values of the levels were also somewhat tentatively assigned.

The low statistic spectra produced required the use of new approaches to the analytical techniques used in assigning the structure of the isomer. Two methods designed to fully utilise the statistics were shown, in the cumulative γ-ray branching ratios and the X-ray region intensities methods. These acted to combine statistics from an observed set of transition intensities within the rotational band and then use the predicted transition ratios relating to various isomer configurations to find

expected intensities in the spectrum relating to these states. This was done to predict both interband (ΔI =1) γ-ray and K X-ray intensities, which were compared with those observed to help assign a configuration. Results from both methods gave clear indications that it was the $8^-\{\frac{7}{2}^+[624]_\nu \otimes \frac{9}{2}^-[734]_\nu\}$ neutron configuration responsible for the isomeric state.

The observed states in ^{252}No were compared with other excitations in the N = 150 isotone chain with 94$\leq$Z$\leq$102. All members of the chain display $K^\pi = 2^-$ and 8^- states with substantial evidence, including the present work, that the same two neutron excitations are responsible. Considered in conjunction with evidence that the two lowest lying quasi-particle excitations in the N = 152 isotone chain member, ^{254}No, are proton states this supplies a good indication for the N = 152 deformed shell gap.

At present less is known about the nuclei in this N = 152 isotone chain and a desirable candidate to study would be the ^{252}Fm member. This should be a doubly deformed magic nucleus as Z = 100, where any isomeric states discovered would be of great interest. However, suitable beam-target combinations which would produce a viable cross-section of production are not available. This limit of viability for cross-section has, however, been reduced by the introduction of the JUROGAM-II in-beam array to the setup at Jyväskylä. Each detector has a count rate limit of 40 kHz in contrast to that of 10 kHz for the detectors in JUROGAM. This allows for the beam current to be significantly increased, subsequently increasing the production yield. The study of ^{256}Rf, produced with a cross-section of 12 nb, is currently planned with the use of this setup, which will hopefully further illuminate the N = 152 isotone chain.

The identification and assignment of K isomers in this region gives experimental evidence of the single particle level energies and orderings. This is vital for both the comparison with, and constraint of, theoretical models used to describe the nuclei in this mass region of the nuclear chart. Also results in this region are of particular interest, as some of the energy levels around these deformed shell gaps also play

an important role in the higher mass region of superheavy nuclei, around the long predicted next spherical shell closures.

Appendix A

Nilsson diagrams

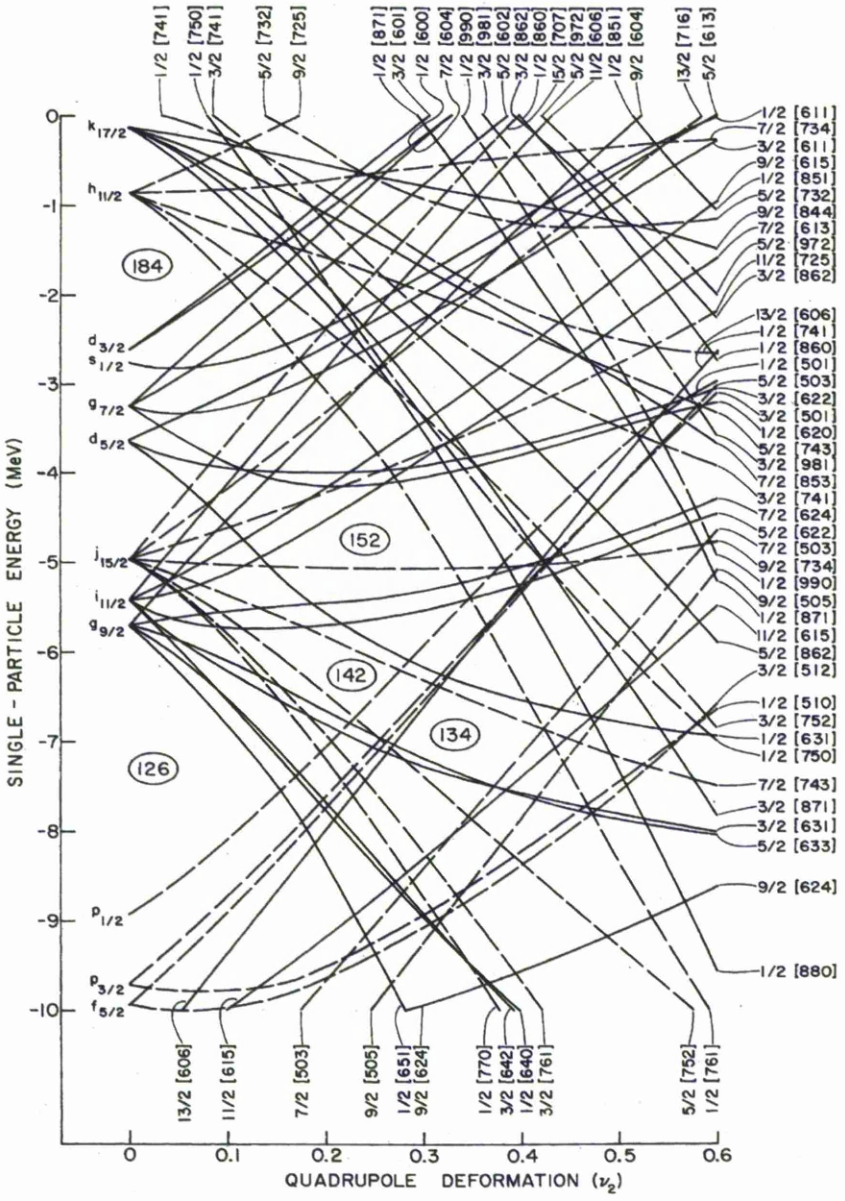

Figure A.1: Single particle neutron energy levels for high mass systems. Calculated using a deformed Woods-Saxon potential as a function of deformation, taken from [16].

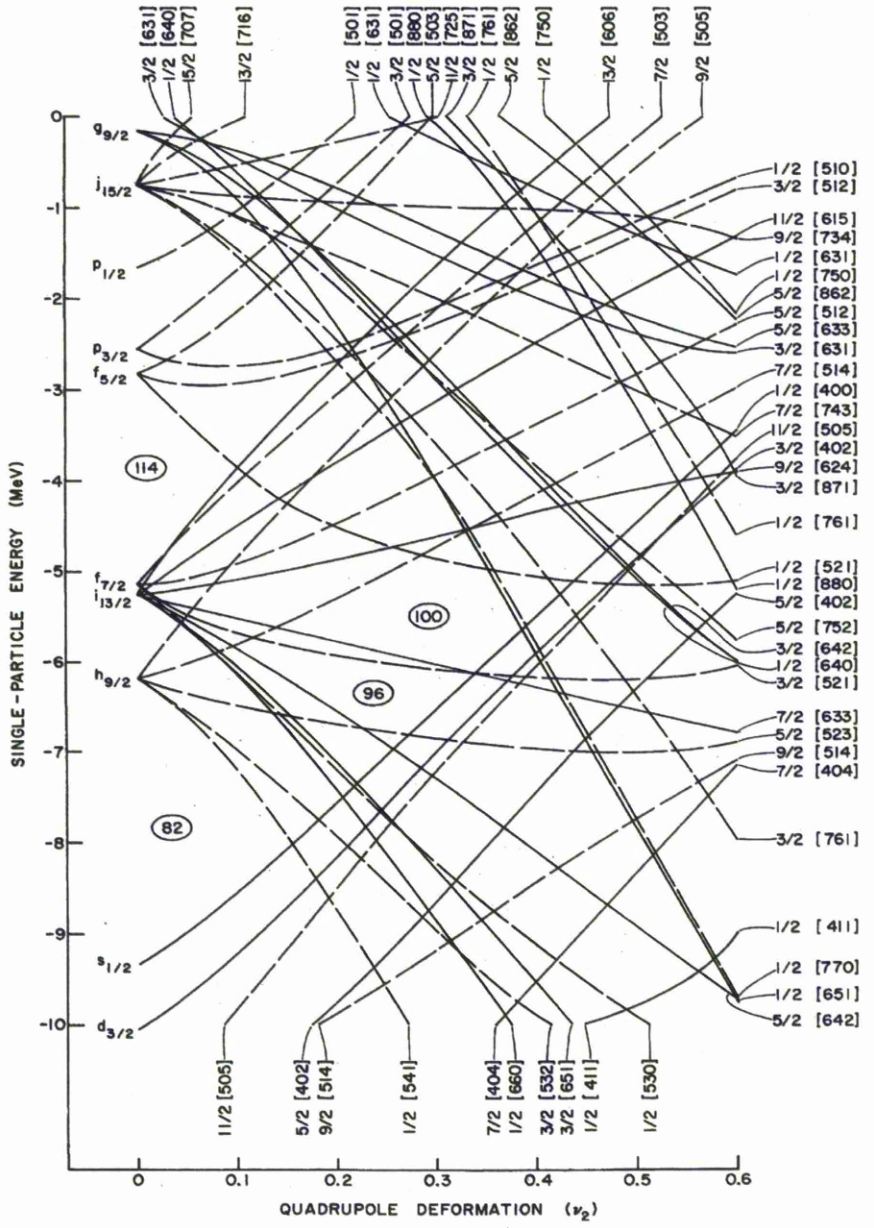

Figure A.2: Single particle proton energy levels for high mass systems. Calculated using a deformed Woods-Saxon potential as a function of deformation, taken from [16].

Bibliography

[1] Yu. Oganessian. Heaviest nuclei from 48 Ca-induced reactions. *Journal of Physics G: Nuclear and Particle Physics*, 34(4):R165, 2007.

[2] M. Bender, K. Rutz, P.-G. Reinhard, J. A. Maruhn, and W. Greiner. Shell structure of superheavy nuclei in self-consistent mean-field models. *Phys. Rev. C*, 60:034304, Aug 1999.

[3] H. Meldner. Predictions of new magic regions and masses for super-heavynuclei from calculations with realistic shell model single particle hamiltonian. *Arkiv Fysik*, 36:593–598, 1967.

[4] S.G. Nilsson, C. Fu Tsang, A. Sobiczewski, Z. Szymański, S. Wycech, C. Gustafson, I.L. Lamm, P. Möller, and B. Nilsson. On the nuclear structure and stability of heavy and superheavy elements. *Nuclear Physics A*, 131(1):1 – 66, 1969.

[5] S. Ćwiok, J. Dobaczewski, P.-H. Heenen, P. Magierski, and W. Nazarewicz. Shell structure of the superheavy elements. *Nuclear Physics A*, 611(2-3):211 – 246, 1996.

[6] P. Möller and J.R. Nix. Stability and decay of nuclei at the end of the periodic system. *Nuclear Physics A*, 549(1):84 – 102, 1992.

[7] R.R. Chasman and I. Ahmad. Nuclear structure at A $\sim$ 250 and the stability of the superheavy elements. *Physics Letters B*, 392(3-4):255 – 261, 1997.

[8] A. Sobiczewski and K. Pomorski. Description of structure and properties of superheavy nuclei. *Progress in Particle and Nuclear Physics*, 58(1):292 – 349, 2007.

[9] W. Zhang, J. Meng, S.Q. Zhang, L.S. Geng, and H. Toki. Magic numbers for superheavy nuclei in relativistic continuum Hartree-Bogoliubov theory. *Nuclear Physics A*, 753(1-2):106 – 135, 2005.

[10] M. Bender, W. Nazarewicz, and P.-G. Reinhard. Shell stabilization of super- and hyperheavy nuclei without magic gaps. *Physics Letters B*, 515(1-2):42 – 48, 2001.

[11] S. Hofmann and G. Münzenberg. The discovery of the heaviest elements. *Rev. Mod. Phys.*, 72:733–767, Jul 2000.

[12] P. Armbruster. On the production of superheavy elements. *Annual Review of Nuclear and Particle Science*, 50(1):411–479, 2000.

[13] K. Morita, K. Morimoto, D. Kaji, T. Akiyama, S. Goto, H. Haba, E. Ideguchi, R. Kanungo, K. Katori, H. Koura, H. Kudo, T. Ohnishi, A. Ozawa, T. Suda, K. Sueki, H. Xu, T. Yamaguchi, A. Yoneda, A. Yoshida, and Y. Zhao. Experiment on the synthesis of element 113 in the reaction ^{209}Bi(^{70}Zn,n)^{278}113. *Journal of the Physical Society of Japan*, 73(10):2593–2596, 2004.

[14] Yu. Ts. Oganessian, F. Sh. Abdullin, P. D. Bailey, D. E. Benker, M. E. Bennett, S. N. Dmitriev, J. G. Ezold, J. H. Hamilton, R. A. Henderson, M. G. Itkis, Yu. V. Lobanov, A. N. Mezentsev, K. J. Moody, S. L. Nelson, A. N. Polyakov, C. E. Porter, A. V. Ramayya, F. D. Riley, J. B. Roberto, M. A. Ryabinin, K. P. Rykaczewski, R. N. Sagaidak, D. A. Shaughnessy, I. V. Shirokovsky, M. A. Stoyer, V. G. Subbotin, R. Sudowe, A. M. Sukhov, Yu. S. Tsyganov, V. K. Utyonkov, A. A. Voinov, G. K. Vostokin, and P. A. Wilk. Synthesis of a new element with atomic number Z=117. *Phys. Rev. Lett.*, 104:142502, Apr 2010.

[15] Z. Patyk, A. Sobiczewski, P. Armbruster, and K.H. Schmidt. Shell effects in the properties of the heaviest nuclei. *Nuclear Physics A*, 491(2):267 – 280, 1989.

[16] R. R. Chasman, I. Ahmad, A. M. Friedman, and J. R. Erskine. Survey of single-particle states in the mass region A > 228. *Rev. Mod. Phys.*, 49:833–891, Oct 1977.

[17] G.D. Jones. Detection of long-lived isomers in super-heavy elements. *Nuclear Instruments and Methods in Physics Research Section A: Accelerators, Spectrometers, Detectors and Associated Equipment*, 488(1-2):471 – 472, 2002.

[18] S. Ćwiok, J. Dudek, W. Nazarewicz, J. Skalski, and T. Werner. Single-particle energies, wave functions, quadrupole moments and g-factors in an axially deformed Woods-Saxon potential with applications to the two-centre-type nuclear problems. *Computer Physics Communications*, 46(3):379 – 399, 1987.

[19] A. Chatillon, Ch. Theisen, P. Greenlees, G. Auger, J. Bastin, E. Bouchez, B. Bouriquet, J. Casandjian, R. Cee, E. Clément, R. Dayras, G. de France, R. de Toureil, S. Eeckhaudt, A. Görgen, T. Grahn, S. Grévy, K. Hauschild, R. Herzberg, P. Ikin, G. Jones, P. Jones, R. Julin, S. Juutinen, H. Kettunen, A. Korichi, W. Korten, Y. Le Coz, M. Leino, A. Lopez-Martens, S. Lukyanov, Yu. Penionzhkevich, J. Perkowski, A. Pritchard, P. Rahkila, M. Rejmund, J. Saren, C. Scholey, S. Siem, M. Saint-Laurent, C. Simenel, Yu. Sobolev, Ch. Stodel, J. Uusitalo, A. Villari, M. Bender, P. Bonche, and P. Heenen. Spectroscopy and single-particle structure of the odd- Z heavy elements ^{255}Lr, ^{251}Md and ^{247}Es. *The European Physical Journal A - Hadrons and Nuclei*, 30:397–411, 2006. 10.1140/epja/i2006-10134-5.

[20] A. P. Robinson, T. L. Khoo, I. Ahmad, S. K. Tandel, F. G. Kondev, T. Nakatsukasa, D. Seweryniak, M. Asai, B. B. Back, M. P. Carpenter, P. Chowdhury, C. N. Davids, S. Eeckhaudt, J. P. Greene, P. T. Greenlees, S. Gros, A. Heinz, R.-D. Herzberg, R. V. F. Janssens, G. D. Jones, T. Lauritsen, C. J. Lister,

D. Peterson, J. Qian, U. S. Tandel, X. Wang, and S. Zhu. $K^{\pi} = 8^{-}$ isomers and $K^{\pi} = 2^{-}$ octupole vibrations in N=150 shell-stabilized isotones. *Phys. Rev. C*, 78:034308, Sep 2008.

[21] P. T. Greenlees, R.-D. Herzberg, S. Ketelhut, P. A. Butler, P. Chowdhury, T. Grahn, C. Gray-Jones, G. D. Jones, P. Jones, R. Julin, S. Juutinen, T.-L. Khoo, M. Leino, S. Moon, M. Nyman, J. Pakarinen, P. Rahkila, D. Rostron, J. Sarén, C. Scholey, J. Sorri, S. K. Tandel, J. Uusitalo, and M. Venhart. High-K structure in ^{250}Fm and the deformed shell gaps at N=152 and Z=100. *Phys. Rev. C*, 78:021303, Aug 2008.

[22] R.-D. Herzberg, P. T. Greenlees, P. A. Butler, G. D. Jones, M. Venhart, I. G. Darby, S. Eeckhaudt, K. Eskola, T. Grahn, C. Gray-Jones, F. P. Heßberger, P. Jones, R. Julin, S. Juutinen, S. Ketelhut, W. Korten, M. Leino, A.-P. Leppanen, S. Moon, M. Nyman, R. D. Page, J. Pakarinen, A. Pritchard, P. Rahkila, J. Saren, C. Scholey, A. Steer, Y. Sun, Ch. Theisen, and J. Uusitalo. Nuclear isomers in superheavy elements as stepping stones towards the island of stability. *Nature*, 442:896–899, 2006.

[23] S. K. Tandel, T. L. Khoo, D. Seweryniak, G. Mukherjee, I. Ahmad, B. Back, R. Blinstrup, M. P. Carpenter, J. Chapman, P. Chowdhury, C. N. Davids, A. A. Hecht, A. Heinz, P. Ikin, R. V. F. Janssens, F. G. Kondev, T. Lauritsen, C. J. Lister, E. F. Moore, D. Peterson, P. Reiter, U. S. Tandel, X. Wang, and S. Zhu. K isomers in ^{254}No: Probing single-particle energies and pairing strengths in the heaviest nuclei. *Phys. Rev. Lett.*, 97:082502, Aug 2006.

[24] B. Sulignano, S. Heinz, F. Heßberger, S. Hofmann, D. Ackermann, S. Antalic, B. Kindler, I. Kojouharov, P. Kuusiniemi, B. Lommel, R. Mann, K. Nishio, A. Popeko, Š. Šáro, B. Streicher, M. Venhart, and A. Yeremin. Identification of a K isomer in ^{252}No. *The European Physical Journal A - Hadrons and Nuclei*, 33:327–331, 2007. 10.1140/epja/i2007-10469-3.

[25] R. F. Casten. *Nuclear Structure from a Simple Perspective.* Oxford Science Publications, Oxford, second printing edition, 2000.

[26] V.M. Strutinsky. Shell effects in nuclear masses and deformation energies. *Nuclear Physics A*, 95(2):420 – 442, 1967.

[27] P. Walker and G. Dracoulis. Energy traps in atomic nuclei. *Nature*, 399:35–40, 1999.

[28] K.E.G. Löbner. Systematics of absolute transition probabilities of K-forbidden gamma-ray transitions. *Physics Letters B*, 26(6):369 – 370, 1968.

[29] A. Bohr and B. R. Mottelson. *Nuclear Structure.* World Scientific, Singapore, 1998.

[30] V. F. Weisskopf. Radiative transition probabilities in nuclei. *Phys. Rev.*, 83:1073–1073, Sep 1951.

[31] T. Kibédi, T.W. Burrows, M.B. Trzhaskovskaya, P.M. Davidson, and C.W. Nestor Jr. Evaluation of theoretical conversion coefficients using brIcc. *Nuclear Instruments and Methods in Physics Research Section A: Accelerators, Spectrometers, Detectors and Associated Equipment*, 589(2):202 – 229, 2008. http://bricc.anu.edu.au/.

[32] B. Cohen and C. Fulmer. Fission-fragment mass separator and the nuclear charge distribution of fission fragments of a single mass. *Nucl. Phys.*, 6:547–560, 1958.

[33] M Leino, J Äystö, T Enqvist, P Heikkinen, A Jokinen, M Nurmia, A Ostrowski, W.H Trzaska, J Uusitalo, K Eskola, P Armbruster, and V Ninov. Gas-filled recoil separator for studies of heavy elements. *Nuclear Instruments and Methods in Physics Research Section B: Beam Interactions with Materials and Atoms*, 99(1-4):653 – 656, 1995. Application of Accelerators in Research and Industry.

[34] R.D. Page, A.N. Andreyev, D.E. Appelbe, P.A. Butler, S.J. Freeman, P.T. Greenlees, R.-D. Herzberg, D.G. Jenkins, G.D. Jones, P. Jones, D.T. Joss, R. Julin,

H. Kettunen, M. Leino, P. Rahkila, P.H. Regan, J. Simpson, J. Uusitalo, S.M. Vincent, and R. Wadsworth. The GREAT spectrometer. *Nuclear Instruments and Methods in Physics Research Section B: Beam Interactions with Materials and Atoms*, 204(0):634 – 637, 2003. 14th International Conference on Electromagnetic Isotope Separators and Techniques Related to their Applications.

[35] G. F. Knoll. *Radiation Detection and Measurement.* John Wiley & Sons, inc., New York, third printing edition, 2000.

[36] R. B. Firestone. *Table of Isotopes.* John Wiley & Sons, inc., New York, eighth printing edition, 1996.

[37] H Weick. ATIMA. http://www-linux.gsi.de/ weick/atima/atima.html, 2011.

[38] D. C. Radford. Notes on gf3. http://radware.phy.ornl.gov/gf3/, 2000.

[39] Yu. Ts. Oganessian, V. K. Utyonkov, Yu. V. Lobanov, F. Sh. Abdullin, A. N. Polyakov, I. V. Shirokovsky, Yu. S. Tsyganov, A. N. Mezentsev, S. Iliev, V. G. Subbotin, A. M. Sukhov, K. Subotic, O. V. Ivanov, A. N. Voinov, V. I. Zagrebaev, K. J. Moody, J. F. Wild, N. J. Stoyer, M. A. Stoyer, and R. W. Lougheed. Measurements of cross sections for the fusion-evaporation reactions ^{204,206,207,208}Pb+^{48}Ca and ^{207}Pb+^{34}S : decay properties of the even-even nuclides ^{238}Cf and ^{250}No. *Phys. Rev. C*, 64:054606, Oct 2001.

[40] I. Lazarus, E.E. Appelbe, P.A. Butler, P.J. Coleman-Smith, J.R. Cresswell, S.J. Freeman, R.D. Herzberg, I. Hibbert, D.T. Joss, S.C. Letts, R.D. Page, V.F.E. Pucknell, P.H. Regan, J. Sampson, J. Simpson, J. Thornhill, and R. Wadsworth. The GREAT triggerless total data readout method. *Nuclear Science, IEEE Transactions on*, 48(3):567 –569, jun 2001.

[41] D. Rostron. *Spectroscopy of ^{250}Fm using Tagging Techniques.* PhD thesis, University of Liverpool, 2009.

[42] F. R. Xu, E. G. Zhao, R. Wyss, and P. M. Walker. Enhanced stability of superheavy nuclei due to high-spin isomerism. *Phys. Rev. Lett.*, 92:252501, Jun 2004.

[43] F. Heßberger, S. Antalic, B. Sulignano, D. Ackermann, S. Heinz, S. Hofmann, B. Kindler, J. Khuyagbaatar, I. Kojouharov, P. Kuusiniemi, M. Leino, B. Lommel, R. Mann, K. Nishio, A. Popeko, Š. Šáro, B. Streicher, J. Uusitalo, M. Venhart, and A. Yeremin. Decay studies of K isomers in ^{254}No. *The European Physical Journal A - Hadrons and Nuclei*, 43:55–66, 2010. 10.1140/epja/i2009-10899-9.

[44] R.M. Clark, K.E. Gregorich, J.S. Berryman, M.N. Ali, J.M. Allmond, C.W. Beausang, M. Cromaz, M.A. Deleplanque, I. Dragojević, J. Dvorak, P.A. Ellison, P. Fallon, M.A. Garcia, J.M. Gates, S. Gros, H.B. Jeppesen, D. Kaji, I.Y. Lee, A.O. Macchiavelli, K. Morimoto, H. Nitsche, S. Paschalis, M. Petri, L. Stavsetra, F.S. Stephens, H. Watanabe, and M. Wiedeking. High-K multi-quasiparticle states in ^{254}No. *Physics Letters B*, 690(1):19 – 24, 2010.

[45] A. Ghiorso, T. Sikkeland, and M. J. Nurmia. Isotopes of element 102 with mass 251 to 258. *Phys. Rev. Lett.*, 18:401–404, Mar 1967.

[46] C. E. Bemis, Robert L. Ferguson, Franz Plasil, R. J. Silva, Frances Pleasonton, and R. L. Hahn. Fragment-mass and kinetic-energy distributions from the spontaneous fission of ^{252}No. *Phys. Rev. C*, 15:705–712, Feb 1977.

[47] R.-D. Herzberg, N. Amzal, F. Becker, P. A. Butler, A. J. C. Chewter, J. F. C. Cocks, O. Dorvaux, K. Eskola, J. Gerl, P. T. Greenlees, N. J. Hammond, K. Hauschild, K. Helariutta, F. Heßberger, M. Houry, G. D. Jones, P. M. Jones, R. Julin, S. Juutinen, H. Kankaanpää, H. Kettunen, T. L. Khoo, W. Korten, P. Kuusiniemi, Y. Le Coz, M. Leino, C. J. Lister, R. Lucas, M. Muikku, P. Nieminen, R. D. Page, P. Rahkila, P. Reiter, Ch. Schlegel, C. Scholey, O. Stezowski,

Ch. Theisen, W. H. Trzaska, J. Uusitalo, and H. J. Wollersheim. Spectroscopy of transfermium nuclei: $^{252}_{102}$No. *Phys. Rev. C*, 65:014303, Dec 2001.

[48] Y.A. Akovali. Review of alpha-decay data from doubly-even nuclei. *Nuclear Data Sheets*, 84(1):1 – 114, 1998.

[49] B. Sulignano. *Search for K isomers in ^{252,254}No and ^{260}Sg and investigation of their nuclear structure.* PhD thesis, Johannes Gutenberg-University, Mainz, Germany, 2007.

[50] A. N. Andreyev, D. D. Bogdanov, V. I. Chepigin, A. P. Kabachenko, O. N. Malyshev, R. N. Sagaidak, L. I. Salamatin, G. M. Ter-Akopian, and A. V. Yeremin. Cross sections of 102 element isotopes formation in the reactions of ^{22}Ne+^{236}U and ^{26}Mg+^{232}Th. *Zeitschrift für Physik A Hadrons and Nuclei*, 345:389–394, 1993. 10.1007/BF01282899.

[51] B. Sulignano and E. Parr et al. Investigation of high K states in ^{252}No. in preparation.

[52] J.-P. Delaroche, M. Girod, H. Goutte, and J. Libert. Structure properties of even-even actinides at normal and super deformed shapes analysed using the Gogny force. *Nuclear Physics A*, 771(0):103 – 168, 2006.

[53] A. Leppänen, J. Uusitalo, P. Greenlees, R. Herzberg, N. Amzal, F. Becker, P. Butler, A. Chewter, J. Cocks, O. Dorvaux, S. Eeckhaudt, K. Eskola, J. Gerl, T. Grahn, N. Hammond, K. Hauschild, K. Helariutta, F. Heßberger, M. Houry, G. Jones, P. Jones, R. Julin, S. Juutinen, H. Kankaanpää, H. Kettunen, T. Khoo, W. Korten, P. Kuusiniemi, Y. Le Coz, M. Leino, C. Lister, R. Lucas, M. Muikku, P. Nieminen, M. Nyman, R. Page, J. Pakarinen, P. Rahkila, P. Reiter, J. Sarén, Ch. Schlegel, C. Scholey, O. Stezowski, Ch. Theisen, W. Trzaska, and H. Wollersheim. Recoil-fission tagging of the transfermium nucleus ^{252}No. *The European Physical Journal A - Hadrons and Nuclei*, 28:301–306, 2006. 10.1140/epja/i2006-10056-2.

[54] A.V. Belozerov, M.L. Chelnokov, V.I. Chepigin, T.P. Drobina, V.A. Gorshkov, A.P. Kabachenko, O.N. Malyshev, I.M. Merkin, Yu.Ts. Oganessian, A.G. Popeko, R.N. Sagaidak, A.I. Svirikhin, A.V. Yeremin, G. Berek, I. Brida, and Š. Šáro. Spontaneous-fission decay properties and production cross-sections for the neutron-deficient nobelium isotopes formed in the ^{44,48}Ca + ^{204,206,208}Pb reactions. *The European Physical Journal A - Hadrons and Nuclei*, 16:447–456, 2003. 10.1140/epja/i2002-10109-6.

[55] J. E. Draper, F. S. Stephens, M. A. Deleplanque, W. Korten, R. M. Diamond, W. H. Kelly, F. Azaiez, A. O. Macchiavelli, C. W. Beausang, E. C. Rubel, J. A. Becker, N. Roy, E. A. Henry, M. J. Brinkman, A. Kuhnert, and S. W. Yates. Spins in superdeformed bands in the mass 190 region. *Phys. Rev. C*, 42:R1791–R1795, Nov 1990.

[56] J. A. Becker, E. A. Henry, A. Kuhnert, T. F. Wang, S. W. Yates, R. M. Diamond, F. S. Stephens, J. E. Draper, W. Korten, M. A. Deleplanque, A. O. Macchiavelli, F. Azaiez, W. H. Kelly, J. A. Cizewski, and M. J. Brinkman. Level spin for superdeformed nuclei near A=194. *Phys. Rev. C*, 46:889–903, Sep 1992.

[57] G. Hackman, T. L. Khoo, M. P. Carpenter, T. Lauritsen, A. Lopez-Martens, I. J. Calderin, R. V. F. Janssens, D. Ackermann, I. Ahmad, S. Agarwala, D. J. Blumenthal, S. M. Fischer, D. Nisius, P. Reiter, J. Young, H. Amro, E. F. Moore, F. Hannachi, A. Korichi, I. Y. Lee, A. O. Macchiavelli, T. Døssing, and T. Nakatsukasa. Spins, parity, excitation energies, and octupole structure of an excited superdeformed band in ^{194}Hg and implications for identical bands. *Phys. Rev. Lett.*, 79:4100–4103, Nov 1997.

[58] A.V. Afanasjev, T.L. Khoo, S. Frauendorf, G.A. Lalazissis, and I. Ahmad. Cranked relativistic Hartree-Bogoliubov theory: Probing the gateway to superheavy nuclei. *Phys. Rev. C*, 67:024309, Feb 2003.

[59] S. Ćwiok, S. Hofmann, and W. Nazarewicz. Shell structure of the heaviest elements. *Nuclear Physics A*, 573(3):356 – 394, 1994.

[60] R. C. Thompson, J. R. Huizenga, and Th. W. Elze. Collective states in ^{230}Th, ^{240}Pu, ^{244}Pu, and ^{248}Cm excited by inelastic deuteron scattering. *Phys. Rev. C*, 12:1227–1235, Oct 1975.

[61] K. J. Moody, W. Brüchle, M. Brügger, H. Gäggeler, B. Haefner, M. Schädel, K. Sümmerer, H. Tetzlaff, G. Herrmann, N. Kaffrell, J. V. Kratz, J. Rogowski, N. Trautmann, M. Skålberg, G. Skarnemark, J. Alstad, and M. M. Fowler. New nuclides: Neptunium-243 and Neptunium-244. *Zeitschrift für Physik A Hadrons and Nuclei*, 328:417–422, 1987. 10.1007/BF01289627.

[62] S.W. Yates, R.R. Chasman, A.M. Friedman, I. Ahmad, and K. Katori. Particle-phonon interactions in ^{248}Cf and ^{249}Cf. *Phys. Rev. C*, 12:442–450, Aug 1975.

[63] K. Katori, I. Ahmad, and A. M. Friedman. Two-quasineutron states in $^{248}_{98}$Cf and $^{250}_{98}$Cf and the neutron-neutron residual interactions. *Phys. Rev. C*, 78:014301, Jul 2008.

[64] L.G. Multhauf, K.G. Tirsell, and R.A. Meyer. Collective excitations in ^{246}Cm and the decay of ^{246}Am^{m}. *Phys. Rev. C*, 13:771–789, Feb 1976.

[65] M. Bender, P. Bonche, T. Duguet, and P.-H. Heenen. Skyrme mean-field study of rotational bands in transfermium isotopes. *Nuclear Physics A*, 723(3-4):354 – 364, 2003.